Topographic Effects on Strong Winds in Southern Norway; A Case Study of the Storm Dagmar

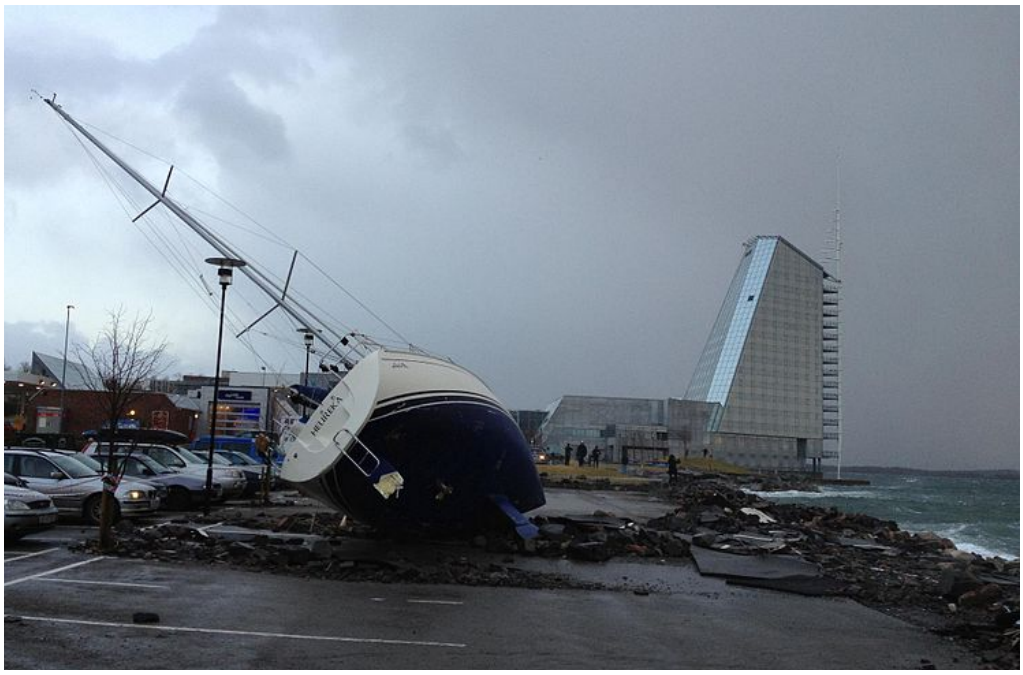

Master's Thesis in Meteorology

Ida Marie Solbrekke

June 2014

UNIVERSITY OF BERGEN
GEOPHYSICAL INSTITUTE

The figure on the front page shows
a sail boat blown ashore in Molde,
on the 25th of December 2011.
Picture is retrieved from NSAA (NSAA, 2014).

Acknowledgements

First of all, I would like to express my gratitude to my outstanding supervisor, Asgeir Sorteberg. Thanks for guiding and pointing me in the right direction, for the good ideas, and for all the interesting discussions. It has really been educational and fun. Thanks to my co-supervisor Mari Sandvik, who helped me with the WRF model, and also for helping me proofread.

A huge thank you to my fantastic boyfriend, Algot Kristoffer Peterson, for always cheering me up, for the interesting discussions, and for helping me proofread.

I also have a huge thank you to Torbjørn Taskjelle, for all the help with MatLab and LaTeX problems.

Thank you to the two Idars: Barstad for letting me borrow his linear wave model, and to Hessevik for helping me with more disk-space whenever needed, and other Linux problems.

Last but not least, thanks to all of my fellow students, making these past 5 years memorable and so fun!

Abstract

During the 25th of December 2011 a strong low pressure system struck Soutwestern Norway. This rapidly evolving system got the name "Dagmar". The aim of this thesis was to find out how the complex topography in Southern Norway affected the strong winds caused by Dagmar. An observational analysis was carried out, together with high resolution numerical simulations performed by the the Weather Research and Forcasting model (WRF). A linear wave model (Barstad and Grønås, 2005) was used to address the result form the WRF model and the observational analysis. In addition, the linear wave model was used to investigate how changes in key parameters like wind speed, wind direction, mountain height, and atmospheric stability could have influenced the WRF model results. The highest observed 10-m wind speed was measured at Kråkenes lighthouse, $43.8\,\mathrm{m\,s^{-1}}$, while the strongest wind gust was measured at Juvvasshø, $64.7\,\mathrm{m\,s^{-1}}$. The WRF model was set to simulate Dagmar with a realistic topography in Southern Norway. In addition, two other simulations were carried out: One where the topography of Southern Norway was smoothed out, and one run where the topography was completely removed. This was done to see the effect of Norway's complex topography on the strong winds caused by Dagmar. The flat topography simulation showed that the sting jet (strong winds to the south of Dagmar's core), which did not reach the coast in the topography-runs, reached inland when the mountain was removed. The reason for this retardation of the flow upstream of the mountain in the topography-runs was due to the presence of the mountain, and the corresponding high pressure region created on the windward side. The strength of this upstream wind shadow varied when the upstream wind direction changed. Another feature, present only in the mountain-runs, was a "left side jet", e.g., an region of accelerated air along the northwest coast. The linear wave model showed that the wind pattern was sensitive to changes in the key parameters, and varying the upstream wind direction from westerly to southwesterly was crucial for the exsistence of the left side jet.

Contents

Chapter 1

Introduction

Low (and high) pressure systems help the Earth to redistibute the energy from the sun. This energy is unevenly distributed due to the Earth's obliquity[1], its elliptical orbit around the sun, and the spherical shape of the Earth. The increased amount of greenhouse gases in the atmosphere will impact the developement of these low pressure systems, and a report from 2013, produced by The Norwegian Meteorological Institute about extreme weather events in Europe (Hov et al., 2013), stated that;

> *Under the increasing greenhouse gas concentrations of the IPCC SRES scenarios, climate models project a decrease in the total number of cyclones in the northern hemisphere mid-latitudes. However, these models indicate an increase in the number of severe storms in Northwestern and Central Europe.*

The wind caused by these strong systems will interact with the topography in Southern Norway and can result in modifications of both the wind speed and the wind direction. The topography in Southern Norway is characterized by the mountain range Langfjella, which divides the southern part of Norway meridionally into two regions, together with narrow fjords and valleys (for the topography in Southern Norway see Figure 6.1). Norway is known for its complex topography, and the interaction between the low pressure systems and the terrain is interesting, and of importance, because the knowledge can contribute to protect human lives and material assets, save financial costs and also improve weather forcasts.

During the 25th and 26th of December 2011 two strong low pressure systems struck Norway. The satellite pictures in Figure 1.1 show the synoptic situation at that time, and the two low pressure systems. During the night of the 25th a storm called "Cato" struck Norway, but it mainly affected the northern part. Bjerknes and Solberg (1922) stated that a new low pressure system can develop in the tail of a cold front corresponding to an already exsisting low pressure system. And, in the tail of Cato's cold front a new system started to develop. This rapidly evolving system got the name "Dagmar". Most affected was the northwestern part of Southern Norway.

[1]The obliquity, or the tilt of the Earth, is the angle between the the rotational axis and the normal to the plane of the elliptical orbit around the sun (Hartmann, 1994).

The lighthouse located at Kråkenes in Sogn og Fjordane measured a mean wind (10-min average) of $43.8\,\mathrm{m\,s^{-1}}$, and a wind gust of $58\,\mathrm{m\,s^{-1}}$ (the strongest instantaneous wind speed during one hour). Strong winds were also measured in the mountains, Juvasshø in Oppland had a mean wind of $39.4\,\mathrm{m\,s^{-1}}$ with gusts up to $65\,\mathrm{m\,s^{-1}}$ (MET, 2012). Several other stations also measured a mean wind stronger than hurricane force ($> 32.7\,\mathrm{m\,s^{-1}}$). A report submitted as a result of a colaboration between NVE and Kjeller Vindteknikk concluded that a storm like Dagmar, with unusual strong winds between southwest to west, is expected to occur once every 40 to 100 years, while a storm like that in general (independent of wind direction) was estimated to occur every 10- to 40 years (Harstveit, 2012). The costs of the damaged assets was more than 1.3 billion Norwegian kroners, of which the costs in Møre og Romsdal accounted for more than half of this sum (FinansNorge, 2013). The total costs are unknown, but when the New-Years Storm struck Norway in 1992 the total costs were more than twice the insured amount (Teigland, 2002).

In this thesis the focus will be on the storm Dagmar; why some places were more affected than others, and how these strong winds interacted with the complex topography in the southern part of Norway. The synoptic situation will not be discussed in detail. Barstad and Grønås (2005) simulated the effect of an ideal flow passing Southern Norway. They found that the topography in Southern Norway affected both the strength of the wind and the wind direction. Depending on the upstream values of both wind speed and direction the outcome was different. Whiteman and Doran (1993) considered four possible mechanisms that could produce distinct relationships between wind above and within a valley: thermal forcing, strong downward transport of horizontal momentum, magnitude of the component of the ambient wind projected along the valley axis, and pressure-driven channeling. Damaging gravity waves and hydraulic jumps can occur as a consequence of strong winds flowing over complex topography. Likewise, we can get funneling effect and gap flows due to the fjords and valleys (Markowski and Richardson, 2011). Both observations, high resoultion numerical simulations (The Weather Research and Forcast model, WRF), and a linear wave model will be used to obtain a better understanding of the meteorological situation that occurred. Three WRF model runs, with different topography, will be investigated to see how the wind pattern changes. The first simulation will be a run using realistic topography of Southern Norway. For the second run the complexity of the realistic topography will be removed, using a smoothed mountain. In the last run, the topography will be completely removed. A linear wave model will also be used to acheive a better understanding of how sensitive the interaction between the wind and a Gaussian mountain is to changes in wind speed, wind direction, mountain height and the atmospheric stability.

In Chapter 2 the theories behind interaction between a flow and a topography will be considered. WRF and the linear wave model will be described in Chapter 3. The synoptic situation and an analysis of the observations will be presented in Chapter 4. Validation of the WRF model and the results from the linear wave model will be

discussed in Chapter 5, while the results and comparison between the three WRF model runs will be presented and discussed in Chapter 6. Some concluding remarks can be found at the end, in Chapter 7.

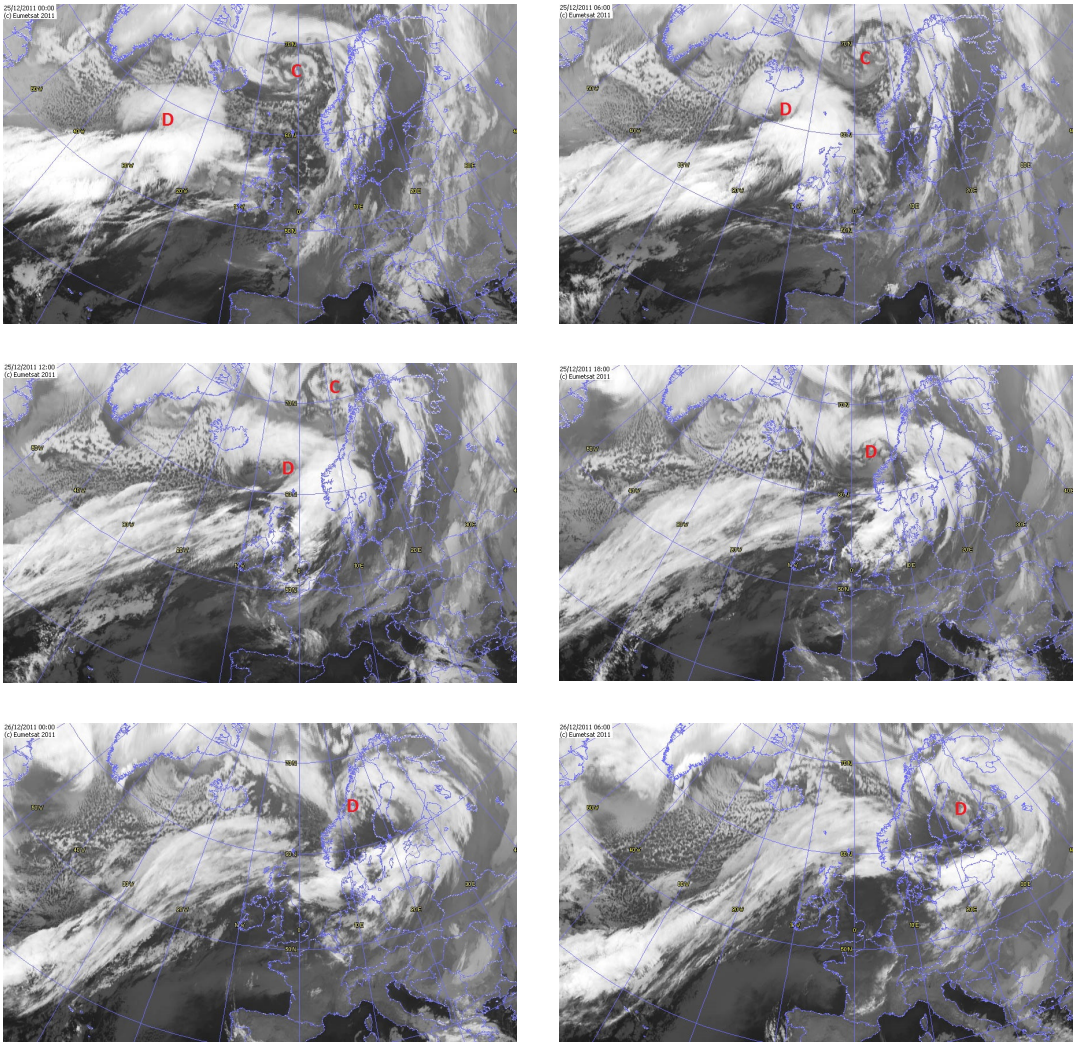

Figure 1.1: Satellite pictures of the large scale synoptic situation, from the 25th of December at 0000UTC (upper left panel) until 26th of December at 0600UTC (lower right panel). The symbol "C" indicates the position of the low pressure system Cato, and "D" shows the position of Dagmar. Satellite pictures retreived from Wetterzentrale (2014).

Chapter 2

Background

How a flow responds to topography depends mostly on the shape of the mountain and the characteristics of the large-scale flow. The result of the interaction between the flow and the topography can make the flow change dramatically, both from its upstream direction and its upstream flow speed.

2.1 Mountain Waves

Wave-like patterns are found everywhere in the atmosphere. The governing equations in the atmosphere allow wave solutions of any kind, like mountain-generated gravity waves. The derivation below follows Markowski and Richardson (2011). Assuming no friction and no diabatic heating effects, the equations of motion takes on this form;

$$\frac{\partial u}{\partial t} + u\frac{\partial u}{\partial x} + v\frac{\partial u}{\partial y} + w\frac{\partial u}{\partial z} + \frac{1}{\rho}\frac{\partial p}{\partial x} - fv = 0 \tag{2.1}$$

$$\frac{\partial v}{\partial t} + u\frac{\partial v}{\partial x} + v\frac{\partial v}{\partial y} + w\frac{\partial v}{\partial z} + \frac{1}{\rho}\frac{\partial p}{\partial y} + fu = 0 \tag{2.2}$$

$$\frac{\partial w}{\partial t} + u\frac{\partial w}{\partial x} + v\frac{\partial w}{\partial y} + w\frac{\partial w}{\partial z} + \frac{1}{\rho}\frac{\partial p}{\partial z} - g = 0 \tag{2.3}$$

$$\frac{\partial \rho}{\partial t} + \nabla \cdot (\rho \bar{v}) = 0 \tag{2.4}$$

$$\frac{\partial \theta}{\partial t} + u\frac{\partial \theta}{\partial x} + v\frac{\partial \theta}{\partial y} + w\frac{\partial \theta}{\partial z} = 0 \tag{2.5}$$

where $\bar{v}$ is the velocity vector (u, v, w), u is the zonal wind component, v is the meridional wind component, w is the vertical velocity, ρ is the density, p is the pressure, θ is the potential temperature, and $f \approx 1.25 \times 10^{-4}$ at $60°N$ is the Coriolis parameter. Potential temperature changes with height according to the Poisson relation, $\theta = T\left[\frac{p_0}{p}\right]^{\frac{R}{c_p}}$, where T is the air temperature, R is the gas constant for dry air, and c_p is the specific heat for dry air. To be able to simplify the above Equations 2.1 to 2.5 the assumption of two-dimensionality is made, assuming motion only in x- and z-direction, where the mean variables are uniform in x-direction. Further, the

background density is considered constant, the rotational effects are neglected, and all fields variables are splitted into two parts, a mean and a perturbation:

$$\begin{aligned} u &= \bar{u}(z) + u'(x,z), \\ w &= w'(x,z), \\ p &= \bar{p}(z) + p'(x,z), \\ \rho &= \rho_0 + \rho'(x,z), \\ \theta &= \bar{\theta}(z) + \theta'(x,z). \end{aligned} \tag{2.6}$$

The latter requires the basic state variables ($\bar{u}$, $\bar{p}$, $\bar{\rho}$ and $\bar{\theta}$) to be in hydrostatic balance when the perturbations (u', w', p', ρ' and θ') are set to zero. In addition, the perturbations must be so small that any term involving products of perturbations can be neglected ($x'^2 \ll 1$). With these assumptions, and inserting the divided field variables (Equation 2.6) into Equations 2.1 to 2.5, the new equations are

$$\bar{u}\frac{\partial u'}{\partial x} + w'\frac{\partial \bar{u}}{\partial z} + \frac{1}{\rho_0}\frac{\partial p'}{\partial x} = 0, \tag{2.7}$$

$$\bar{u}\frac{\partial w'}{\partial x} + \frac{1}{\rho_0}\frac{\partial p'}{\partial z} - B = 0, \tag{2.8}$$

$$\frac{\partial u'}{\partial x} + \frac{\partial w'}{\partial z} = 0, \tag{2.9}$$

$$\bar{u}\frac{\partial \theta'}{\partial x} + w'\frac{\partial \bar{\theta}}{\partial z} = 0, \tag{2.10}$$

where $B = -\frac{\rho'}{\bar{\rho}}g \approx \frac{\theta'}{\bar{\theta}}g$ is the buoyancy[1]. Equations 2.7 to 2.10 can be combined to give a wave equation for either of the perturbed variables (u', w', p', ρ' or θ'). As an example, the wave-equation for w' is:

$$\frac{\partial^2 w'}{\partial x^2} + \frac{\partial^2 w'}{\partial z^2} + l^2 w' = 0, \tag{2.11}$$

where

$$l^2 = \frac{N^2}{\bar{u}^2} - \frac{1}{\bar{u}}\frac{d^2\bar{u}}{dz^2} \tag{2.12}$$

is the Scorer-parameter. This parameter will determine the wave pattern of the flow. $N^2 = \frac{g}{\bar{\theta}}\frac{d\bar{\theta}}{dz}$ is the Brunt-Väisälä frequency, or buoyancy frequency, for the background field. This parameter indicates at which frequency a vertically displaced air parcel will oscillate whithin a stable enviroment. The atmosphere needs to be stable to be able to produce buoyance waves, which means that N needs to be positive. Equation 2.11 can be solved by seeking a wave solution on the form;

$$w' = \Re\left\{\sum_k \tilde{w} e^{i(kx+mz+\omega t)}\right\}, \tag{2.13}$$

[1]Buoyance of an air parcel depends on the temperature and humidity, and the buoyancy force therefore depends on the surrounding density

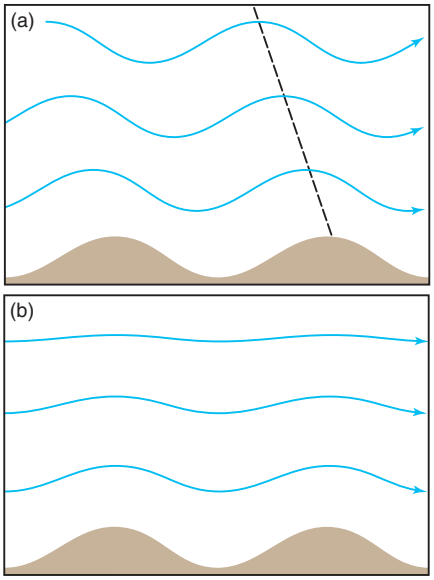

Figure 2.1: The streamlines over an infinite series of sinusoidal ridges. a) shows the case where the vertical wave number, m, is a real, and the case where m is an imaginary number, b). Figure adapted from Durran (1990).

where only the real part of the solution will be retained (represented by $\Re$ in Equation 2.13). The complex amplitude, $\tilde{w}$, consists of one real and one imaginary part ($\tilde{w} = \tilde{w}_r + i\tilde{w}_i$), ω is the wave frequency, k and m are the wave numbers in the x- and z-direction, respectively. By inserting Equation 2.13 into Equation 2.11 the vertical wave structure ($\tilde{w}e^{imz}$) can be detected;

$$m^2 = l^2 - k^2, \tag{2.14}$$

where m can be either real or imaginary, and the two outcomes will produce fundamentally different soultions. As long as $l^2 < k^2$, m is imaginary, and the solution will be waves that grow or decay exponentially with height:

$$w' = \tilde{w}e^{-m_i z}e^{ikx}. \tag{2.15}$$

The minus in front of m prevents the amplitude from increasing exponantially with height, which is an unphysical solution (lower panel of Figure 2.1). If $l^2 > k^2$, m is real and the solution will be a two-dimensional wave, propagating in both x- and z-direction (upper panel of Figure 2.1):

$$w' = \tilde{w}e^{i(kx+m_r z)}. \tag{2.16}$$

2.2 The Rossby Number and the Effect of Rotation

The Coriolis force is a measure of the rotational effect on the flow. When the Euler equation is used in a rotating frame of reference, combined with the geostrophic equation, the horizontal components of the equation can be written as:

$$\frac{Du}{Dt} = f(v - v_g) = fv_a, \tag{2.17}$$

$$\frac{Dv}{Dt} = -f(u - u_g) = -fu_a, \tag{2.18}$$

where f is the Coriolis parameter, u_g and v_g are the zonal and meridional component of the geostrophic wind, respectively, and u_a and v_a are the ageostrophic parts of the flow, such that $u = u_g + u_a$ and $v = v_g + v_a$. These equations (Equations 2.17 and 2.18) indicate that the acceleration of the flow is given by the difference between the actual wind and the geostropic wind. This means that a change in the u-component of the flow is given by the magnitude of the ageostrophic part of the v-component times the Coriolis force, and vice versa for the other component. The importance of the Coriolis force in the flow, can be evaluated by a scale analysis. The non-dimensional Rossby Number is given by

$$Ro = \frac{U}{f_0 L}, \tag{2.19}$$

where U, L and f_0 is the characteristic velocity, length scale and Coriolis parameter, respectively, for the situation of interest. The rotational effects are neglegctible when $Ro \gg 1$, and a flow that approaches an obstacle will be symmetric around it. On the other hand, for $Ro \ll 1$ the rotational effects are large and the flow will be asymmetric around the same obstacle. The Rossby Number can also be interpreted as the reliability of the geostrophic approximation. The smaller the acceleration of the flow is, the smaller the difference between the actual wind and the geostrophic wind (see Equations 2.17 and 2.18), and the Rossby number will be small as well. The replacement of the actual wind with its geostrophic value is then a good approximation. This is often done when the flow is away from boundaries and away from the equator. The flow is then determined by the strength of the large-scale pressure field.

2.3 Blocking and Flow Splitting

The parameters that decide whether an air parcel will go around or traverse over a mountain barrier are the strength of the wind, the height of the parcel relative to the height of the mountain (the distance to climb), the aspect ratio of the mountain (ratio between crosswise and streamwise dimensions), and the stratification of the atmosphere. If the flow has too low kinetic energy (the upstream wind is too weak) the air parcels will not be able to traverse over the mountain. Likewise, if the stratification is too strong and the distance to be climbed is too large. A parameter that also can

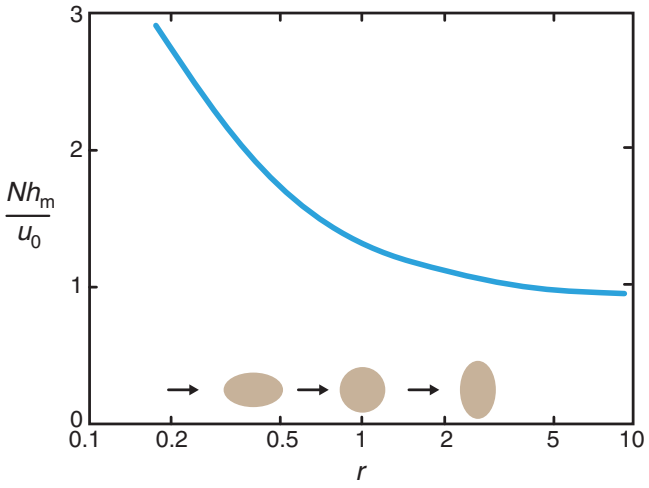

Figure 2.2: The stagnation line as a function of the non-dimensional mountain height $\hat{h} = \frac{Nh_m}{u_0}$ and the aspect ratio r (Markowski and Richardson, 2011; Smith, 1990).

tell something about blocking and stagnation is the non-dimensional mountain height,

$$\hat{h} = \frac{Nh_m}{\bar{u}}, \tag{2.20}$$

where h_m is the height of the mountain, N is the atmospheric stratification and $\bar{u}$ is the upstream value of the flow speed. The non-dimensional mountain height is a measure of the non-linearity produced in a flow. Linear theory is said to be trustworthy when $\hat{h} \ll 1$. In other words: To produce a plausible result in shallow water theory, the upstream wind velocity ($\bar{u}$) must be much larger than the stratification (N) times the mountain height (h_m). Barstad and Grønås (2005) expected three different flow regimes depending on the magnitude of the non-dimensional mountain height: $\hat{h} < 1$ led to gravity waves formation, $\hat{h} \gg 1$ cause upstream stagnation and flow splitting followed by a downstream wake, and $\hat{h} \approx 1$ resulted in strong downslope winds, high drag over the mountain, stagnation aloft and breaking gravity waves due to the large amplitude of the waves. They expected all the three flow regimes to occure over Southern Norway, for normal values of $\bar{u}$ and N, and $h_m \approx 1000\,\mathrm{m}$.

As mentioned above, the aspect ratio of the mountain also plays a crucial role in blocking and stagnation of the flow. The aspect ratio can be defined as the ratio between the crosswise and streamwise dimension of the mountain,

$$r = \frac{L_{cr}}{L_{st}} \tag{2.21}$$

where L_{cr} and L_{st} denotes crosswise and streamwise dimensions, respectively. When looking at Figure 2.2 it can be seen that as the aspect ratio (r) increases, which means that the flow is impinging the major axis of the mountain, then for a given non-dimensional mountain height $\hat{h}$, blocking of the flow will be more likely to happen. This figure also shows that stagnation only starts when $\hat{h} \approx 1$ for very large r. This means that as long as $\bar{u} > Nh_m$ (Equation 2.20), a complete stagnation of the flow

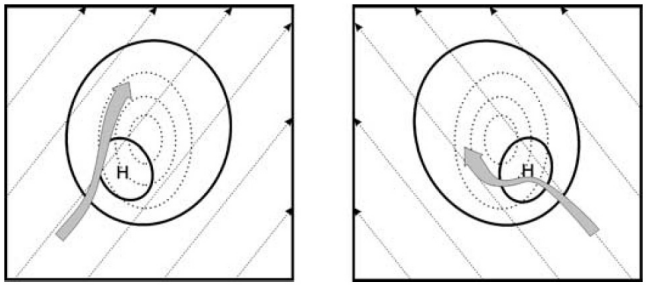

Figure 2.3: The different behavior of a flow, when the upstream wind direction is southwesterly (left panel), and southeasterly (right panel). (Barstad and Grønås, 2005)

will not occur.

Another parameter that can have an impact on the interaction between flow and topography is the effect of the Coriolis force. Barstad and Grønås (2005) also investigated whether an air stream was more likely to be blocked when it came from certain directions. They looked at an idealized obstacle with elliptical contours, where the major axis was located in the north-south direction. Figure 2.3 shows this setup. They concluded that when the air approached this obstacle from southeast it was more likely that this flow was going to be blocked compared to the air coming from southwest. Furthermore, Barstad and Grønås argue that the reason for this direction-preferable blocking was due to the fact that when a flow approaches a barrier it gets slowed down and deflected to the left by the background pressure gradient force. When the flow comes from southwest it gets deflected to the left and the flow continues in a northward direction. As the flow goes northward, the Coriolis force will increase making the flow turn slightly to the right. This makes the air climb the mountain, but now it climbs a narrower mountain, which makes blocking less likely. When the flow has a southeasterly direction, this leftward deflection of the flow as it approaches the barrier makes the air climb the mountain on a broader and higher place. As it climbes, it gains more potential energy, and slows down. Thus, it is more likely that the flow will be blocked.

2.3.1 Corner Winds

Nigro et al. (2012) stated *"A corner wind is an asymmetric flow around an obstacle, or barrier. In the Northern Hemisphere, the majority of the flow passes on the left side of the barrier (when looking downstream with the flow), whereas a minimal amount of the flow passes on the right side of the barrier"*. The reason for this asymmetry is an imbalance between the pressure gradient force and the Coriolis force. This imbalance arises because of a terrain-induced high pressure region on the windward side of the barrier, created by the interaction of the flow with the obstacle. This high pressure region can be thermally induced, it can be formed by momentum transfer from the flow to the mountain, or it can be produced by conservation of potential vorticity with stretching and compression of air columns. This region of high pressure perturbation slows down the wind due to conservation of Bernoulli's

equation (see Section 2.5). Further, this leads to a weakening of the Coriolis force, since the Coriolis force is a function of the wind speed. This implies that the Coriolis force no longer will be able to balance the pressure gradient force and the flow will deflect in the direction of the pressure gradient force. Once the flow passes the left corner, the flow is in the background pressure field again and not slowed down by the terrain-induced high pressure. The flow will accelerate, exceeding the upstream value, because the flow has a component in the direction of the pressure gradient force, created by the high pressure region infront of the mountain. Barstad and Grønås (2005) studied ideal flows passing over Southern Norway and the importance of the Earth's rotation in the intermediate range of $Ro \approx 1$. The different flows were characterized by a left-side jet or a corner wind, an upstream minimum on the right side of the mountain and a downstream wake caused by inertia gravity waves, flanked by a region to the right with enhanced wind speed. They concluded that the Coriolis force was an important parameter in determining whether air approaching the mountain would be blocked or not. The Coriolis force actually delayed the onset of upstream blocking as $\hat{h}$ increased.

2.4 Hydraulic Theory

Strong winds "on the lee side", as a consequence of stratified fluid impigning over a mountain barrier, has been studied for many years (e.g., Scorer, 1949; Long, 1954)). The linear theory described in the section above holds for infinitesimal perturbations of the dependent variables from their background values. Long (1954) showed that the linear theory also holds for larger perturbations. By taking use of Equation 2.1 and Equation 2.4, assuming a steady state solution[2], expressing the pressure in terms of the terrain height h and the depth of the fluid H, and requirering a constant mass flux[3], the one-dimensional equations for shallow water arise:

$$u\frac{\partial u}{\partial x} + g\frac{\partial}{\partial x}(H+h) = 0 \tag{2.22}$$

$$\frac{\partial}{\partial x}(uH) = 0 \tag{2.23}$$

By combining the two equations above it is possible to relate the acceleration of the flow to changes in the height of the free surface H;

$$\left(1 - Fr^2\right)\frac{\partial H}{\partial x} = -\frac{\partial h}{\partial x}, \tag{2.24}$$

where $Fr = \frac{u}{c}$ is the Froude number, the ratio between the upstream wind speed u and the gravity wave phase speed c. The Froude number can be used to distinguish between three different flow regimes: A supercritical regime, a subcritical regime and a transitional regime. When $Fr^2 > 1$ while traversing the mountain barriere, the

[2]This is plausible because the source that drives the waves is stationary, then after some time the wave pattern will also be stationary.

[3]In the mean flow direction, here x-direction.

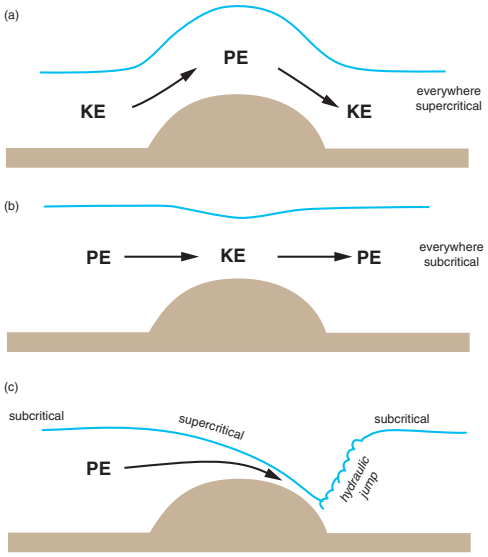

Figure 2.4: Three different flow regimes in hydraulic theory. a) Supercritical regime, b) Subcritical regime and c) Transitional regime. The figure also shows the distribution of the flows kinetic energy (KE) and potential energy (PE). Figure adapted from Durran (1990).

flow is said to be in the supercritical regime (Figure 2.4a). It means that when the flow climbs the windward side, $\frac{\partial h}{\partial x} > 0$, then from Equation 2.24 this implies that $\frac{\partial H}{\partial x} > 0$. The fluid is then thickest on top of the mountain, and from conservation of mass (Equation 2.23) this will lead to a decrease in u. When the flow descends down the lee side the thickness of the fluid layer decreases and the flow accelerates back to its upstream value. If $Fr^2 < 1$ the flow is said to be in the subcritical regime. From Equation 2.24 and Equation 2.23 the highest u is reached at the mountain top before it returns to its original value in the lee of the barrier (Figure 2.4b). When the flow undergoes a transition the flow starts out in the subcritical regime ($Fr^2 < 1$). At the same time the Froude number needs to be so close to unity that when the air climbs the windward side of the mountain, u increases and leads to $Fr^2 > 1$. The flow transitions into the supercritical regime when the mountain top is reached. As the fluid starts descending down the lee side it will continue to accelerate. This results in a lee wind that exceeds its upstream value. As in both the above regimes, the air parcels in the fluid need to return back to its equilibrium height when the fluid reaches the lee side. In the transitional regime, this leads the flow into a so-called hydraulic jump (Figure 2.4c). When such a jump occurs, the energy is dissipated through turbulent motion, the fluid thickness increases, and u returns to its upstream value, creating a wake downstream of the mountain containing slower air. (Markowski and Richardson, 2011).

An equation indicating the balance between the kinetic energy (KE) and the potential energy (PE) of the flow can be obtained by integrating Equation 2.22. The distribution of KE and PE in the different flow regimes is illustrated in Figure 2.4.

2.4.1 Gap Flows

In the vicinity of mountains, topographic features like fjords and valleys usually also exist, and a gap flow is flow that has been influenced by these fjords and valleys. Pan and Smith (1999) defined a gap wind as a jet of air, faster than adjacent air streams, which occur downstream of a gap. A wake, on the other hand, is defined as a region of slower air formed in the lee of a barrier. The wind speed can reach anomalously high values in fjords and valleys. The acceleration of the flow is usually caused by along-gap pressure gradients from the large-scale flow regime, where a stronger along-gap pressure gradient force provides a stronger gap flow. This kind of flow-acceleration can also happen in the presence of cold-air surges, i.e., when there is a significant cross-barrier temperature difference.

From the linear theory and the Froude number (defined in Section 2.4), it is possible to get an answer to why and where in the gap you might expect an acceleration of the flow. Similar as for hydraulic jumps, a gap wind require a transition in the Froude number. In linear theory, where mass is conserved,

$$(b \times h \times u) = constant. \tag{2.25}$$

b is the fjord or valley width, h and u are the height and speed of the flow, respectively. This equation will give an idea on where these strong winds might be expected. To get these strong, accelerating winds, $(b \times h)$ needs to be small in order for u to compensate. This means that the strongest wind will appear just downstream of the valley or fjord mouth, and not where the channel is narrowest, because the height (h) compensates for the decrease in width (b) (Markowski and Richardson, 2011).

Gabersek and Durran (2004) looked at four different gap flows resulting from four different non-dimensional mountain heights. The results are shown in Figure 2.5. When $\hat{h} = 0.25$ (Figure 2.5a), called the linear regime, mountain waves were present but no wave breaking occurred. The deviation of the streamlines was small and no distinct jet was present, neither in the center nor at the gap exit. When $\hat{h} = 1.4$, the atmosphere was in the mountain-wave regime (Figure 2.5b); wave breaking occurred, creating high winds down the lee slope of the barrier, which ended abruptly in a hydraulic jump. The flow accelerated all the way through the gap, especially at the gap exit, making these winds exceed their upstream value far downstream of the gap exit. This elongated area of strong winds were flanked by turbulent wakes of slow and even reversed flow. When $\hat{h} = 5$ (Figure 2.5d), which they called the upstream-blocking regime, the amplitude of the lee-waves was negligible and the strength of the gap-exit flow was even lower than the upstream wind speed. The strongest wind was here located in the center of the valley, slightly shifted towards the entrance of the gap. The intermediate regime $\hat{h} = 2.8$ (Figure 2.5c) was a mixture of $\hat{h} = 1.4$ and $\hat{h} = 5$ regimes. The wave breaking was reduced, and the high winds at the gap-exit did not extend as far downstream as in the mountain-wave regime.
They also investigated the mass fluxes and the momentum fluxes in and out of three

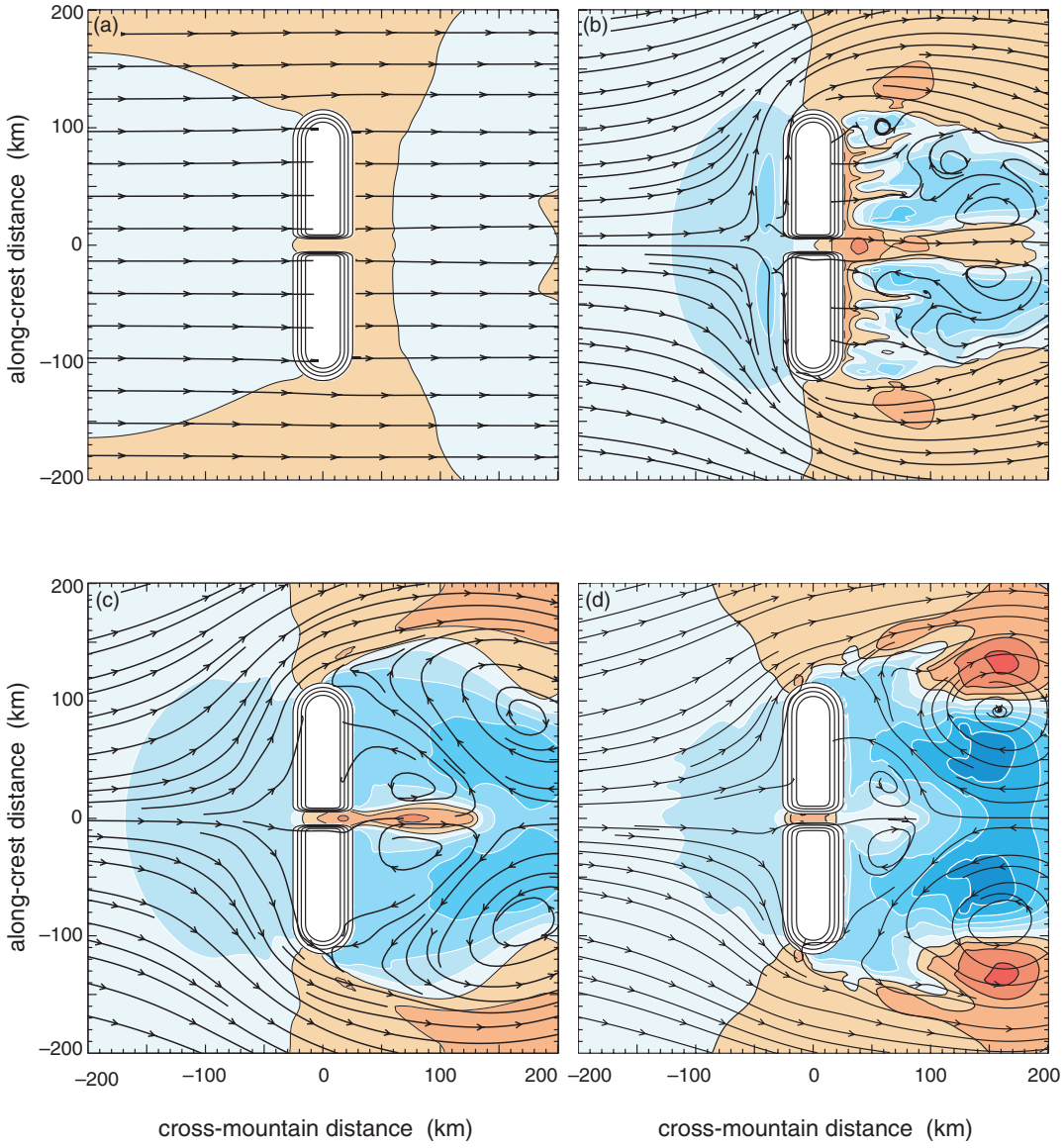

Figure 2.5: Flow through a gap modeled for four different flow regimes; a) the linear flow regime, $\hat{h} = 0.25$, b) mountain-wave regime, $\hat{h} = 1.4$, c) intermediate regime, $\hat{h} = 2.8$ and d) the blocking regime, $\hat{h} = 5$. Figure retrieved from Gabersek and Durran (2004).

control volumes, and concluded that the reason for this acceleration in the wind was due to lateral confluence and sinking motion towards the gap exit.

2.5 Bernoulli's Equation

Another concept that can link the thickness of the fluid layer to changes in the wind speed is the Bernoulli equation;

$$\underbrace{\rho_0 \frac{u^2}{2}}_{\text{A}} + \underbrace{p}_{\text{B}} + \underbrace{\rho_0 g z}_{\text{C}} = C, \tag{2.26}$$

which claims that the relationship between a parcel's kinetic energy (A), pressure (B) and potential energy (C) is conserved along a parcel trajectory. Since the potential temperature (θ) is more often conserved along a trajectory compared to the air density (ρ), it can be more convenient to express Equation 2.26 in terms of the non-dimensional Exner function, $\pi = \left(\frac{p}{p_0}\right)^{\frac{R}{c_p}}$;

$$\frac{u^2}{2} + c_p \theta \pi + g z = C. \tag{2.27}$$

Equation 2.27 is conserved along an isentropic surface[4]. From Equations 2.26 to 2.27 an increase in the wind speed is either balanced by a decrease in potential energy (descending of the air) or a decrease in pressure, or both.

Gabersek and Durran (2004) used Bernoulli's function along isentropic surfaces to investigate the acceleration of the flow through a gap in the mountain wave regime ($\hat{h} = 1.4$). Equation 2.27 can be written on the form;

$$\frac{u_{ex}^2}{2} = \frac{u_{en}^2}{2} + \underbrace{c_p \left(T_{en} - T_{ex}\right)}_{\text{A}} + \underbrace{g \left(z_{en} - z_{ex}\right)}_{\text{B}}, \tag{2.28}$$

where u_{en}, T_{en} and z_{en} are the values at the entrance of the gap and u_{ex}, T_{ex} and z_{ex} denotes values at the gap exit. Equation 2.28 states that by following an isentropic surface u_{ex} will exceed u_{en} whenever the temperature at the gap exit is lower than the temperature at the gap entrance. The parcel also need to descend as it approaches the gap exit, such that $z_{en} > z_{ex}$. Because descending air compresses and adiabatically warms when entering a region of higher pressure, the kinetic energy term counteracts the pressure term in Equation 2.28. Gabersek and Durran (2004) concluded that to get an acceleration of the flow, the descent of air as it passes through the gap must count for much more than the corresponding warming of the air.

[4]Isentropic surface is a surface of constant potential temperature.

Chapter 3

Methods

3.1 The Weather Research and Forcasting Model (WRF)

The following information and description of the WRF model follow Skamarock et al. (2008), if nothing else is stated. The Weather Reasearch and Forcast model is used for both numerical weather prediction and atmospheric research. WRF was developed to advance the understanding and to improve the prediction of mesoscale weather. The building of the model is a collaboration between the National Center for Atmospheric Research's (NCAR) Mesosale and Microscale Meteorology (MMM) Division, the National Oceanic and Atmospheric Administration's (NOAA) National Centers for Environmental Prediction (NCEP) and Earth System Reasearch Laboratory (ESRL), the department of Defense's Air Force Weather Agency (AFWA) and Naval Research Laboratory (NRL), the Center for Analysis and Prediction of Storms (CAPS) at the University of Oklahoma, and last but not least the Federal Aviation Administration (FAA), with the participation of university scientists. WRF is maintained and supported as a community model to facilitate wide international use for research, operation at weather forcasting and teaching. It is suitable for a broad span of applications across scales ranging from large-eddies to global simulations.

Figure 3.1 shows the different components in the WRF system, with the two dynamical solvers, ARW (Advanced Research WRF) and NMM (Nonhydrostatic Mesoscale Model). The ARW solver is often used for both real and idealized cases, and is used in this thesis.

3.1.1 Governing Equations

The ARW dynamics core integrates the incompressible, nonhydrostatic Euler equations[1]. The equations are formulated using a terrain-following mass vertical coordinate (Laprise, 1992), η, which is defined as

$$\eta = (p_h - p_{ht})/\mu, \tag{3.1}$$

[1]The ARW solver was originally referred to as the Eulerian mass or "em" solver.

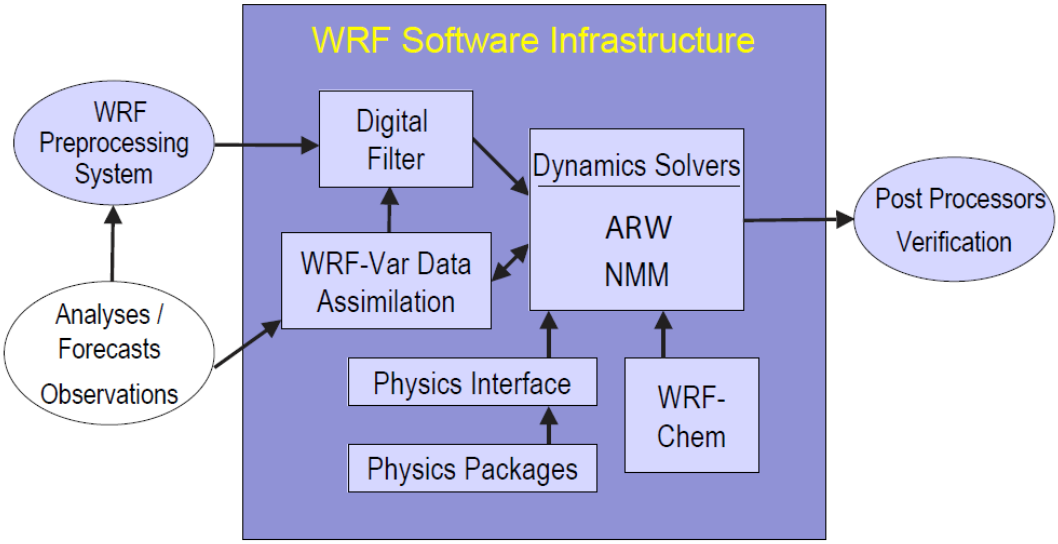

Figure 3.1: The components in the WRF system. Figure retrieved from Skamarock et al. (2008).

where p_h denotes the part of the pressure which is in hydrostatic balance, $\mu = p_{hs} - p_{ht}$ is the difference between the pressure at the surface (p_{hs}) and at the top boundaries (p_{ht}), varying from 0 at the top boundary to 1 at the surface. This way of expressing the vertical coordinate is called sigma-coordinates. This means that the pressure is the dependent variable instead of the height, z, and it allows the flow to follow the terrain (Figure 3.2).

Since mass per unit area, within the air column in the model domain at (x, y) is given by $\mu(x, y)$, the flux form variables are given by

$$\mathbf{V} = \mu\mathbf{v} = (U, V, W), \qquad \Omega = \mu\dot{\eta}, \qquad \Theta = \mu\theta, \tag{3.2}$$

where $\mathbf{v} = (u, v, w)$ are velocities in a three dimensional flow, while $\dot{\eta} = \omega$ is the vertical velocity in a terrain-following coordinate system[2], θ is the potential temperature. Other variables that also appear in the gouverning equations used in the ARW solver are the non-conserved variables: pressure, geopotential and the inverse density, defined and denoted by p, $\phi = gz$, and $\alpha = 1/\rho$, respectively.

By using the above defined variables the flux-form of the Euler equations can be written as

$$\frac{\partial U}{\partial t} + (\nabla \cdot \mathbf{V}u) - \frac{\partial}{\partial x}\left(p\frac{\partial \phi}{\partial \eta}\right) + \frac{\partial}{\partial \eta}\left(p\frac{\partial \phi}{\partial x}\right) = F_U, \tag{3.3}$$

$$\frac{\partial V}{\partial t} + (\nabla \cdot \mathbf{V}v) - \frac{\partial}{\partial y}\left(p\frac{\partial \phi}{\partial \eta}\right) + \frac{\partial}{\partial \eta}\left(p\frac{\partial \phi}{\partial y}\right) = F_V, \tag{3.4}$$

$$\frac{\partial W}{\partial t} + (\nabla \cdot \mathbf{V}w) - g\left(\frac{\partial p}{\partial \eta} - \mu\right) = F_W, \tag{3.5}$$

[2]The vertical velocity in a terrain following coordinate is the component of the flow perpendicular to the terrain, and is therefore not neccessary in the same/opposite direction as the gravitational acceleration force.

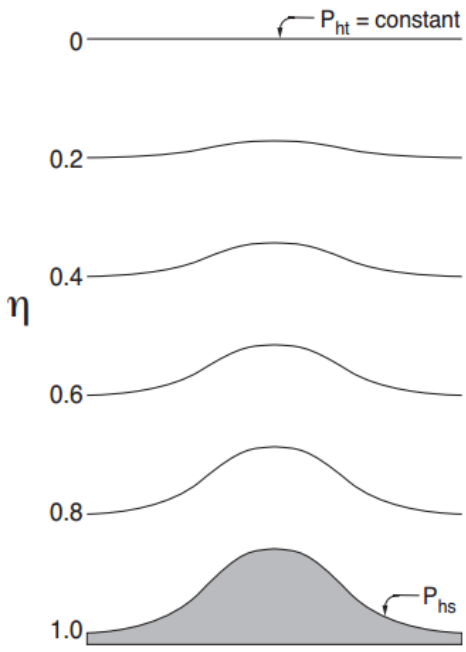

Figure 3.2: The sigma-coordinate, and how it follows the terrain. Figure retreived from Skamarock et al. (2008).

$$\frac{\partial \Theta}{\partial t} + (\nabla \cdot \mathbf{V}\theta) = F_\Theta, \tag{3.6}$$

$$\frac{\partial \mu}{\partial t} + (\nabla \cdot \mathbf{V}) = 0, \tag{3.7}$$

$$\frac{\partial \phi}{\partial t} + \frac{1}{\mu}\left[(\mathbf{V} \cdot \nabla\phi) - gW\right] = 0, \tag{3.8}$$

$$\frac{\partial \phi}{\partial \eta} + \alpha\mu = 0, \tag{3.9}$$

$$p = p_0 \left(R_d\theta/p_0\alpha\right)^\gamma, \tag{3.10}$$

where $\gamma = c_p/c_v = 1.4$ is the ratio of the dry air heat capacity for constant pressure and volume. R_d is the gas constant for dry air, and p_0 denotes the reference pressure. The F_U, F_V, F_W and F_Θ represents the forcing terms arising from the model physics, turbulent mixing, spherical projections and the effect of the Earth's rotation. Equations 3.3 to 3.8 represents the prognostic equations cast in conservative flux form, except Equation 3.8 which is the total derivative of the definition of the geopotential.

3.1.2 Temporal and Spatial Discretization

The ARW solver uses a time-split integration scheme due to the large variation in the frequencies (wave lengths) in the atmosphere. The low-frequency modes are integrated in time using a third-order Runge-Kutta scheme (RK3), while the high-frequency acoustic modes are integrated over shorter time steps to maintain numerical stability ($u\Delta t \leq \Delta x$).

The ARW solver uses a staggered C-grid for the variables shown in Figure 3.3.

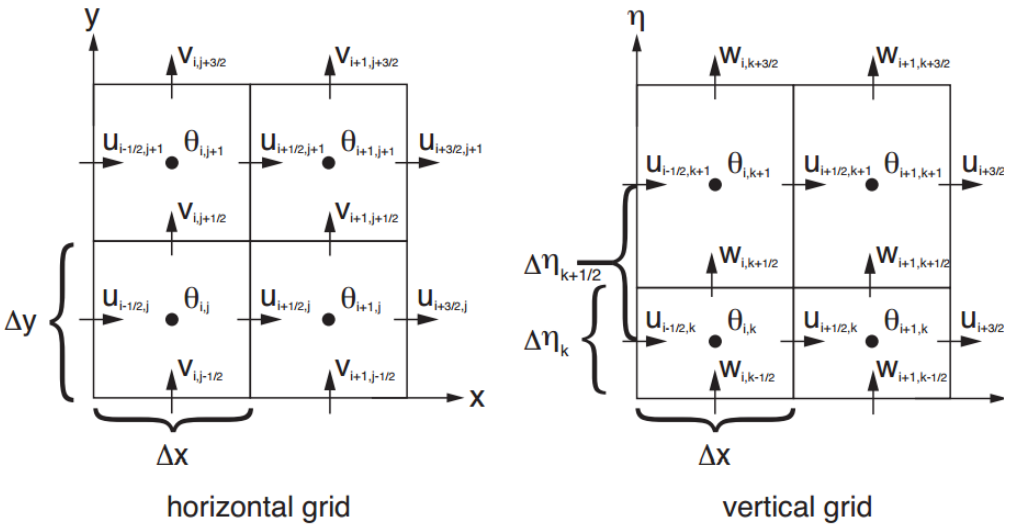

Figure 3.3: The staggered C-grid used in the spatial discretization in the WRF model. Figure retrieved from Skamarock et al. (2008).

Normal velocities (velocities normal to the boundaries of each grid box) are staggered one-half grid length from the thermodynamic variable, θ. The subscript (i, j, k) on the variables indicates the spatial location of the given variable with $(x, y, \eta) = (i\Delta x, j\Delta y, k\Delta\eta)$. The mass point will be defined as the center of each grid box (where θ is located in Figure 3.3), and the points where u, v and w sit will be defined as u-, v- and w-points, respectively. Not shown in the figure is the column mass, μ, which is defined at the mass point together with the moisture variable (q_m), pressure (p), and the inverse density (α). The geopotential ϕ is defined at the w-point.

3.1.3 WRF Preprocessing System (WPS)

When using the WRF model it is possible to choose to perform either an ideal or a real case. By running WRF Preprocessing System (WPS) the model is prepared for real-data simulation. The WPS consists of three programs; Geogrid, Ungrib and Metgrid, which are usually run in the respective order. The model domain is defined in the geogrid program, together with the interpolation of the statical terrestrial data sets to the model grid(s) and the choise of the projection of the selected area. Ungrib extracts time-varying meteorological fields from GRIB-formatted files, in this case ERA-Interim data from the ECMWF data server. Metgrid horizontally interpolates the meteorological fields extracted in ungrib to the simulation domain defined by geogrid. As an intermediate step between the WPS and WRF the Real program is run. This program interpolates vertically the meteorological fields to the WRF-eta (η) levels.

3.1.4 Specified Lateral Boundary Condition

The specified boundary condition, often used in real-data cases, is usually referred to as a relaxation boundary condition. In ARW this kind of boundary condition is

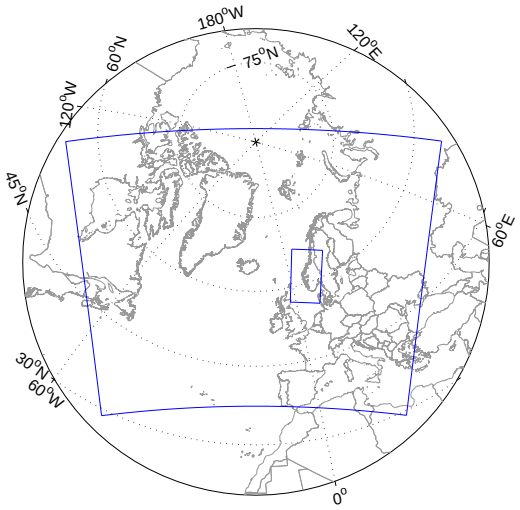

Figure 3.4: The two domains used in the WRF model. The largest domain has a grid-resolution of 10 km, while the inner domain has a grid-resolution of 2 km.

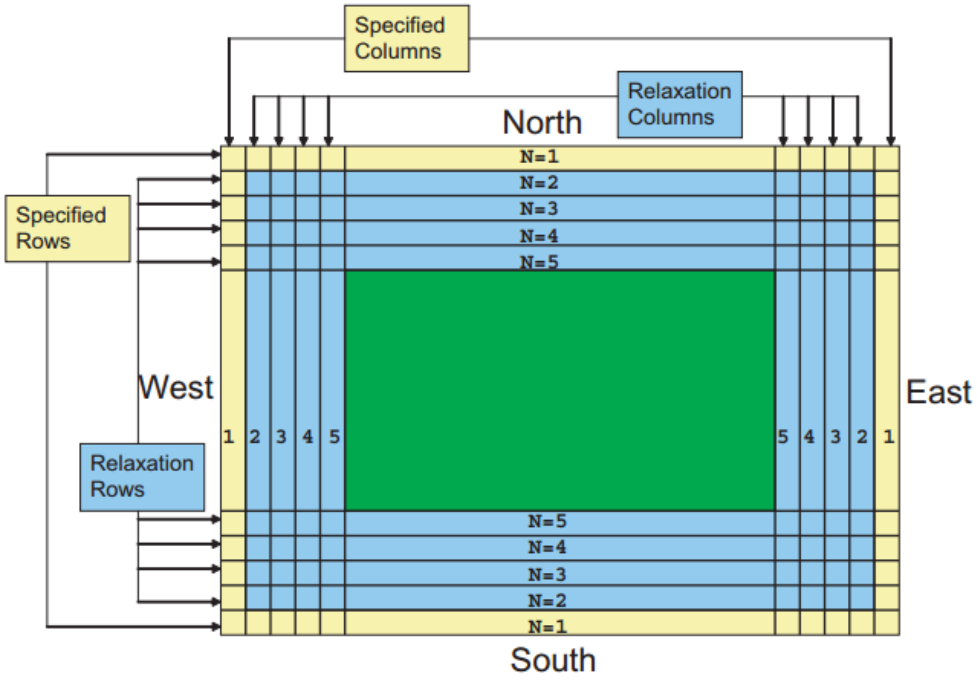

Figure 3.5: The specified and relaxation zones of the lateral boundary (Skamarock et al., 2008). The yellow rows/columns are the specified zone, which get information solely from the ERA-Interim reanalysis data. The next four rows and columns (blue) are the relaxation zone, and hence the data produced by the model in this region will be relaxed towards the ERA-Interim data.

applied either for the outer most grid or for the time-dependent boundaries supplied to a nested grid. In this thesis, only the coarse grid will have a specified lateral boundary. The specified lateral boundary for the coarse grid will include both a specified and a relaxation zone (Figure 3.5). In this case, for the coarse grid, the last row and column along the outer most edge is called the specified lateral boundary, and this will be determined entirely from the ERA-interim reanalysis data. The next four rows and columns (row/column 2-5 in Figure 3.5) are named the relaxation zone. This is the region where the model will be nudged or relaxed towards the ERA-Interim reanalysis data. In other words, the data in this region will then be a combination of the data produced by the WRF model and the ERA-Interim realanysis data. This is done to smoothen the transition zone between the external model and WRF.

3.1.5 Nesting

The ARW solver allows for horizontal nesting in the purpose of focusing on smaller domains inside a larger grid. There are two nesting options; 1-way nesting and 2-way nesting. These options determine how the coarse and fine grid communicate with each other. During both 1- and 2-way nesting the Lateral Boundary Conditions (LBC) of the fine grid are interpolated from the coarse grid. In 1-way nesting this is the only interaction between the two grids. Two different modes exist for 1-way nesting. The first mode treats the two grids separately; the model integrates the forcast of the coarse grid first. The output from the coarse grid is then used as LBC for the finer grid, followed by a complete time intergration. The second 1-way nesting option is a simulation where the integrations of the two grids happens at the same time. This means that the coarse grid provides LBC to the finer grid for every time step of the coarse grid. In 2-way nesting, the solution from the coarse grid is replaced by the solution from the fine grid for all that points that lies inside both the coarse-grid domain and the fine-grid domain.

3.1.6 Nudging of the Model Data

Spectral nudging is a way to force the entire domain of interest, and not just the boundaries, to adapt to the large-scale features of an external model (Radu et al., 2008). In other words, spectral nudging is a method used to keep the larger horizontal scales close to the analysis and/or observations when integrating. The smaller scales are not significantly affected by the nudging, allowing the model to freely generate features at smaller scales under the large-scale constraints (Berg et al., 2013). Initially, this method was an alternative for data assimilation, but it was also found to reduce the systematic model bias (Laprise et al., 2012; Berg et al., 2013). There are two types of spatial nudging: The first is the grid- or analysis-nudging, which forces the model simulation, grid-point by grid-point, towards a series of analysis. The other one is observational- or station-nudging, which forces the simulation towards the observed data. The observational nudging allows the model to effectively adapt the observations of temperature, wind and moistrure from all platforms, at any

location in the model domains at any time within the data assimilation period. With this nudging option, each observation directly interacts with the model equations.

3.1.7 The Model Setup

In this thesis the version 3.3.1 of the WRF model was used to study the topography's effect of the strong winds caused by Dagmar. The model setup was based on two nested domains, see Figure 3.4, where 1-way nesting was used. The lateral boundary conditions (LBC) were provided to the inner grid every time step (every 40 s). The outer (parent) domain had a horizontal extent of 6720 km in the east-west direction and 5490 km in the north-south direction, and covered almost the entire Northern hemisphere, with a horizontal grid resolution of 10 km. The inner (child) domain had a horizontal extent of 301 km in the east-west direction and 526 km in the north-south direction with a horizontal grid resolution of 2 km, and covered Southern Norway. In the vertical, the atmosphere was divided into 40 intervals, ending at 50 hPa. The first layer was 27.3 m (on average), and the atmosphere below 5000 m was divided into 16 layers. The timestep (Δt) was 40 s to remain numerical stability. To be able to study the effects of Dagmar, the model integration for the coarse domain started at 0000UTC the 25th of December 2011, and ended 27th of December 2011 at 1800UTC. This information was carried on to the fine grid as boundary information every time step, running from 25th of December 2011 at 0600UTC until 27th of December 2011 at 1800UTC. The spin up time was set to 6 hours, from the 25th at 0000UTC until 0600UTC. In this model run the spectral observational-nudging was used to nudge the model towards the ERA-Interim reanalysis data. Nudging was performed in all the vertical levels, and at every (40 s). The relaxation time was set to 56 min, meaning that after 56 min the modeled atmosphere was, on average, the same as the observed state of the atmosphere. Only the wavelengths longer than 671 km in the x-direction and 685 km in the y-direction were nudged. The inner domain was not spectrally nudged, this domain only got information through the boundaries from the parent grid, which means that the finer grid ran freely and generated its own meteorological features. The following section describes the WRF-Physics used in this thesis.

3.1.8 WRF Physics and Parameterization

A parameterization uses algorithmically or statistically procedures to solve the effects of the physical processes that cannot be directly represented in a model. The reasons for parameterize some of the physical processes are: the scale of the feature is so small, or that the process is too complex, such that it makes it too computational expensive to represent it directly. Insufficient knowledge, regarding a physical process and how it works, to explicitly represent it mathematically is another reason. The schemes listed below are the schemes used in the all the WRF runs.

Physics	Scheme
Microphysics	Thompson et al. (2004)
Short wave radiation	MM5 SW scheme
Long wave radiation	RRTM LW scheme
Cumulus parameterization	Kain–Fritsch Scheme
Surface layer	MM5 Similarity Scheme
Land-surface options	Unified Noah Land Surface Model
Planetary Boundary Layer	Mellor–Yamada–Janjic Scheme (MYJ)

Table 3.1: The parameterizations used in the WRF runs.

Cloud Microphysics

Cloud microphysics includes all processes that occur on the scales of cloud droplets and hydrometeors, and not on the scale of the cloud itself (Warner, 2011). The scheme used for these processes in all the three WRF runs is developed by Thompson et al. (2004). It is is a bulk microphysical parameterization scheme (BMP) which integrates seven variables, and takes into account both the ice-phase processes and the mixed-phase processes. The scheme by Thompson et al. (2004) assumes that the snow size distribution depends on both the ice water content and the temperature, and is therefore represented as the sum of exponential and gamma distributions. This schemes also assumes that the snow has a non-spherical shape with a bulk density that varies with the inverse of the snow crystal's diameter.

Cumulus Parameterization

To parametrize moist convection is of importance because intense convection can lead to hazardous features like flash flood, gust fronts, and tornadoes. The cumulus clouds have a large effect on the global albedo, and thus the radiation budget, and the effect of these clouds needs to be represented in weather and climate models (Warner, 2011). The cumulus parameterization is taken care of by the Kain-Fritsch (KF) scheme, which is a modification of the earlier Kain (2004) and Kain (1993). It uses a simple cloud-model with both moist up- and downdrafts. The cumulus clouds are only parametrized in the outer domain where the grid resolution is too coarse to resolve these type of clouds.

Radiation Parameterization

Radiation from the Sun is responsible for all the processes in the atmosphere, from Hadley circulation on the global scale, mesoscale buoyancy instabilities, to turbulent fluxes on the Earth's surface. Since the radiation interacts with the atmosphere on the molecular level, the processes are too small and too complex to be simulated directly (Warner, 2011).

Short Wave Radiation

The short wave radiation was parametrized by the MM5 short wave (SW) scheme, based on Dudhia (1989). It is based on a downward integration of the extraterrestrial radiation. It accounts for clear-air scattering, absorption of SW by water vapor, and cloud albedo and absorption.

Long Wave Radiation

The long wave radiation was taken into account by the RRTM (Rapid Radiative Transfer Model) scheme from the MM5, based on Mlawer et al. (1997). This is a spectral-band scheme taking use of the correlated-k method. The correlated-k method is a tecnique used for calculations of radiation in a non-homogenious atmosphere using spectrally average data (Goody et al., 1989). It uses pre-set tables to optimize the representation of longwave processes due to water vapor, ozone, CO_2, and trace gases. All this in addition to account for cloud optical depth.

Surface Layer

In the surface layer, molecular transport dominates over turbulent transport. These small scales features need to be parametrized, and the similarty scheme from MM5 was applied for that purpose. This sceme computes surface exchange coefficients for heat, moisture and momentum by using stability functions from Paulson (1970), Dyer and Hicks (1970) and Webb (1970). Convective velocities are used to enhance the surface fluxes of heat and moisture (Beljaars, 1995). In this current version of the sceme, no parameterization for the thermal roughness length is included. This scheme relates the roughness length to friction velocity over water through the Charnock relation. The Charnock relation is an empirical expression for aerodynamic roughness length $z_0 = \alpha_c u_\star^2/g$ over the ocean, where $u_\star$ is the friction velocity, g is the gravitational acceleration and α_c is called the Charnock parameter.

Land-Surface Options

Land-surface processes are parametrized because they occure on too small scales to be directly represented by the WRF model (Warner, 2011). The Unified Noah Land Surface Model (Noah LSM) is a successor to the OSU LSM described by Chen and Dudhia (2001). This model is a 4-layer soil temperature and moisture model, with both canopy moisture and snow cover prediction. The layer thickness are 10, 30, 60 and 100 cm (adding to 2m) from the top down. It takes care of the root zone, evapotranspiration, soil drainage and runoff. It also includes vegetaion categories, monthly vegetation fraction and soil texture. This scheme provide the boundary-layer scheme with sensible and latent heat fluxes. Different from the OSU scheme, the Noas LSM also predicts soil ice and fractional snow cover effects, improved urban treatment, and it considers surface emissivity properties.

Planetary Boundary Layer

The Earth's surface and the free atmosphere are connected through the Planetary Boundary Layer (PBL) of the troposphere. In the boundary layer turbulent eddies transport water vapor and heat, but also heat frictional stress is transported upwards by these turbulent eddies. The closure-problem of the equations used in the planetary boundary layer forces us to parametrize these features. In the WRF model, the turbulence in the PBL, and in the free atmosphere, is represented by a nonsingular implementation of the Mellor-Yamda 2.5 turbulence closure model (Mellor and Yamada, 1982).

3.1.9 Description of the Simulations

Three different model runs were carried out to investigate the effect of the complex topography in Southern Norway on the strongs winds caused by the storm Dagmar. The first model run simulated Dagmar with the best resolved topography (herafter referred to as "control run"). This was done to see how well the model captured what really happened the day Dagmar struck Southern Norway, and to get the reliability of the model. In the second model run the topography of Southern Norway was smoothed out (herafter "smooth topography run"), i.e. the complexity of the original topography was removed. This was done to see how the small scale variations in the topography, like steep tops and valleys, affected the wind speed and direction. The third model run simulated Dagmar when Norway's topography height was zero (herafter "flat topography run"). Then it was possible to see how the flow pattern and strength of the wind changed when the influence of a mountain was gone.

3.2 The Linear Wave Model

The linear wave model, developed by Idar Barstad in 2003 (Barstad and Grønås, 2005), is a model that simulates the interaction of a uniform flow with different topographies. The model solves the 3-D Navier-Stokes equations in a compressible atmosphere. The main purpose of this model is to obtain better understading of how a uniform flow is influenced by different topographies in varying atmospheric conditions. The model uses a fast fourier tranformation to obtain the analytic 3-D wave solutions for the different variables. Different parameters can be adjusted to obtain the desired atmospheric state; wind speed and direction, Coriolis parameter, stability of the atmosphere, hydrostacy, shape of the mountain, friction etc.

Five slightly different runs were conducted, testing how sensitive the wind pattern was to changes in the parameters. Table 3.2 shows the setup of the five scenarios. The friction was not included in these model runs, and a one-layer atmosphere in hydrostatic balance was used. The Coriolis parameter was the same for all the runs, $f = 1.26 \times 10^{-4}$, and the shape of the mountain was Gaussian elliptical. The half-length of the mountain in the x-direction was 100 km, while in the y-direction the half-length was 500 km, such that the aspect ratio of the mountain was $r = \frac{L_{cr}}{L_{st}} = 5$

(see Section 2.3 for more information about the aspect ratio). The initial state of the wind speed, wind direction and stability was uniform throughout the atmosphere.

The first run (Run1) was a simulation where the key parameters were as close as possible to the ones found in the case of Dagmar, hereafter called "the realistic run". Even though not all stations observed wind speed of hurricane strengt (>32.7 $\mathrm{m\,s^{-1}}$), the uptream wind speed was set to 32 $\mathrm{m\,s^{-1}}$, and the wind direction was westerly. The height of the mountain was 1500 m, and the atmospheric stability was set to 1.5 °K/1000 m in potential temperature. This was the control run, and all the other runs were compared to the results form this scenario. In Run2 the wind direction was changed, from westerly to southwesterly wind. Run3 was a scenario where the upstream wind speed was weaker, 18 $\mathrm{m\,s^{-1}}$ instead of 32 $\mathrm{m\,s^{-1}}$. In Run4, the height of the moutain was increased from 1500 m to 1800 m. The shape and the cross- and lengthwise dimensions were still the same. In the last run (Run5), the stability of the atmosphere (in potential temperature) was increased from 1.5 K/1000 m to 4 K/1000 m.

Parameter	**Run1**	**Run2**	**Run3**	**Run4**	**Run5**
Mnt. height	1500	1500	1500	1800	1500
u - comp	32	25	18	32	32
v - comp	0	20	0	0	0
Wind speed	32	32	18	32	32
Wind dir	270	231	270	270	270
Stability	1.5	1.5	1.5	1.5	4

Table 3.2: Information about the setup of the different runs performed by the linear wave model. The mountain height (Mnt. height) is given in meters, u- and v- components of the wind speed are given in $\mathrm{m\,s^{-1}}$, wind direction are given in degrees, and the atmospheric stability (in potential temperature) is given in K/1000 m.

Chapter 4

The Synoptic Situation and Observational Study

4.1 The Synoptic Situation

During the 25th and 26th of December 2011 two strong low pressure systems struck Norway. The storm "Cato" made landfall on Norway on the night of the 25th. Bjerknes and Solberg (1922) stated that a new low pressure system can develop in the tail of a cold front corresponding to an already exsisting low pressure system. In the tail of Cato's cold front a new system started to develop. This rapidly evolving system got the name "Dagmar". From the theory of cyclogenesis one of the factors that can strengthen an evolving system is cold air advection under the developing trough (Holton and Hakim, 2012). On Dagmar's way over to Norway there were several low pressure systems located to the north of Dagmar, and hence may have strengthened the system. In addition to this, a low pressure system developed west of Ireland (see Figure 4.1). Again, from the theory of cyclogenesis, in some cases, a low pressure system can develop downstream of another system. This is possible if the energy of the existing system, which travels with the group velocity, travels faster than the system itself. This energy is then avalible for the developing system (Holton and Hakim, 2012). Dagmar moved rapidly across the northern part of the Atlantic Ocean, and struck Norway the same evening.

From the Norwegian Meteorological Institute in Bergen the analysis for the evening on the 25th, at 1800UTC (Figure 4.1, left panel), and at 0000UTC the 26th (Figure 4.1, right panel) were retrieved to see how the system moved, and to see the corresponding fronts. At 1800UTC on the 25th, the center of Dagmar was located west of Trøndelag, see left panel of Figure 4.1. The corresponding occluded front was located over the northern part of Southern Norway, whereas the warm front to the southeast and the cold front to the southwest. At 1800UTC on the 25th the large scale wind direction over Southern Norway was westerly. The pressure minimum of Dagmar was at that time < 960 hPa. To the south of the low, the isobars were close together indicating strong wind impinging on the west coast of Southern Norway. The

occluded front was drawn to bend backwards, towards the western coast of Southern Norway. Cato was at that time located to the north of Dagmar and to the west of Troms, indicating cold air advection southwards, with a pressure minimum of $<$ 955 hPa. In the right panel, at 0000UTC the 26th, Dagmar had moved further inland and the center was located over Nordland. The pressure at the core of the system had increased from $<$ 960 hPa to $<$ 965 hPa. The occluded front was now positioned over Nordland and Trøndelag, the cold front along the eastern part of Southern Norway, while the warm front had passed into Sweden and Eastern Europe. The off shore large scale wind direction came from west to northwest, but turned to southwest at the coast. The veering of the wind, from 1800UTC the 25th until 0000UTC on the 26th, is in agreement with the theory that the wind direction turns clockwise as a low pressure system passes (Wallace and Hobbs, 2006). Cato was rather stationary, and was still located west of Troms. The pressure in the core of Cato had not changed much, and was still $<$ 955 hPa.

A numerical study on the storm that struck Norway on the New Year's eve in 1992 was carried out by Grønås (1995). This was the strongest storm that struck Norway during the previous century. This storm mainly affected the northwestern part of Southern Norway, like Dagmar. Grønås investigated the intensification of the non-frontal trough[1], which may happen in strong cyclones, in the area of frontolysis; when the cold air completely secludes the warm core from the bent-back warm front, the cyclone intensifies through a mesoscale lower tropospheric cyclogenesis. He found that the seclusion low (resulting from the non-frontal trough) developed a low level jet. The maximum wind speed was found to the south of the seclusion low. These strong winds might be a superposition of the jet from the seclusion low and the wind from the main low pressure itself. Later, this phenomena got the name "the poisonous tail of the back-bent occlusion".

A recent paper, written by Schultz and Sienkiewicz (2013), looked at something called a *sting jet*, which is very high wind speed south of the surface low center. The term referred to Grønås' invoation of "the poisonous tail of the back-bent occlusion". Schultz and Sienkiewicz claimed that it was two main processes that could trigger a sting jet; the frontolysis at the end of the back-bent warm front, with the resulting secondary circulation, and the role of the static stability to bring the higher momentum air to the surface. Not all low pressure systems get this intensification through a non-frontal trough or a sting jet. Due to the strong cold air advection with the extra help from Cato in the north, together with the low atmospheric stability at that time (this will be shown in Chapter 6), and the location of the strong surface winds in the frontolytic zone (see left panel of Figure 4.1), this may indicate that Dagmar was one of those systems that developed a sting jet.

[1] also known as the back-bent occlusion

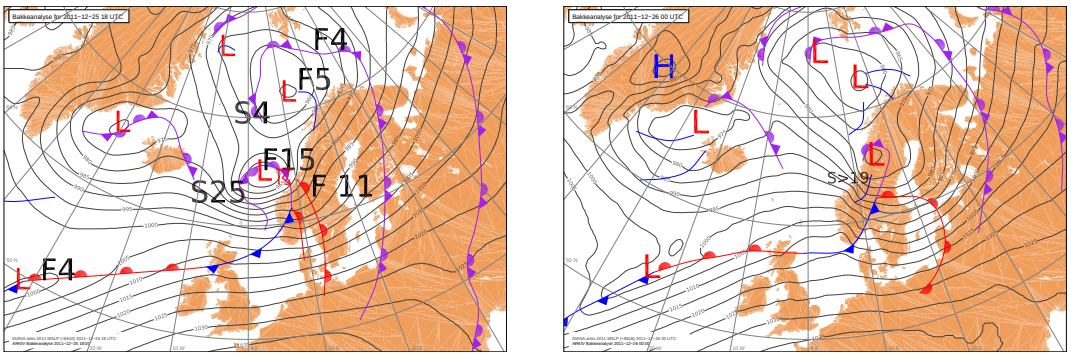

Figure 4.1: The analysis of the large-scale situation when Dagmar made landfall over Southern Norway. The left panel shows the reanalysis for the 25th of December 2011 at 1800UTC, while the right panel shows the situation six hours later, at 0000UTC the 26th. The figures show the surface pressure and the corresponding fronts. Analysis made by the Norwegian Meteorological Institute (Personal communication with Birgitte Furevik, Meteorological Institute.

4.2 Observations

The storm Dagmar affected almost all of Norway in one way or another, but the region of interest will be the Southern part, south of Nordland. The observational data were retreived from the Norwegian Meteorological Institute (MET, 2012), for the 48-h long period; 25th of December at 0000UTC until the 26th of December at 2300UTC. Most of the data were hourly values, but some stations had data only every third or every sixth hour. The original dataset consisted of 194 stations covering almost all of Norway (except some parts of Finnmark). All the stations used in the observational study are listed in Appendix A.

Left panel of Figure 4.2 shows the maximum instantaneous 10-m wind speed (10-min average), while the strongest 10-m wind gust[2] is shown in the right panel, during the period from 0000UTC the 25th until 2300UTC the 26th. The strongest wind gust was 64.7 $\mathrm{m\,s^{-1}}$, measured at Juvvasshø. The strongest 10-m instantaneous (10-min average) wind speed was 43.8 $\mathrm{m\,s^{-1}}$, measured at Kråkenes lighthouse. Figure 4.2 indicates that the northwestern part of Southern Norway and the mountain region were the two areas that was most affected by Dagmar. The two figures also indicate that the eastern and Southern part of Norway were sheltered from these strong winds. This is in agreement with the findings in Barstad and Grønås (2005).

As mentioned earlier, the mountain range Langfjella lies in the north-south direction dividing Southern Norway lengthwise into two regions. Blocking and splitting of the flow will occur when the wind has too little momentum, or the atmospheric stability is too strong for the wind to climb over the mountain, together with the influence of the wind direction (see Section 2.3 for more details). Depending on the wind direction, the Coriolis force also plays a role in determening whether the flow will be blocked or not (Barstad and Grønås, 2005, 2006). Friction plays a role in the east-west difference in the wind speed, in which the flow that affects the eastern

[2]strongest wind gust was here defined as the strongest instantaneous wind gust during one hour.

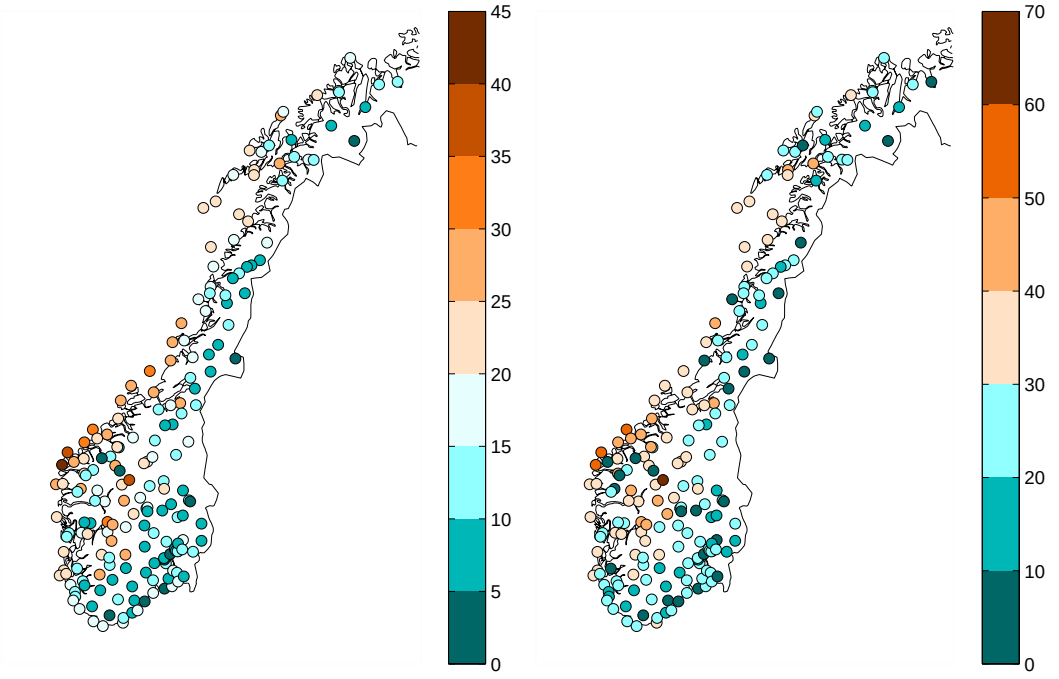

Figure 4.2: Left panel shows the maximum 10-m instantaneous (10-min average) wind speed in $\mathrm{m\,s^{-1}}$, the right panel shows and the maximum 10-m wind gust, from 0000UTC the 25th until 2300UTC the 26th.

part of Southern Norway usually has travelled across the country, from west to east, and will be slowed down due to higher friction over land. As a consequence, the part of Norway located to the west of Langfjella would on average experience higher wind speeds, especially during low pressure systems located in the Nordic Seas. This means that strong wind events in Norway, especially strong winds on the western side, are closely linked to the path of the low pressure systems. Because the low pressure systems form along the polar front (typically located around 60°N), Norway is particularly exposed to these systems.

Figure 4.3 shows the two strongest wind events during Dagmar. The strongest 10-m instantaneous (10-min average) wind was $43.8\,\mathrm{m\,s^{-1}}$ (Kråkenes lighthouse) measured at 1900UTC the 25th. From Figure 4.3 (left panel) it looks like there was a jet that formed along the northwestern coast of Southern Norway at that time. These high wind speeds could have been caused by the poisonous tail of Dagmar. Some hours later, at 2300UTC, the second strongest mean wind was observed, $38.9\,\mathrm{m\,s^{-1}}$, at Juvvasshø.

Figure 4.4 shows the wind directions, corresponding to the wind speed shown in Figure 4.3, for selected stations. Figure 4.4a corresponds to the left panel of Figure 4.3, while Figure 4.4b corresponds to the right panel of Figure 4.3. By looking at Figure 4.4a, the main wind direction was typically southwesterly. Some of the arrows indicate wind from aother direction, possibly caused by local effects. In Figure 4.4b, it is clear that Dagmar had moved further inland, due to the veering of the wind to a more westerly direction.

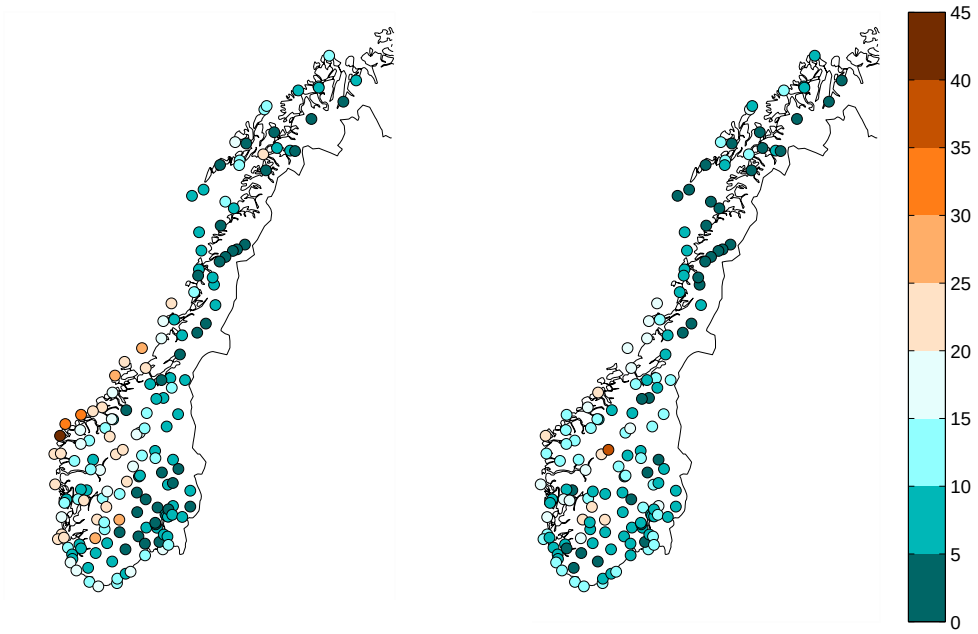

Figure 4.3: The two events with the strongest observed wind speed during Dagmar. Left panel shows the 10-m mean wind (10-min average) observed at 1900UTC on the 25th of December 2011, while the right panel shows the observed wind at 2300UTC, the same day.

Figure 4.6 shows the time series of wind speed, wind direction and wind gust for six selected stations: Veiholmen lighthouse, Kråkenes lighthouse, Utsira lighthouse, Lista lighthouse, Juvvasshø, and Oslo-Blindern (see Figure 4.5 for the location of the six stations). The selected stations were from various locations, and represented different heights above sea level. All six stations experienced an increase in both the wind speed and the wind gust when the wind direction turned into a more westerly direction, and decreased again when the wind turned anticlockwise back into a southewesterly direction. A possible reason for this might be that Dagmar developed a sting jet south of the back-bent occlusion, hence when the wind direction turns from a southwesterly direction into a more westerly wind. For Veiholmen, Figure 4.6a, the sensor broke down during the strongest wind gusts. This was also the case for several other stations.

The increase in the wind speed when the wind turned to a more westerly direction was most pronounced for the stations located along the western and northwestern coast. By looking at the analysis at 1800UTC the 25th (Figure 4.1, left panel), the strongest wind came from west, visible by the tight isobars south of the system. When this strong wind hit the stations along the coast the wind was less influenced by the higher friction over land, making those stations experience a higher wind speed than the stations further inland.

From Figure 4.6 it is seen that the stations located in the Southern and southwestern part (Lista lighthouse and Utsira lighthouse) were first affected by Dagmar, which

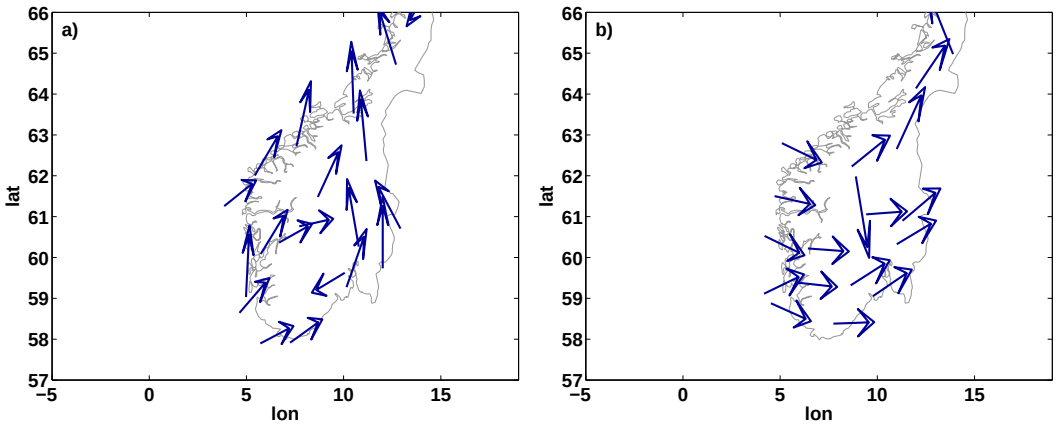

Figure 4.4: The wind directions for the 10-m instantaneous (10-min average) wind speed, for selected stations at 1900UTC (left panel) and 2300UTC (right panel) on the 25th of December 2011. The center of the arrow indicates the location of the corresponding station.

had their maximum wind speed before 1800UTC the 25th. The northwestern stations (Kråkenes and Veiholmen) had their maximum wind speed around 1800UTC the 25th, while Oslo-Blindern experienced the highest wind speed 6 hours later, around midnight. The station located up in the mountain (Juvvasshø) experienced high wind speed over a longer period than the other five stations. Juvvasshø also measured its maximum wind speed around midnight.

4.3 Pressure Impact on Buildings

Many houses and buildings got damaged and destroyed during the strong winds caused by Dagmar. The additional pressure on a building exposed to wind, can be estimated making use of a very simple form of Bernoulli's equation (see Chapter 2 for further explanation). Neglecting the influence of the height, the equation can be written on the following form;

$$\frac{\bar{\rho}}{2}U_1^2 + p_1 = \frac{\bar{\rho}}{2}U_2^2 + p_2, \tag{4.1}$$

where subscript 1 denotes upstream values and subscript 2 denotes values at the wall of the building. When calculating the maximum pressure that could be imposed by the wind, we assume that none of the oncoming air passes the building, i.e., a full stagnation of the flow occurs at the wall, and the flow hits perpendicular to the vertical buliding wall. Setting $\bar{\rho} = 1.18\,\mathrm{kg\,m^{-3}}$, $U_2 = 0\,\mathrm{m\,s^{-1}}$, $p_1 = 970\,\mathrm{hPa}$, and plugging these number into Bernoulli's equation, the pressure caused by a hurricane ($U_1 = 32.7\,\mathrm{m\,s^{-1}}$) will then be:

$$\frac{1.18}{2}32.7^2\mathrm{kg\,m^{-1}\,s^{-2}} + 970\,\mathrm{hPa} = 1600\,\mathrm{hPa}. \tag{4.2}$$

This means that the wall should withstand the weight of one half extra atmo-

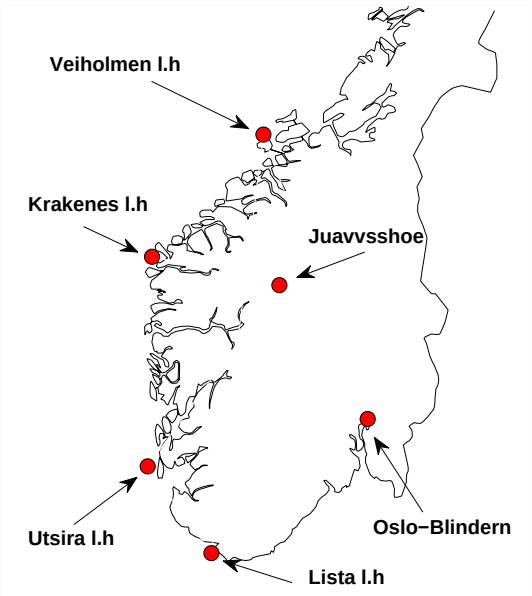

Figure 4.5: The location of the six selected stations. "l.h" is an abreviation for "lighthouse"

sphere. In other words; the wall should withstand an extra pressure of more than $6\,\mathrm{tons/m^2}$. Taking the maximum observed 10-m instantaneous (10-min average) wind speed ($43.8\,\mathrm{m\,s^{-1}}$) and the maximum observed 10-m wind gust ($64.7\,\mathrm{m\,s^{-1}}$), to see how much extra pressure they could apply to a wall. Using the same values as the example above for $\bar{\rho}$, p_1 and U_2, the extra pressure exposed to a vertical wall caused by the maximum mean wind and the maximum wind gust could have been, respectively;

$$\frac{1.18}{2}43.8^2\mathrm{kg\,m^{-1}\,s^{-2}} + 970\,\mathrm{hPa} = 2102\,\mathrm{hPa}, \tag{4.3}$$

$$\frac{1.18}{2}64.7^2\mathrm{kg\,m^{-1}\,s^{-2}} + 970\,\mathrm{hPa} = 3440\,\mathrm{hPa}, \tag{4.4}$$

This mean that the maximum mean wind speed could provide an extra pressure at the wall corresponding to the weight of more than $11\,\mathrm{tons/m^2}$, while the maximum wind gust could expose the wall of the extra pressure equivalent to the weight of more than $25\,\mathrm{tons/m^2}$.

This is of course an overestimate of the reality, because a full stagnation of the flow is unlikely. The flow will always try to find its way around the building. On the other hand, a balcony can prevent the flow from going around the building, and it would experience higher pressure compared to if the flow could just pass the building without any large disturbances. A situation that is not too far from this idealistic example is a flow that flows into an open garage; there is no way out, except the way the flow came in, and the pressure inside the garage would be extremely high. Another issue, is the low pressure perturbation on the lee side of a roof top, see Figure 4.7. Due to the separation of the boundary layer, the low pressure perturbation arises and creates an extremely high pressure gradient force. It is this large pressure gradient force, pointing from the roof towards the low, that can cause the roof to torn off the house (red arrows in Figure 4.7).

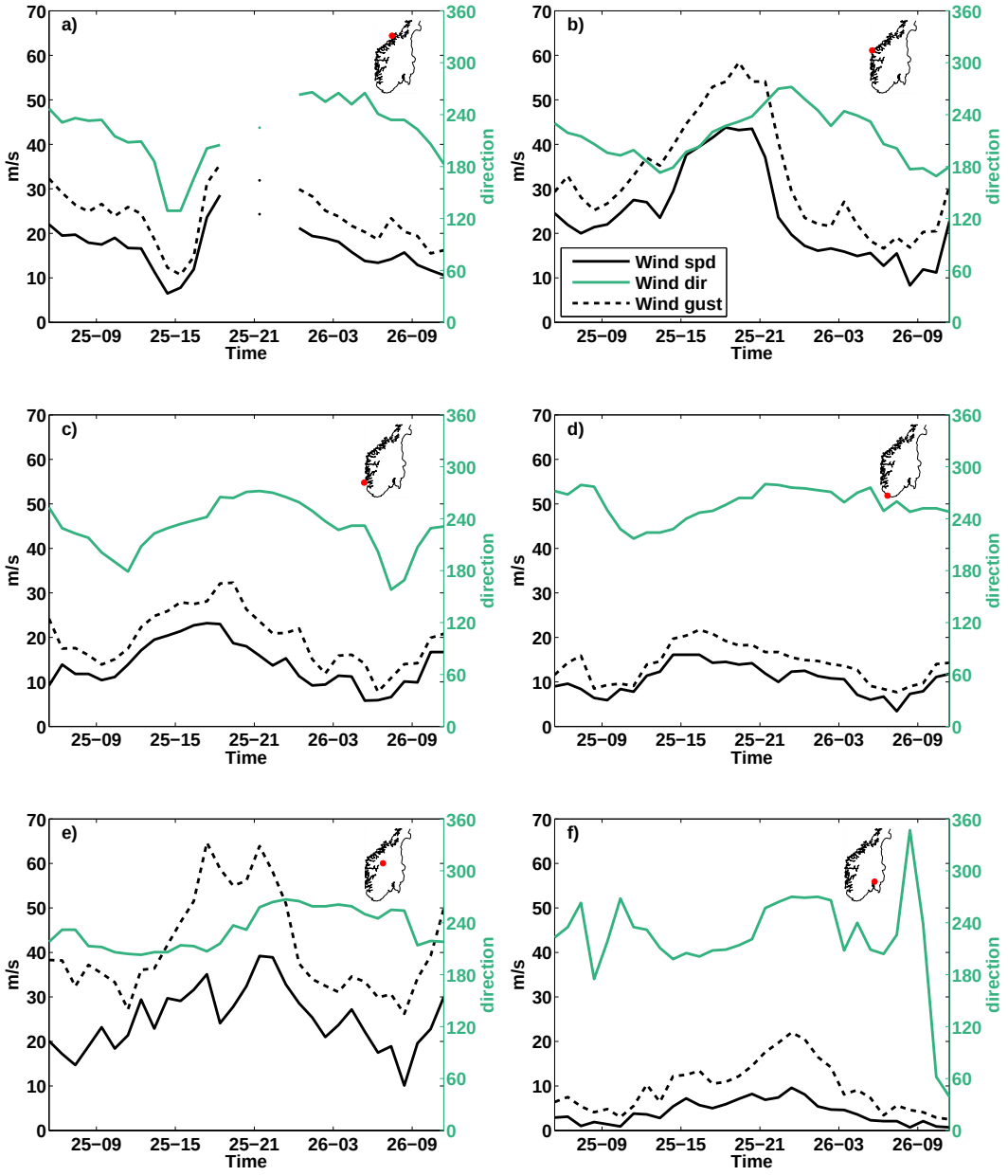

Figure 4.6: Wind measurements from six selected stations. Timeseries show the instantaneous 10-m wind speed (10-min average) in $\mathrm{m\,s^{-1}}$ (solid black curve), the strongest 10-m wind gust during the previous hour in $\mathrm{m\,s^{-1}}$ (dashed black curve), and the wind direction of the 10-m wind in degrees (10-min average) (solid green curve), for the six selected stations; a) Veiholmen, b) Kråkenes lighthouse, c) Utsira lighthouse, d) Lista lighthouse, e) Juvvasshø and f) Oslo-Blindern. The location of each station is shown in its respective figure. Labels on the x-axis represents time, where '25-00' corresponds to 25th of December at 0000UTC.

4.4 Summary

- Dagmar struck Southern Norway on the 25th of December 2011. There were several low pressure systems in the North Atlantic at that time that could have affected the strength of Dagmar, making the system develop rapidly and

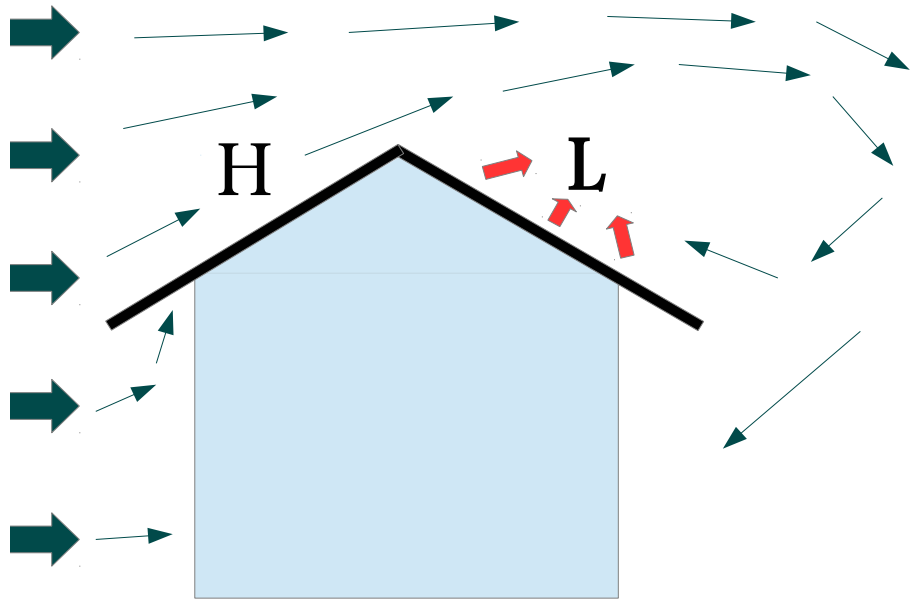

Figure 4.7: Sketch of the pressure perturbations caused by the interaction between a flow and a rooftop. "H" indicates a positive pressure perturbation, while "L" indicates a negative pressure perturbation.

become stronger.

- The highest observed 10-m mean wind speed (10-min average) was measured at Kråkenes lighthouse, $43.8\,\mathrm{m\,s^{-1}}$, while the strongest wind gust was measured at Juvvasshø, $64.7\,\mathrm{m\,s^{-1}}$. It should be noted that at several stations the instrument stopped working during the most extreme wind.

- According to Schultz and Sienkiewicz (2013), "descent associated with the frontolysis reaching a near-neutral boundary layer provides a physical mechanism for sting jets". The offshore stability at the time when Dagmar struck Norway was near-neutral and the conditions were favourable for creating a sting jet. The high-momentum air situated higher up in the atmosphere was then able to penetrate through the atmosphere, all the way down to the surface, and create very high surface winds.

- All of the six selected stations; Veiholmen lighthouse, Kråkenes lighthouse, Utsira lighthouse, Lista lighthouse, Juvvasshø and Oslo-Blindern, experienced a rapid increase of the wind when the wind direction turned from a southwesterly wind direction into a more westerly wind. This may be due to the sting jet, developed to the south of the low, where the wind direction was approximately westerly.

- Assuming a complete blocking of the flow, the additional pressure on a vertical wall, caused by the maximum mean wind ($43.8\,\mathrm{m\,s^{-1}}$) and maximum wind gust ($64.7\,\mathrm{m\,s^{-1}}$) of Dagmar, was $11\,\mathrm{tons/m^2}$ and $25\,\mathrm{tons/m^2}$, respectively.

Chapter 5

Verification Results

Before the WRF model was set to simulate how the topography in Southern Norway influenced the winds from Dagmar, the model had to be evaluated to see if it was able to produce plausible results. See Chapter 3 for information about the model setup. The results produced by the WRF model will be compared to the obervations. A linear wave model will also be used to describe the differences between the WRF model output and the observed data.

5.1 Verification of the WRF Model

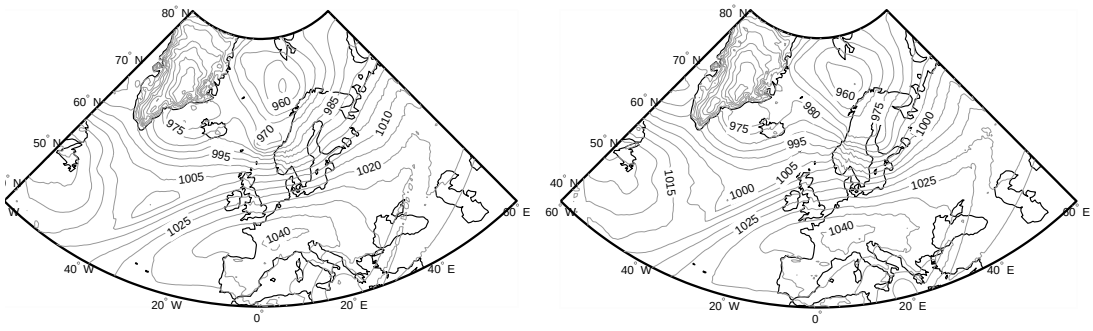

Figure 5.1: The simulated mean sea level pressure (mslp) from the WRF model for the 25th of December 2011 at 1800UTC (left panel) and for the 26th at 0000UTC (right panel).

To see whether the model captured the strength and the position of the low pressure center, the large-scale pressure pattern was plotted. Figure 5.1 shows the mean sea level pressure (mslp) produced by the model. The left panel shows the simulated mslp for the 25th at 1800UTC, while the right panel shows the 26th at 0000UTC. In the left panel Dagmar was located west of Trøndelag. This is in agreement with the analysis made by the Norwegian Meteorological Institute, left panel of Figure 4.1. During these six hours the system moved eastwards; here, positioned on the border between Nordland and Sweden. This is also in agreement with the analysis, right panel of Figure 4.1. At both times (1800UTC and 0000UTC), the large scale wind

direction was westerly offshore, turning southwesterly at the coast, to northwesterly inland over Southern Norway (see Figure 5.1). For Dagmar, the modeled low pressure center had a value of < 970 hPa at 1800UTC the 25th and < 975 hPa at 0000UTC the 26th. In the analysis, the low pressure minimum was < 960 hPa and < 965 hPa for respectively 1800UTC the 25th and 0000UTC the 26th. The model underestimated the strength of Dagmar by approximately 10 hPa. North of Dagmar, the storm Cato was rather stationary during this period, and was located to the northwest of Troms, both in the model and in the analysis. The low pressure minimum of Cato was higher in the WRF model, around 5 hPa for both 1800UTC the 25th and 0000UTC the 26th.

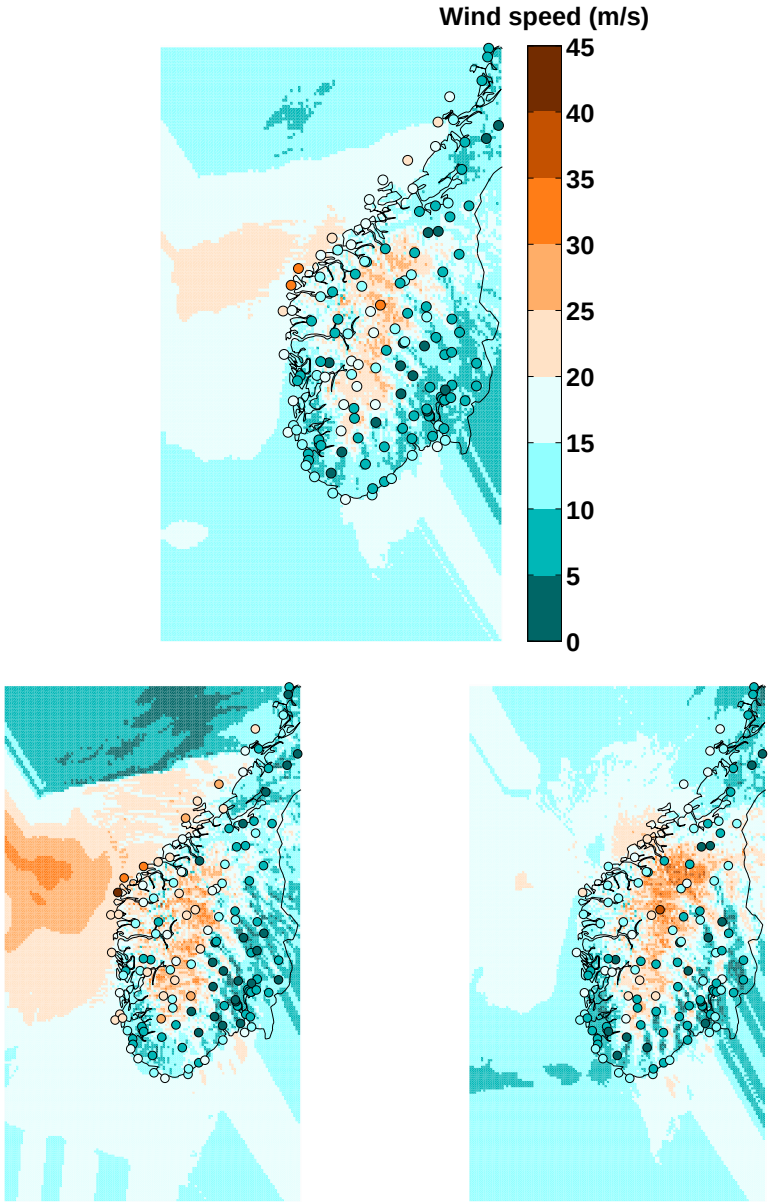

Figure 5.2: Observed (circles) and WRF modeled (background color) wind speed in $\mathrm{m\,s^{-1}}$. The upper panel shows the mean wind speed from 1500UTC the 25th of December 2011 to 0300UTC the 26th. The lower left panel represents the instantaneous 10 m wind (10 min average) for the 25th at 1900UTC, while the right panel shows the wind for the 25th at 2300UTC.

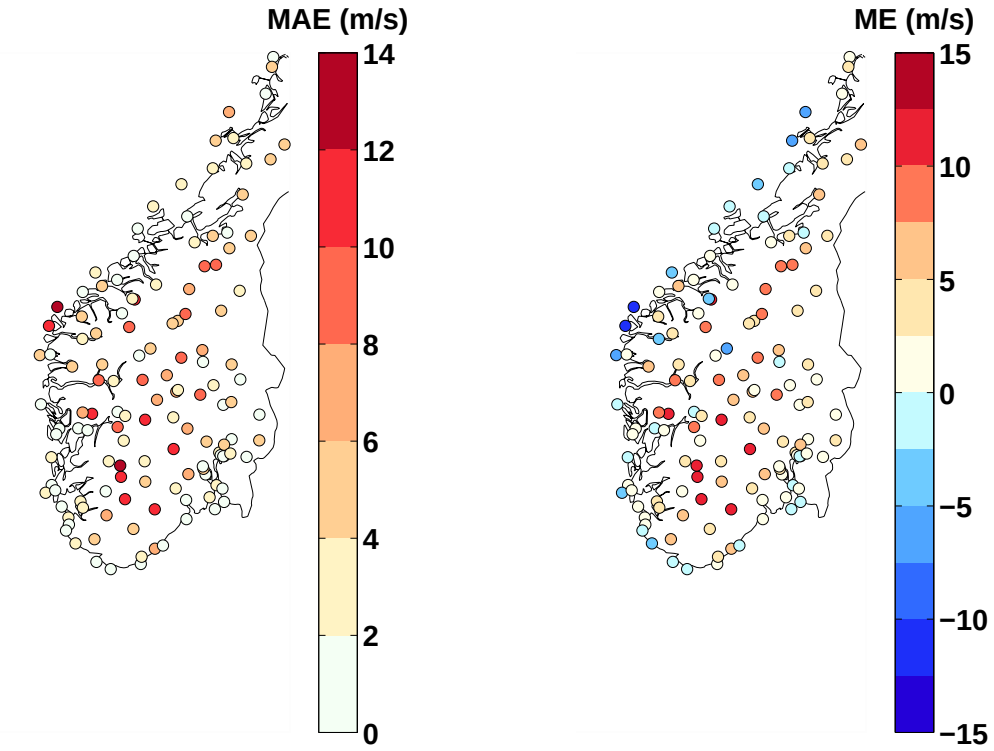

Figure 5.3: Mean difference between the hourly modeled wind speed from WRF and the hourly observed wind speed (from 1500UTC the 25th of December 2011 to 0300UTC the 26th). The left panel shows the mean absolute error (MAE), where the red color indicates where the modeled wind speed deviated from the observed wind speed. The right panel shows the mean error (ME), where the blue colors indicate where the observed wind speed was higher than the modeled wind speed, and red colors indicate where the model was higher than the observations.

The upper panel in Figure 5.2 shows the 10-m mean wind speed pattern averaged from the 25th at 1500UTC until the 26th at 0300UTC. The two lower panels show the 10-m instantaneous wind patterns when the two strongest observed wind events occurred in the observations: the costal maximum at 1900UTC the 25th (left panel) and the maximum in the mountain at 2300UTC the 25th (right panel). Comparing the WRF model result with the observed data, in the upper panel of Figure 5.2, it looks like the model on average overestimated the wind speed in Langfjella. It should be noted that many of the observational stations are located in valleys, and may not be representative for the wind speed in Langfjella. Along the coast, it looks like the model, on average, slightly underestimated the wind speed, especially around the westernmost stations; the observed wind speed was very high compared to the modeled wind speed. A reason may be that the region of very high winds offshore did not reach the costal stations because of too strong atmospheric stability in the WRF model, creating a too strong high pressure anomaly on the wind ward side of the mountain, resulting in a retarded flow. However, if the offshore jet from the WRF output reached the coast, the wind speed had probably been weaker than the observed wind at the westernmost stations; the underestimation of the pressure

minimum of Dagmar by the WRF model resulted in a weaker geostrophic wind. Another reason may be that the atmospheric stability in the WRF model was too weak compared to the observations; the flow could easier pass the mountain, and less flow was accelerated along the northwestern coast of Southern Norway. The overestimation of the wind speed in the mountain support the last explanation. The model also predicted strong wind events on the lee side of Langfjella, verified by the streaks of the lighter colors. This was also present in the observations. A third reason for the deviation of the WRF wind speed from the observations may be wrong representation of the vegetation cover over Southern Norway; too high friction in the model along the coast could result in a more enhanced upstream wind shadow, and too low friction in the mountains could result in an overestimation of the wind speed.

Figure 5.3 shows the difference between the model output and the observed data. In the right panel the mean error (ME) is shown. The ME tells whether the model, on average, over- or underestimated the observed wind speed in the corresponding point. In the left panel, the mean absolute error (MAE) is shown. The MAE is the mean absolute difference between the hourly model output and hourly observed data, at each observational station. The MAE tells nothing about which of the two (observastions or WRF output) that had the highest wind speed, only if the modeled wind speed deviated from the observed wind speed. During this 12-hour period, it looks like the model underestimated the wind speed along the coast, especially along the northwest coast, and overestimated in the mountain area and further inland.

Numeric differences between the WRF model output and the observations are given in Table 5.1. The results were divided into three regions; costal stations, mountain stations (stations located above 1000 m.a.s.l) and inland stations, with six selected stations in each region. The location of the different stations can be seen in Figure 5.4. Some of the stations were highly over or underestimated by the WRF model, so the median was taken into account to exclude the outliers in the estimation of the average wind speed.

From this table it is evident that the WRF model underestimated the average wind speed along the coast, for the six selected stations. The model underestimated the average wind speed along the coast by $1.39\,\mathrm{m\,s^{-1}}$. On the other hand, the median shows no underestimation. This implies that, for these six selected stations, the WRF model did a good job simulating the wind speed along the coast, but at certain stations the underestimation of the wind speed was very pronounced. The average maximum wind speed along the coast was underestimated by the WRF model, $2.4\,\mathrm{m\,s^{-1}}$ (mean) and $0.44\,\mathrm{m\,s^{-1}}$ (median). In the moutain area, the WRF model overestimated the average wind speed by $3.16\,\mathrm{m\,s^{-1}}$ (mean) and $2.40\,\mathrm{m\,s^{-1}}$ (median), and the maximum wind speed by $2.15\,\mathrm{m\,s^{-1}}$ (mean) and $0.09\,\mathrm{m\,s^{-1}}$ (median). The overestimation of the average wind speed, for the six selected stations, was largest for the inland stations. In the lee of Langfjella the WRF model overestimated the average wind speed by $3.43\,\mathrm{m\,s^{-1}}$ for both mean and median. The average maximum wind speed was overestimated by as much as $7.25\,\mathrm{m\,s^{-1}}$ (mean) and $5.71\,\mathrm{m\,s^{-1}}$ (me-

dian). It should be mentioned that the differences between the WRF model and the observations were largest where the most extreme wind events were observed, e.g., at Kråkenes lighthouse and Svinøy lighthouse.

The underestimation of the wind speed by WRF was very pronounced for the westernmost stations (e.g. at Kråkenes lighthouse and Svinøy lighthouse). The reason was probably the wind shadow that occurred along the western coast, as a consequence of the flow being retarded by the presence of Langfjella. If the high pressure region on the windward side (that slowed down the wind) was less pronounced, the area of very strong wind (the orange bulb offshore the northwest coast) may have reached the westernmost stations. A WRF simulation of Dagmar performed by Harstveit (2012) also resulted in underestimation of the wind speed for the westernmost stations.

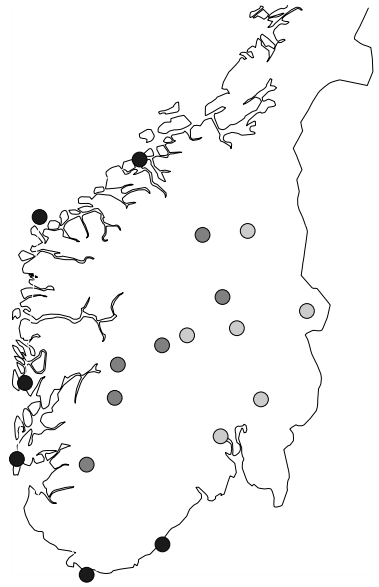

Figure 5.4: Location of the stations listed in Table 5.1. The black dots correspond to the "costal stations", while the dark and light grey dots correspond to the "mountain stations" and the "inland stations", respectively.

	Mean Wind Speed			Max Wind Speed		
Station	**mod**	**obs**	**diff**	**mod**	**obs**	**diff**
Costal stations:						
Torungen fyr	14.61	14.85	-0.24	18.32	18.00	0.32
Lindesnes	15.33	16.42	-1.09	17.11	18.30	-1.20
Haugesund flyplass	13.36	12.88	0.48	18.56	21.30	-2.74
Bergen flyplass	10.71	9.80	0.91	14.28	13.40	0.88
Svinøy fyr	22.90	31.95	-9.05	26.38	38.70	-12.32
Kristiansund	16.33	15.69	0.64	24.20	23.50	0.70
Mean:	15.54	16.93	**-1.39**	19.81	22.2	**-2.4**
Median:	14.97	15.27	**0.12**	18.44	19.80	**-0.44**
Mountain stations (> 1000 masl):						
Hemsedal	15.77	9.60	6.61	21.00	20.60	0.40
Finse	21.12	18.35	2.78	26.02	26.50	-0.48
Kvitfjell	11.88	13.81	-1.93	23.76	24.20	-0.44
Sandhaug	20.71	18.79	2.02	23.30	25.50	-0.22
Blåsjø	19.61	18.74	0.87	27.04	25.30	1.74
Hjerkinn	19.61	11.03	8.58	31.58	17.70	13.88
Mean:	18.12	14.96	**3.16**	25.45	23.30	**2.15**
Median:	19.61	16.08	**2.40**	24.89	24.75	**0.09**
Inland stations:						
Drammen	5.72	5.61	0.12	11.53	8.80	2.73
Lillehammer	7.61	5.55	2.66	14.65	8.60	6.05
Fagernes	10.33	3.22	7.10	19.02	5.20	13.72
Tynset	12.36	8.15	4.20	18.77	13.40	5.37
Gardermoen	10.95	9.90	1.05	22.64	18.80	3.84
Trysil	10.55	4.52	6.04	19.51	7.70	11.81
Mean:	9.59	6.16	**3.43**	17.69	10.43	**7.25**
Median:	10.44	5.58	**3.43**	18.90	8.70	**5.71**

Table 5.1: Overview of the differences between the WRF model and the observations, for the mean wind speed and the maximum wind speed for three regions; costal stations, mountain stations and inland stations. All the values in this table are given in $\mathrm{m\,s^{-1}}$. The mountain stations were located above 1000 meters above sea level (masl) (see Appendix A for more station information). "Mean Wind Speed" corresponds to data that were average from 1500UTC the 25th of December 2011 until 0300UTC the 26th, "Max Wind Speed" shows the maximum wind speed that occurred in the same time interval, "mod" corresponds to the WRF model results, "obs" is the observed wind speed, "diff" is the difference between the WRF moded and the observed data (mod - obs).

Figure 5.5 shows timeseries of the 10-m wind speed from 0600UTC the 25th until 1200UTC the 26th for both the WRF model output and the observations for the selected stations; a) Veiholmen, b) Kråkenes lighthouse, c) Utsira lighthouse, d) Lista lighthouse, e) Juvvasshø and f) Oslo-Blindern (see Chapter 4, Figure 4.6 for the location of the six chosen stations). The figure also include results from 11-h smoothed data. This was done to see if the model captured the wind situation on a time-scale longer than one hour.

As mentioned in Chapter 4, the wind instrument at Veiholmen (Figure 5.5a) broke down during the strongest wind. The WRF model underestimated the wind speed at Veiholmen during the period of the strongest observed wind. The model predicted three wind maximum, where the first occurred before the observed maximum, all three lower than the observed wind speed. At the coastal site, Kråkenes lighthouse (Figure 5.5b), the model underestimated the wind speed throughout the whole period (from 0600UTC the 25th until 1200UTC the 26th). During the time interval when the strongest observed winds occurred, the WRF model predicted a wind speed almost $20\,\mathrm{m\,s^{-1}}$ too low. In the 11-h smoothed data the result were better, but still the model output was too low, indicating that the underestimation was persistent. The same things are visible in the result for Utsira lighthouse, Figure 5.5c. The observed wind speed was higher than the model wind almost throughout the entire period. For Lista lighthouse, d), the model curve and observed curve are in better agreement. During the strongest observed wind (around 1500UTC the 25th) the model predicted correct maximum wind speed, but two hours too late. In the 11 h smoothed data the two curves coincide almost completely during the period of strongest wind. At the mountain site Juvvasshø, e), the model also underestimated the wind speed at almost every hour. As mentioned earlier, the model usually overestimated the wind speed in the mountain area, but this station is one of the exceptions. Again the model captured the increase of wind speed at the right time, but the increase was 5-10 $\mathrm{m\,s^{-1}}$ too small. In the smoothed curve the modeled wind speed was also too low. The situation is different in the last panel, showing the wind speed for Oslo-Blindern; the WRF modeled wind speed was too high at almost every hour. During the strongest wind event (around 0000UTC the 26th) the model overestimated the wind by around $5\,\mathrm{m\,s^{-1}}$.

The observed and the WRF model wind direction can be seen in Figure 5.6. Here, the different panels, a) - f), correspond to the same stations as in Figure 5.5. The wind direction for all the costal stations (panel a) - d)) from the model was very similar to the observations, this was also the case for the mountain station, Juvvasshø. For the northernmost stations (a, b and e), it looks like the model in general had a more westerly wind direction than in the observations. This is in agreement with the theory that the stability could have been too low in model run compared to the observations, and that more of the flow in the the model therefore went straight over the mountain and without attaining a northerly component. For Oslo-Blindern, f), the observed wind direction varied more than at the other stations. The model

captured the clockwise turning of the wind when the wind increased (starting around 2100UTC the 25th), but it did not capture the turning of the wind to a more northerly direction around 0900UTC at the 26th. This was also at the time when the lowest wind at this station was observed, which the model overestimated.

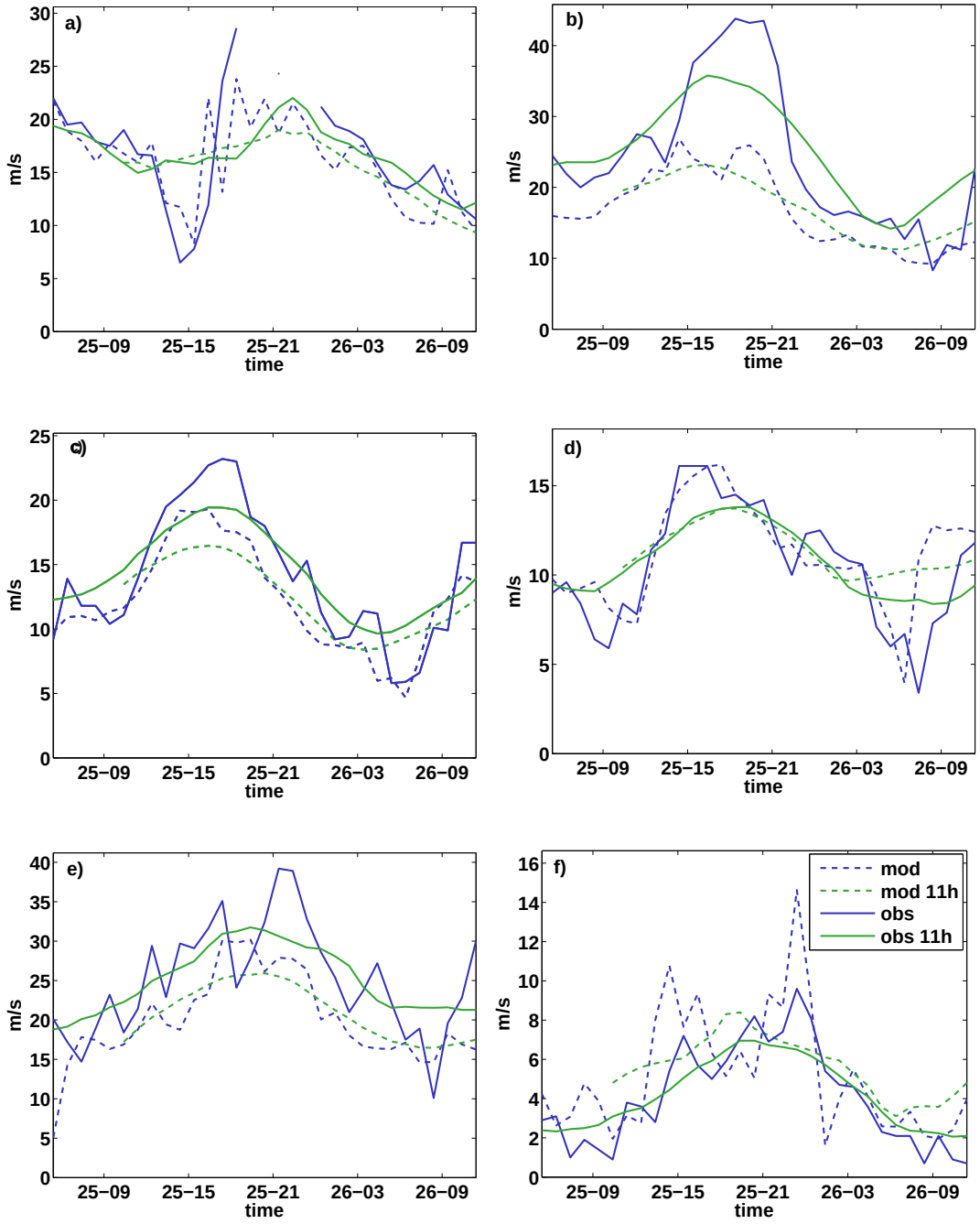

Figure 5.5: Timeseries of the 10-m wind speed from the 25th of December 2011 at 0600UTC until the 26th at 1200UTC. The solid lines correspond to the result from the observations, while the dashed lines correspond to the result from the WRF model. The blue color shows the hourly data, while the green color indicates result from 11-h smoothed data. Stations shown are: a) Veiholmen, b) Kråkenes lighthouse, c) Utsira lighthouse, d) Lista lighthouse, e) Juvvasshø and f) Oslo-Blindern.

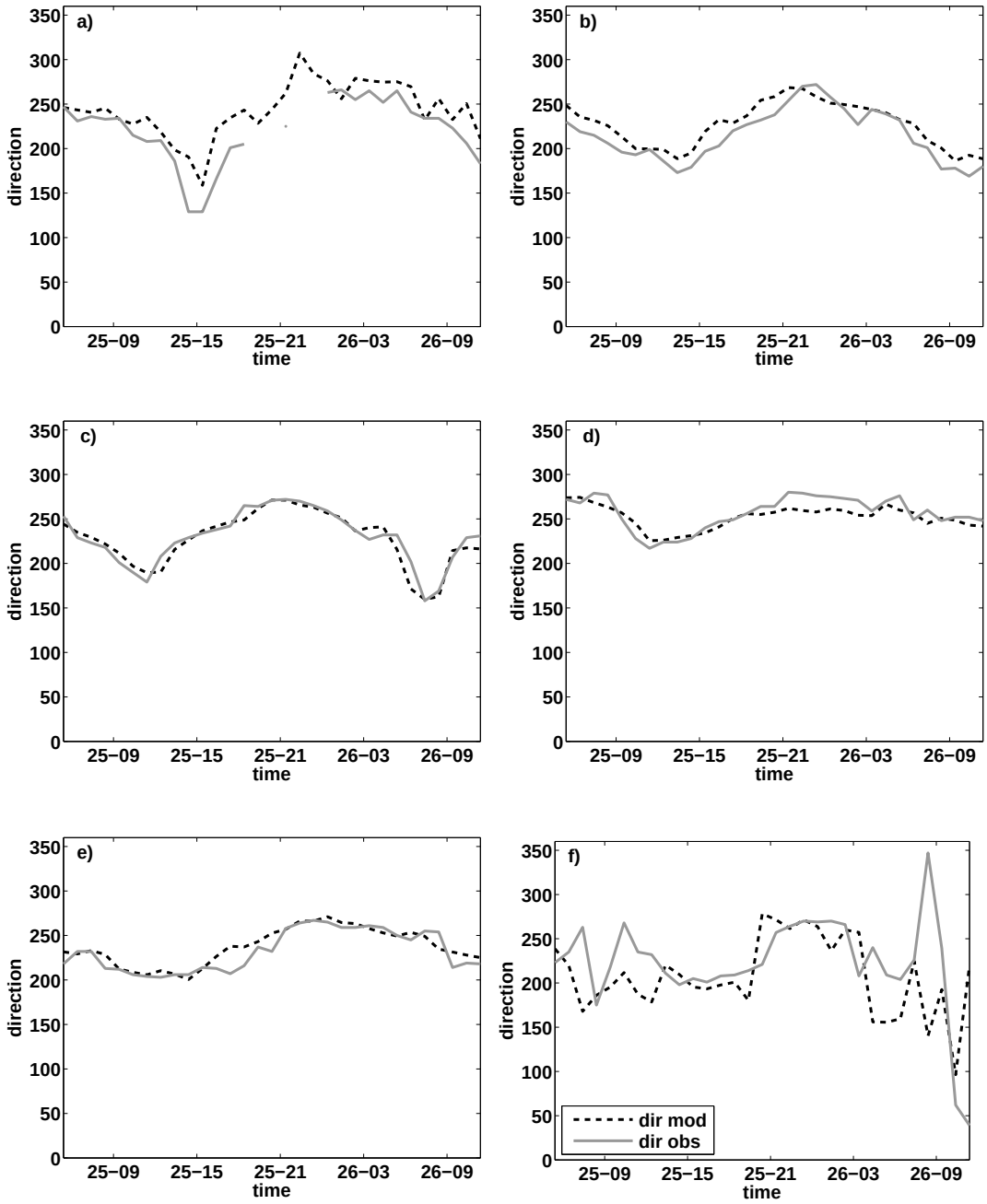

Figure 5.6: Timeseries of the 10-m wind direction from the 25th of December 2011 at 0600UTC until the 26th at 1200UTC. The solid grey line is the observed wind direction, and the dashed black line is the 10-m wind direction from the WRF model. Stations shown are: a) Veiholmen, b) Kråkenes lighthouse, c) Utsira lighthouse, d) Lista lighthouse, e) Juvvasshø and f) Oslo-Blindern.

5.2 Results from Linear Theory

How much of the observed signals, from the observations and WRF model output, that can be described by linear theory were investigated using a simple linear wave model. This was done to get a better understanding of how a uniform flow interacts with an idealized Gaussian shaped mountain, and to see the arising flow patterns (see Section 3.2 for information about the model and the setup).

To be able to compare the results from the linear model with the observations and the WRF output, the setup of the linear wave model was tuned against the observed values in the key variables (wind speed and direction, atmospheric stability, and the height and shape of the moutain). This means that the background wind speed was set to $32\,\mathrm{m\,s^{-1}}$, and the upstream wind direction was westerly. The atmospheric stability was near-neutral; the potential temperature increased by approximately $1.5°$ Kelvin per 1000 m, meaning that the bouyancy frequency was set to $N^2 = 0.00725$. The height of the idealized Gaussian mountain was 1500 m and the shape was elliptic, where the flow approached perpendicular to the major axis.

The results from this run are shown in Figure 5.7. Due to the Coriolis force, the region of weaker wind on the windward side was slightly shifted to the right when looking downstream of the flow (see upper panel of Figure 5.7). The region of high pressure perturbation, responsible for this deceleration of the flow, can be seen in the lowest right panel. As the flow approached the mountain the wind was slowed down. As a consequence, the flow attained a northerly component, and the flow to the south of the high pressure perturbation developed a component in the opposite direction of the corresponding pressure gradient, creating a retarded flow in that area. This area of weaker winds was propably the one Barstad and Grønås (2005) referred to as the "upstream minimum".

Another region of decelerated air was found about 1000 km downstream of the mountain top, referred to as the "downstream wind shadow" (Barstad and Grønås, 2005). This wind wake occurred as a consequence of a divergent flow in that area. The weakest wind was found upstream of the mountain barrier, $26\,\mathrm{m\,s^{-1}}$. This indicates a reduction in the upstream wind speed of 19 % (see upper right panel of Figure 5.7). The flow accelerated down the lee side of the mountain reaching $40\,\mathrm{m\,s^{-1}}$ approximately 50 km downstream of the top. The wind here was 25 % higher than the upstream wind speed of $32\,\mathrm{m\,s^{-1}}$. According to Bernoulli's equation (see Section 2.5 and Eq. 2.26), the negative pressure perturbation together with the descent of the air on the lee side, forces the wind velocity to increase to compensate for the negative pressure and air motion. The region of slightly positive pressure perturbation downstream of the mountain was propably caused by a minor convergence of the air, visible in the wind direction field (lower left panel in Figure 5.7). The Rossby number (Ro) was a bit larger than unity ($Ro = 1.27$), indicating that the flow was moderately affected by rotation. The non-dimensional mountain height (h) was 0.34, indicating a flow that was characterized by gravity wave formation.

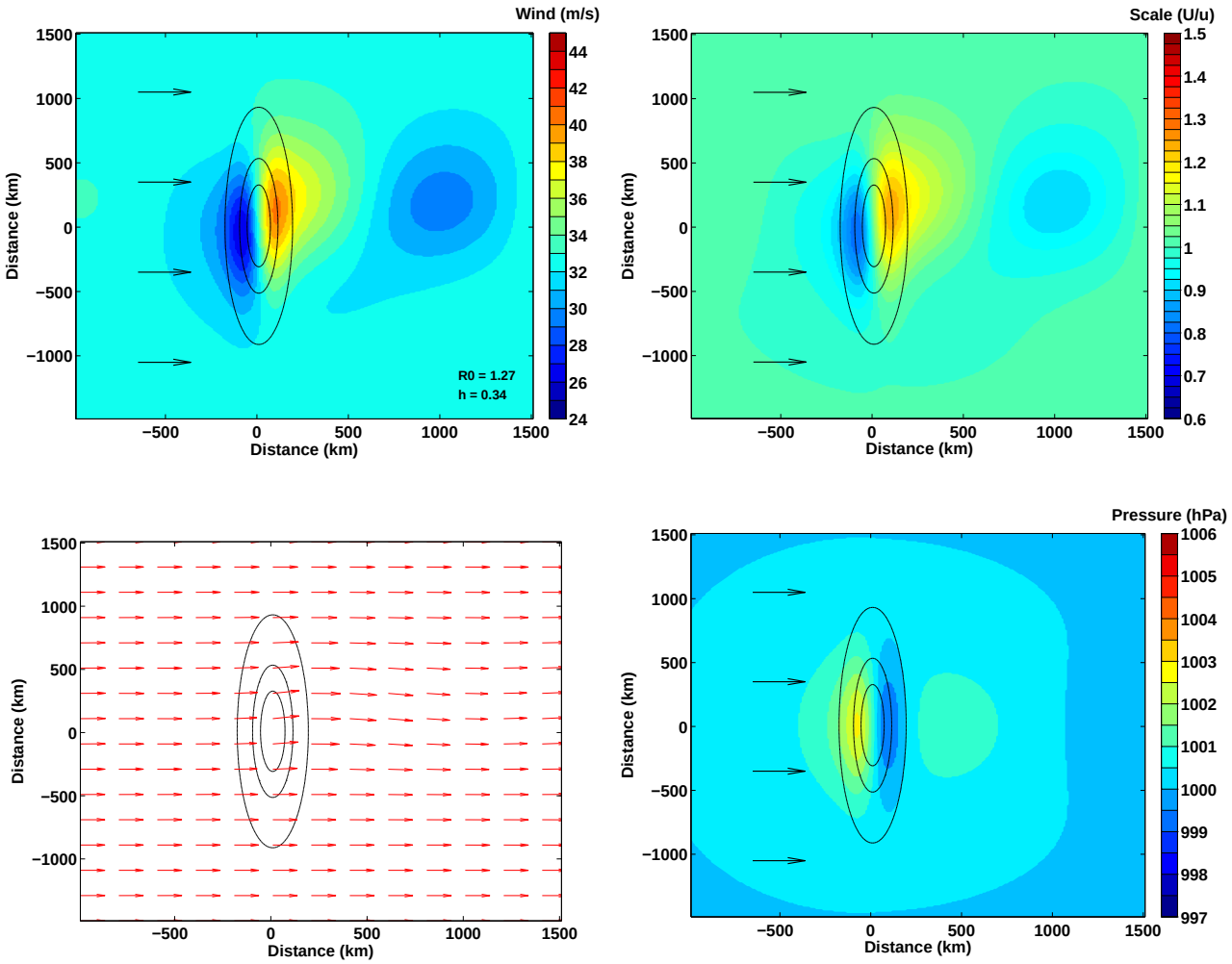

Figure 5.7: Results from the realistic run by the linear wave model. The upper left panel shows the wind speed in colors together with the upstream wind direction (arrows). The Rossby number (Ro) and the non-dimentional height (h) are also shown in this panel. The upper right panel shows the local wind speed (U) scaled by the background wind speed (u). The lower left panel shows the local wind speed and direction, where the arrows mark the direction from its respective point. The lower right panel shows the pressure distribution, where the background pressure was set to 1000 hPa. The mountain height was 1500 m, $N^2 = 0.00725$, and the background wind was a $32\,\mathrm{m\,s^{-1}}$ westerly wind. The solid black ellipses indicate the height contours of the mountain, where the outer ellipse corresponds to 50 m, the one in the middle is at 500 m and the innermost ellipse corresponds to 1000 m.

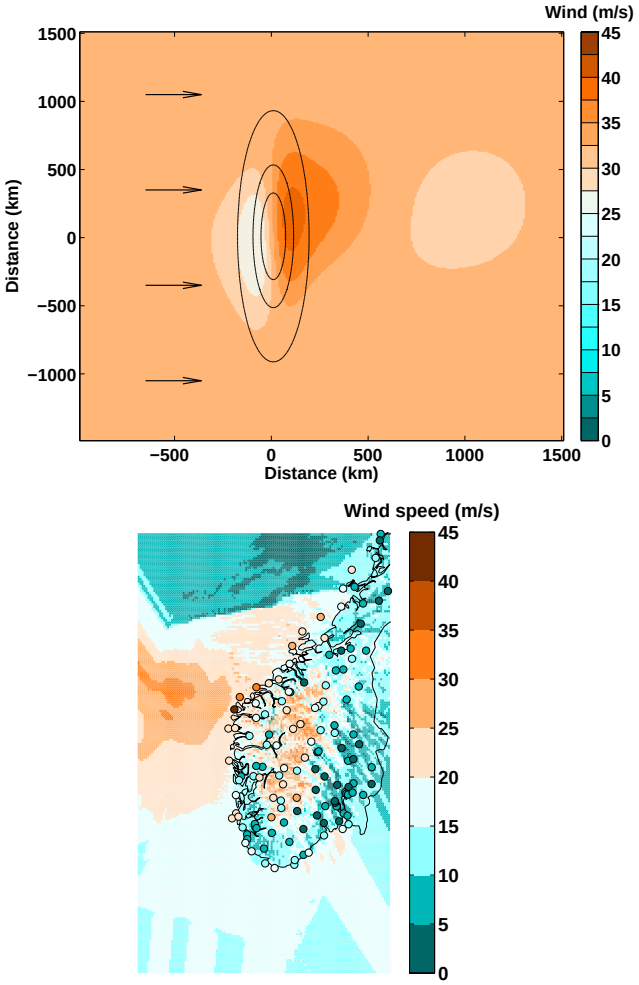

Figure 5.8: The upper panel shows the wind speed pattern from the realistic run (Run1) carried out by the linear wave model. The lower panel shows the wind pattern from the WRF control run for 1900UTC the 25th of December 2011 (background colors) together with the observations (colored dots).

5.2.1 Comparison with WRF Output and Observations

How much the result from the WRF model and the observations that can be described by linear theory is yet to be discussed. Although many of the parameters were left out of the linear wave model, like friction, vertical and horizontal wind shear, non-hydrostacy and the complexity of the real topography, the results are to some extent comparable. As mentioned in Section 2.3, linear theory is said to be trustworthy when the non-domensional mountain height ($\hat{h}$) is much less than one, and in the realistic run $\hat{h} = 0.34$. In Figure 5.8 the resulting wind speed from the realistic run carried out by the linear wave model (upper panel) is shown, together with the wind pattern from the WRF control run and the observations (lower panel).

By comparing the result from the realistic run (linear model) with both the results from the WRF control run and the observations, the most pronounced similarity was the upstream wind shadow. Also, a wind shadow, or an area of weaker wind, was found on the lee side of Langfjella in the WRF control run and in the observations, but this was propably not the downstream wind shadow that occurred in the realistic run. According to the location of the downstream wind shadow in the realistic run (see upper panel os Figure 5.8), located 1000 km from the obstacle, the downstream

wind shadow in the WRF output and in the observations would have been located in Finland. The downstream wind shadow present in the WRF output and in the observations was probably caused by surface friction (the large roughness length), and presence of valleys and topography on smaller scales. The acceleration of the flow down the lee side, evident in the realistic run, was not present in the WRF control run or in the observations. The highest wind speed in the WRF control run was found in the highest part of Langfjella, while the highest wind speed in the observations was found at the northwest coast of Southern Norway, and not on the way down the lee side of the mountain, as in the realistic run. The lack of acceleration down the lee side in the WRF model and in the observations might be caused by the higer surface roughness or a different atmospheric stability. The strong winds offshore the northwestern coast of Southern Norway, present in the WRF control run and in the observations, was not present in the realistic run. The reason may be that the realistic run did not have the "corner" located at Stad, which can create tip jets. Also, small changes in the upstream wind direction can be crucial of the strength and even the existence of the "left side jet" (Barstad and Grønås, 2005). The latter is investigated in Section 5.2.2.

5.2.2 The Sensitivity Runs

The sensitivity of the WRF model results to changes in wind speed, direction, mountain height and atmospheric stability can be investigated by performing sensitivity runs with the linear model. This may improve the understanding of why the output from the WRF model deviated from the observations. In addition to the realistic run (Run1) described above, four sensitivity runs for the linear model were carried out; A run where the wind direction was slightly changed (Run2), a run where the wind speed was decreased (Run3), a run where the mountain height was increased (Run4), and in the last run the atmospheric stability was increased (Run5). In all the runs only one parameter was changed, while the other parameters were the same as in the realistic run (Run1).

Southwesterly Wind Direction (Run2)

The first sensitivity run (Run2) was conducted to see how sensitive the wind and pressure patterns were to changes in the wind direction. The wind was turned anticlockwise to a southwesterly wind direction[1] (231°), but the strength of the wind was unchanged.

The results from this scenario can be seen in Figure 5.9. The first thing to notice is that the downstream wind shadow now was enhanced, together with a less apparent upstream minimum. The Rossby number (Ro) was here 0.85, which was less than for the realistic run (Ro=1.27). That means that the rotational effect was larger for this setup, indicating more assymetric flow around the mountain. Since the flow approached the barrier from a southwesterly direction, the flow had to traverse a broader mountain, and the flow was then more affected by it. The acceleration of the flow down the lee side extended further north, and even to the upstream side of the mountain (see the two upper panels of Figure 5.9), indicating the presence of a "left side jet". The reason may be that when the upstream wind direction was southwesterly, the flow to the north of the high pressure region had a larger component in the direction of the pressure gradient force.

[1] To keep the strength of the wind equal to the wind speed from the realistic run ($32\,\mathrm{m\,s^{-1}}$), the compenents of the wind (u,v) was set to be $25\,\mathrm{m\,s^{-1}}$ and $20\,\mathrm{m\,s^{-1}}$, respectively. This resulted in a wind direction of 231°.

The acceleration of the flow down the lee side resulted in a maximum wind speed of $41\,\mathrm{m\,s^{-1}}$, corresponding to an increase of 28 %, while the downstream minimum had a wind speed of $27\,\mathrm{m\,s^{-1}}$, which is a reduction of 26 %. The negative pressure perturbation that arrised on the lee side was less pronounced than in the realistic run. The reason is that the restoring of the geostrophic balance forced more air in the area of lower pressure, making the negative pressure perturbation less pronounced in this run.

Reduced Wind Speed (Run3)

In this run (Run3), the only factor that was changed from the realistic run was the wind speed. The wind speed was set to $18\,\mathrm{m\,s^{-1}}$. Results from Run3 are shown in Figure 5.10. A striking wave pattern is seen in the horizontal wind speed downstream of the obstacle. The upstream minimum and the jet down the lee side had the same structure as in the realistic run, though a bit more pronounced. The maximum wind speed was as high as $27\,\mathrm{m\,s^{-1}}$, an increase of 50 %. Both the upstream minimum and the downstream wind shadow were very pronounced, with a reduction of around 33 %.

The downstream region of higher pressure was located closer to the mountain in this run than in the realistic run. The reason is probably that this flow converged closer to the mountain due to the lower wind speed. The Rossby number was 0.71, meaning that the rotational effect was larger than for both the realistic run and the run with southwesterly wind, due to the lower wind speed. The non-dimentional mountain height (h) was 0.6, which may indicate that the flow was between regimes; $h < 1$ and $h \approx 1$, where the first one is characterized by high drag over the mountain with strong lee winds and breaking gravity waves aloft, and the second is characterized by gravity waves (Smith, 1989).

The very distinct wave pattern in the lee of the mountain was caused by a larger convergence and divergence of the flow as a consequence of the lower wind speed (lower kinetic energy). More of the flow was forced to go around the mountain, hence the convergence and divergence in the lee were larger than in the realistic run.

Higher Mountain (Run4)

The only parameter that was changed in this run was the height of the mountain. The shape was still Gaussian and the crosswise and lenghtwise dimensions were unchanged. The height of the mountain was changed from 1500 m to 1800 m. The results from Run4 are shown in Figure 5.11. The general wind pattern from this run was very similar to the pattern from the realistic run. The upstream minimum and the downslope wind was a bit more pronounced here; $24\,\mathrm{m\,s^{-1}}$ and $41\,\mathrm{m\,s^{-1}}$ in this run, compared to $26\,\mathrm{m\,s^{-1}}$ and $40\,\mathrm{m\,s^{-1}}$ in the realistic run. The deceleration of the wind speed to $24\,\mathrm{m\,s^{-1}}$ corresponds to a decrease of 25 %, while the increase of the wind to $40\,\mathrm{m\,s^{-1}}$ equals an acceleration of 28 %. The high pressure perturbation on the upstream side of the mountain was slightly higher in this run, 1003.3 hPa against 1002.7 hPa from the realistic run. The high pressure region downstream of the mountain was in this run a bit stronger than in the realistic run. The reason for this difference in the positive pressure perturbations may be that more of the air was forced to go around the barrier (evident from the higher pressure on the windward side in this run), and hence also the convergence on the lee was stronger in this run. The Rossby number was equal to the Rossby number in the realistic run, while the non-dimensional mountain height was slightly higher ($h = 0.41$).

Increased Stability (Run5)

In the last run the atmospheric stability was the parameter that was changed. The stability was changed so that the potential temperature increased with 4 °K/1000 m instead of 1.5 °K/1000 m. The rest of the parameters were the same as in the realistic run (Run1). The results from this run are shown in Figure 5.12. Again, the main patterns were similar to the patterns from the realistic run. The difference was that the strength of the signals was more enhanced in this run; the wind shadows, the acceleration of the wind on the lee side, and also the pressure perturbations were more distinct. Due to the higher stability in this run more of the flow did not make it over the mountain and was forced around. The large positive pressure perturbation on the windward side is a good indication to splitting of the flow. The pressure on the upstream side was 1004.6 hPa, almost 2 hPa more than in the realistic run. Also the negative pressure perturbation on the lee side of the mountain was more pronounced in this run (998.7 hPa). The wind speed on the wind ward side and down the lee side was $20\,\mathrm{m\,s^{-1}}$ and $44\,\mathrm{m\,s^{-1}}$, corresponding to a deceleration of 36 % and an acceleration of 38 %, respectively. The Rossby number was the same as for the realistic run (1.27) which indicates flow that was moderately assymetric around the mountain. The non-dimensional mountain height (h) was slightly higher for this run (Run5), but still in the regime where high drag over the mountain and strong lee winds are expected, toghether with breaking gravity waves aloft.

Concluding Remarks

Four sensitivity runs were carried out by the linear wave model to get an idea of how sensitive the observed wind pattern (from observations and the WRF model) was to changes in key variables (wind speed and direction, mountain height and atmospheric stability). The results from the linear wave model showed that small changes in the upstream wind speed, wind direction, atmospheric stability and topography height can have significant effect on the resulting wind and pressure patterns. If several of the key parameters in the WRF model deviated from the observed values, this may result in very different wind patterns. From westerly to southwesterly upstream wind direction the "left side jet" varied from almost non-existing to very pronounced (evident in Run2), and it was very clear that a stronger atmospheric stability and higher mountain forced more of the flow to go around the mountain and converge on the lee side.

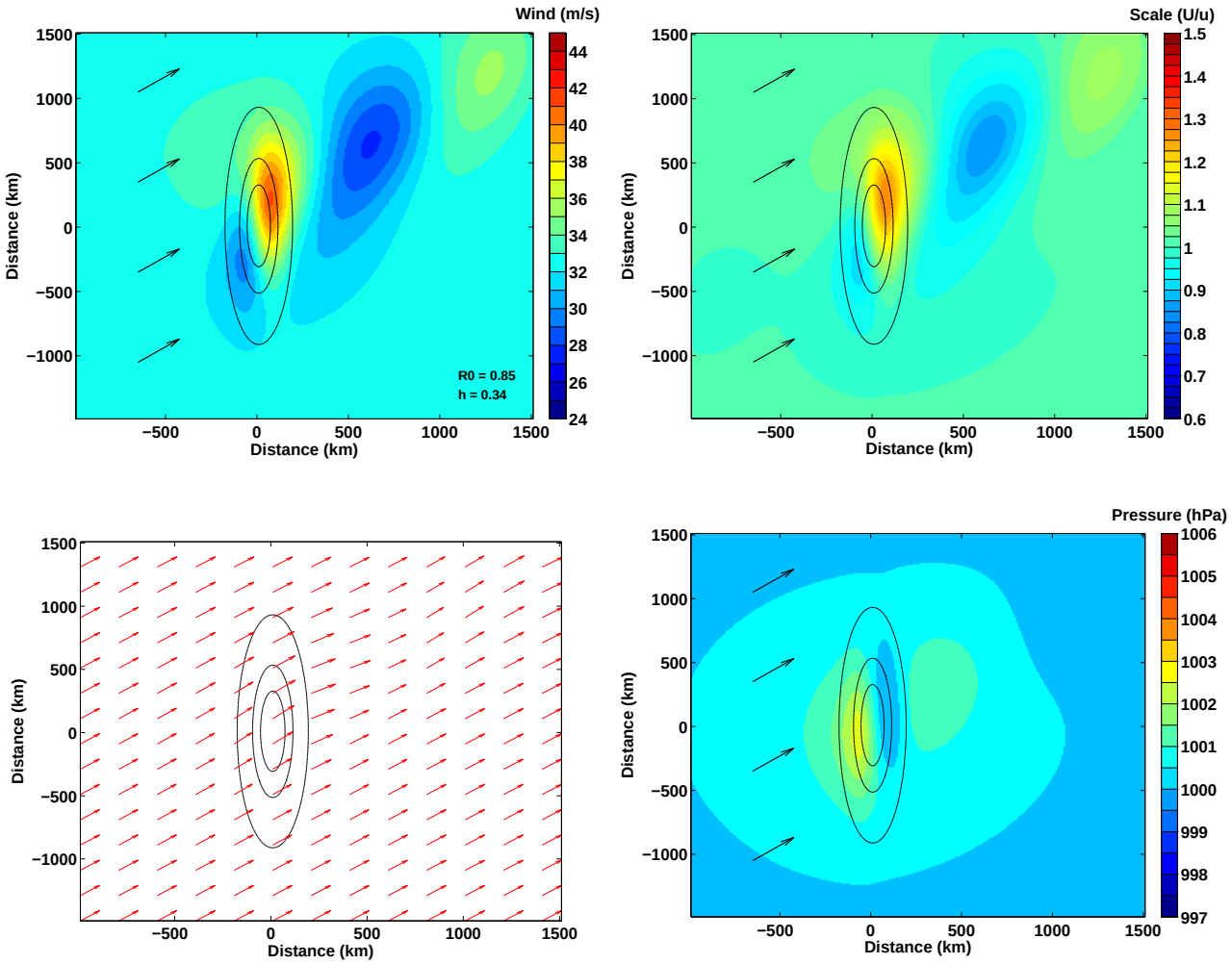

Figure 5.9: Same as in Figure 5.7, but the upstream wind direction was changed to southwesterly.

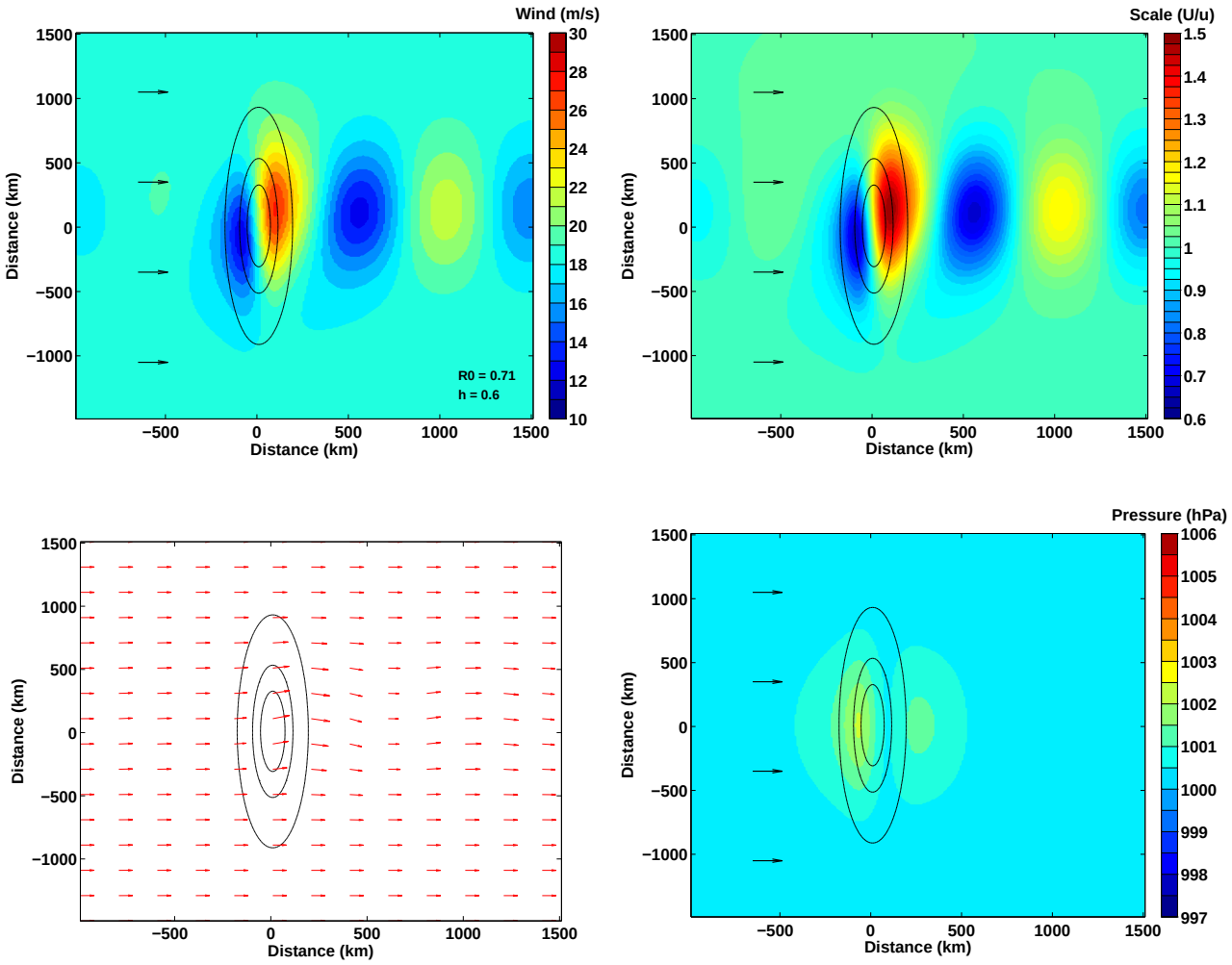

Figure 5.10: Same as in Figure 5.7, but the upstream wind speed was reduced to $18\,\mathrm{m\,s^{-1}}$.

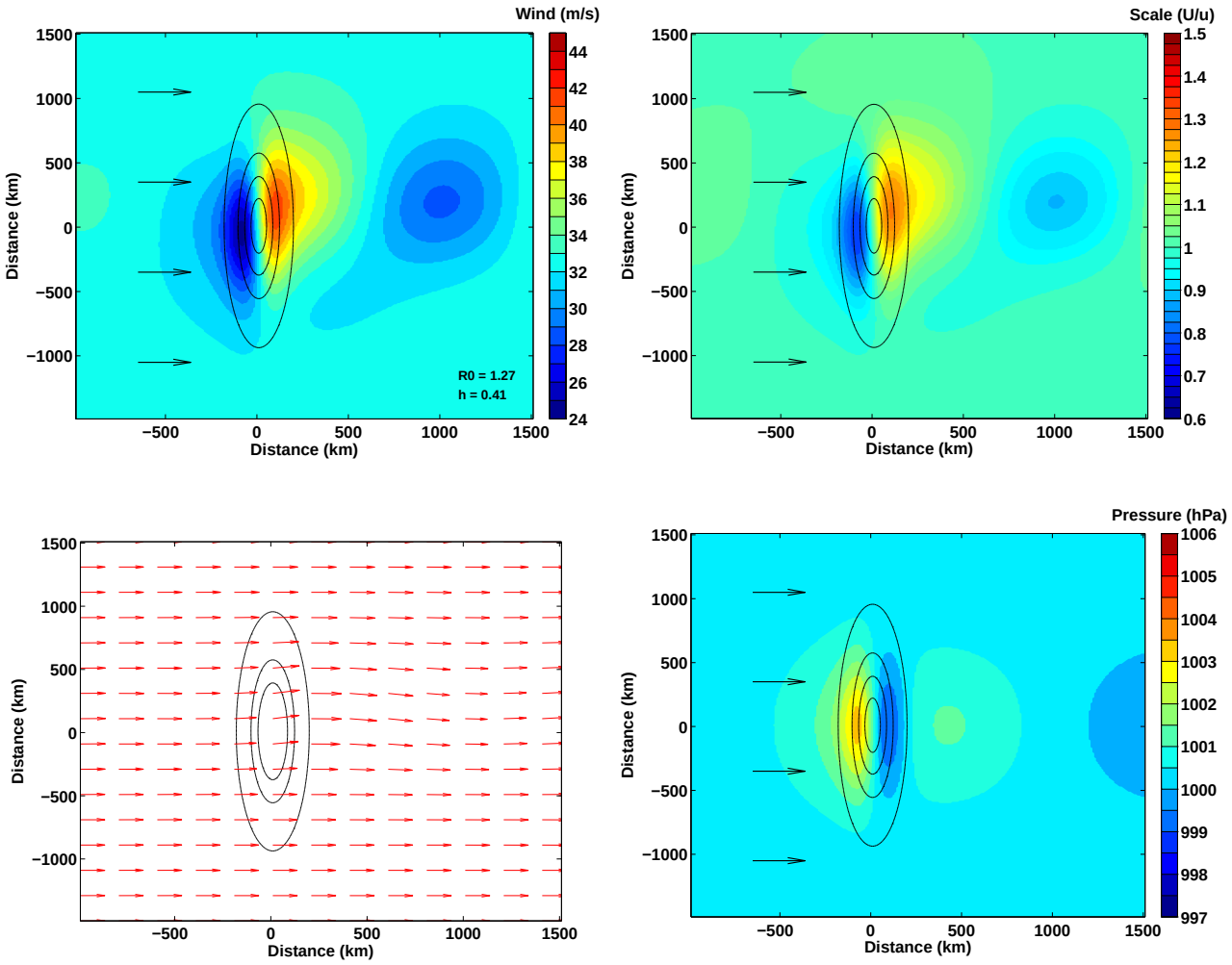

Figure 5.11: Same as in Figure 5.7, but the mountain height was increased to 1800 m.

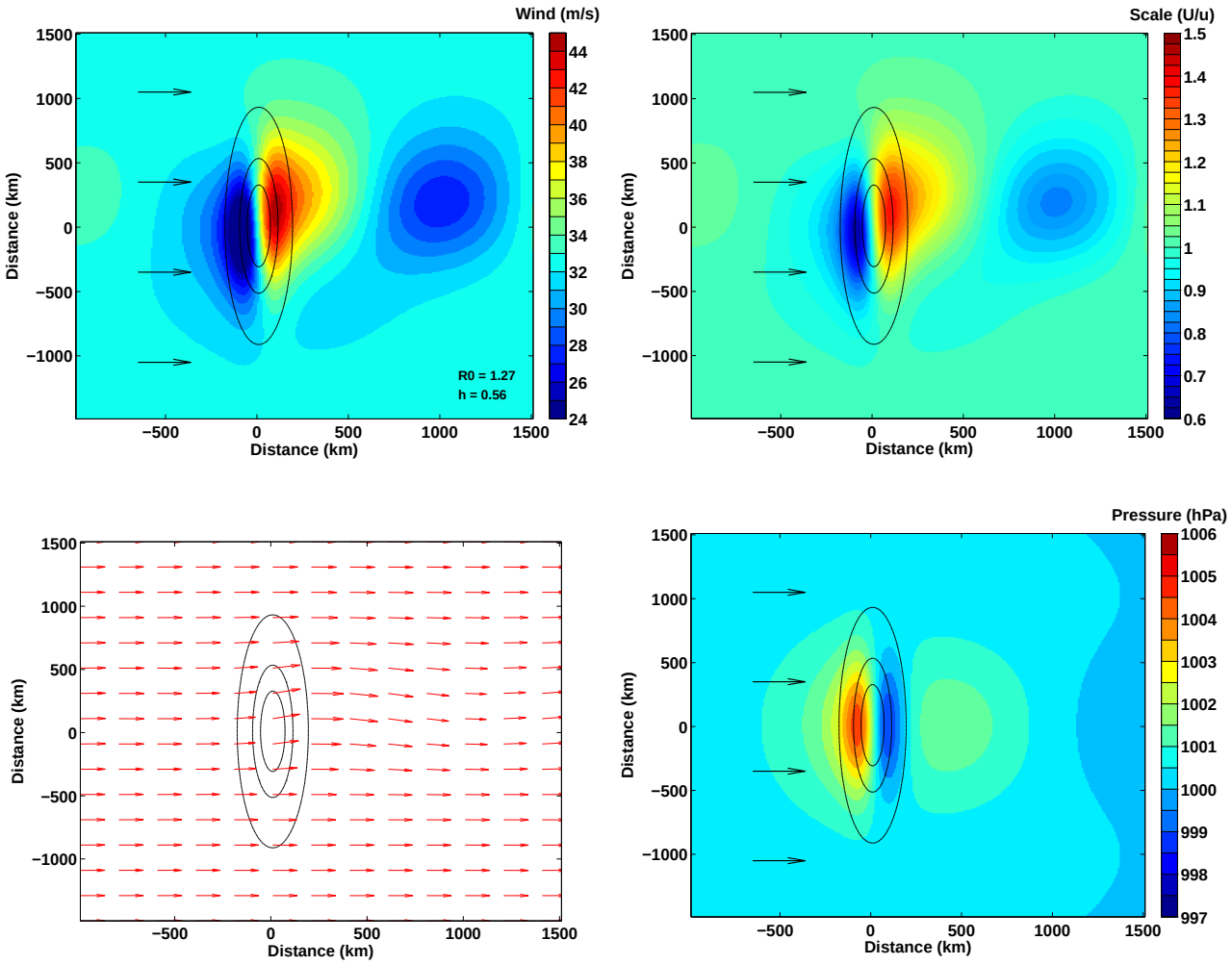

Figure 5.12: Same as in Figure 5.7, but the atmospheric stability, in potential temperature, was increased to 4 K/1000 m.

5.3 Summary of the WRF Model Verification

- The simulated pressure pattern over Southern Norway from the WRF model was more or less equal the one from the analysis done by the Norwegian Meteorological Institute, for both 1800UTC the 25th and 0000UTC the 26th of December 2011. However, compared to the analysis, the model underestimated the strength of both Dagmar and Cato by 10 hPa and 5 hPa, respectively.

- The WRF model underestimated the average wind speed along the coast by $1.39\,\mathrm{m\,s^{-1}}$. On the other hand, the median showed no underestimation. The WRF model did a good job simulating the wind speed along the coast, but at certain stations the underestimation of the wind was very pronounced. In the moutain area, the WRF model overestimated the average wind speed and the maximum wind speed, for both mean and median. The overestimation of the average wind speed, for the six selected stations, was largest for the inland stations. The WRF model overestimated the average wind speed by $3.43\,\mathrm{m\,s^{-1}}$ for both mean and median, and the average maximum wind speed was even more overestimated. It should be mentioned that the differences between the WRF model and the observations were largest where the most extreme wind events were observed.

- The underestimation of the WRF wind speed was pronounced for the westernmost stations (e.g., at Kråkenes lighthouse and Svinøy lighthouse). The reason was probably the wind shadow that occurred along the western coast, as a consequence of the flow being retarded by the presence of Langfjella. If the high pressure region on the windward side (that slowed down the wind) was less pronounced, the area of very strong wind may have reached the stations located at the northwestern coast. A WRF simulation of Dagmar performed by Harstveit (2012) also resulted in underestimation of the wind speed for the westernmost stations.

- For the six selected stations (Veiholmen, Kråkenes lighthouse, Utsira lighthouse, Lista lighthouse, Juvvasshø and Oslo-Blindern) the model, on average, underestimated the wind speed for all the stations except for Oslo-Blindern, where the model overestimated the wind speed. At the time of the strongest observed wind speed at Kråkenes lighthouse (Figure 5.5b) the model underestimated the mean wind speed by more than $20\,\mathrm{m\,s^{-1}}$. For the smoothed curve (11 hour) in Figure 5.5, the model did a better job capturing the wind situation over several hours compared to the exact wind speed every hour. Still, the smoothed WRF data were lower than the smoothed observed data.

- Regarding the wind direction for the six selected stations, the WRF model results were almost identical to the observations. For the three northernmost stations (Veiholmen, Utsira lighthouse and Juvvashø) the modelled wind direction had a larger westerly component than the corresponding result from the observations (from 0600UTC until 2100UTC the 25th). This is indicative of a too weak stability in the WRF model.

- The most pronounced similarity between the results from the realistic run (linear model), the WRF control run and the observations was the exisitence of the upstream wind shadow. The jet down the lee side of the mountain, present in the realistic run, was neither present in the WRF control run nor in the observations. The acceleration along the northwestern coast of southern Norway

was not present in the results from the realistic run. The reason for that may be that the realistic run did not have the "corner" located at Stad, which can create tip jets, but also small changes in the upstream wind direction can be crucial for the strength and even the existence of the "left side jet" (Barstad and Grønås, 2005).

- The results from the sensitivity runs, carried out by the linear wave model, show that the wind pattern (and also the pressure pattern) was sensitive to changes in the key peremeters (wind speed, wind direction, atmospheric stability, and height of the mountain). By only changing the upstream wind direction from westerly to southwesterly the "left side jet" varied from almost non-existing to very pronounced. The direction-sensitivity in the existence of a left side jet, together with the too pronounced upstream wind shadow in the WRF output, may be the reason why the WRF wind speed for the westernmost stations differred from the observations.

Chapter 6

Modeled Effect of Topography

The aim of this chapter was to use the WRF model to see how different topographies would have modified the high wind speed and wind direction caused by Dagmar. In addition to simulating Dagmar with the best resolved topography (the control run), two other model runs were carried out: The second run was a scenario where the complexity of the original topopgraphy in Southern Norway was smoothed out (the smooth topography run), and the third run was a scenario where the topography was completely removed (flat topography run). Figure 6.1 shows the topography in the three different WRF simulations.

6.1 The Pressure Fields

The pressure field gives a good indication on the large scale wind speed and direction. Plotting the isobars can give an indication on whether the different topographies changed the pressure pattern over Southern Norway. The simulated pressure lines produced by the three runs are shown in Fig. 6.2.

Offshore, the pressure fields for the three runs were almost identical. The deviation between the fields happened when the flow in the topography-runs approached the downstream mountain range. One of the reasons for the difference may be that the flow transferred momentum to the mountain, i.e. the flow tried to "push" the mountain, resulting in a positive pressure perturbation on the windward side and at the top of the mountain, and a negative pressure perturbation on the lee side. This "pushing" is dependent on the atmospheric stability; if the atmosphere needs to do work against the stability, i.e., the atmosphere is stable, more of the flow would be blocked, and the pressure here would be higher than if the stability was low and much of the flow could pass the mountain more or less unaffected. Another explanation for the pressure pattern visible in the runs with topography could be conservation of potential vorticity, which is a balance in the relation between the absolute vorticity and the depth of the fluid[1]. This balance implies that when a flow starts to climb a mountain, the thickness of the fluid layer decreases and the air column will be compressed, forcing the absolute vorticity to decrease in the order to maintain the balance. As a consequence, the compression of the air column resultes in an anticyclonic motion, hence an increase in the atmospheric pressure. When the air flows down the lee side of the mountain the air column stretches and the absolute vorticity increases. This scenario generates cyclonic motion, resulting in lower pressure on the lee side of the

[1]Conservation of potential vorticity: $\frac{\zeta+f}{h} = const$, where ζ is the relative vorticity, f is the planetary or background vorticity due to Earth's rotation (Coriolis) and h is the depth of the fluid.

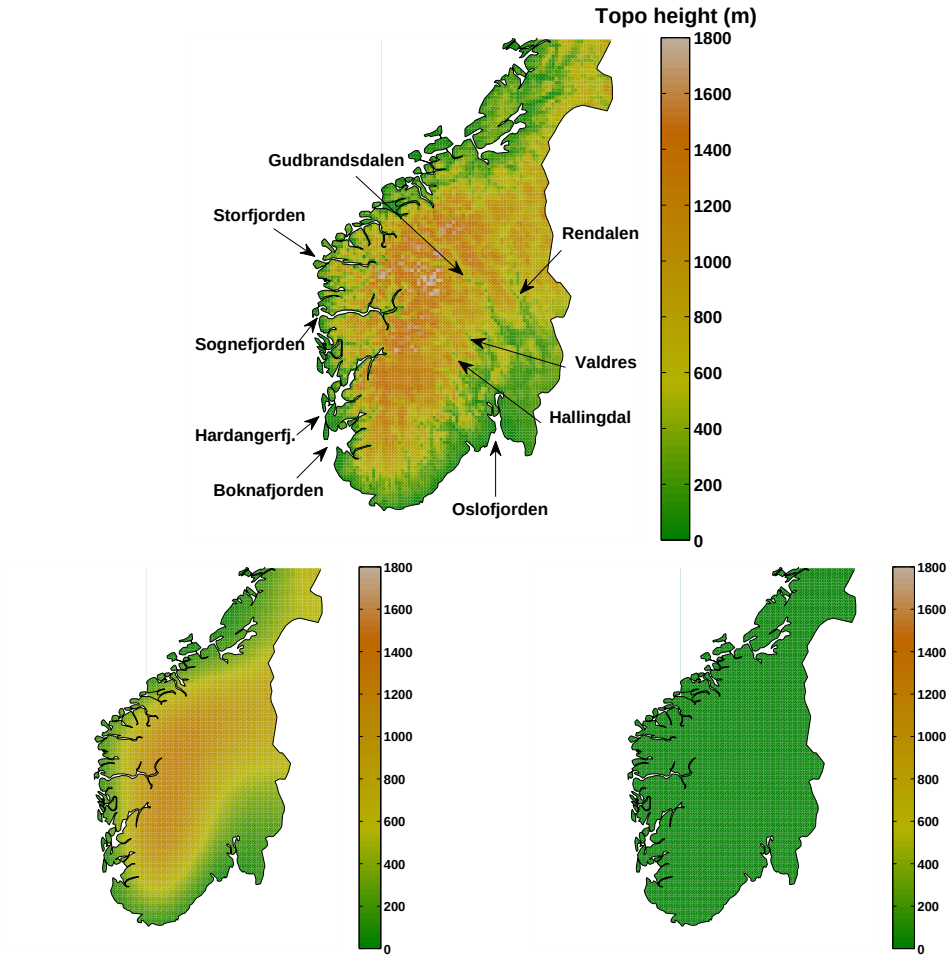

Figure 6.1: The topography (height above sea level [m]) for the three different WRF runs. The upper panel shows the topography from the control run, together with the names of some valleys and fjords. The lower left and lower right represent the topography used in the smooth topography run and flat topography run, respectively.

mountain (Holton and Hakim, 2012). A third reason may be thermally produced pressure perturbations. The flow that climbs the mountain gets adiabatically cooled, the density then increases making the heavy air sink to the ground and produce a high pressure anomaly.

Either of the above explanations could create a positive pressure perturbation in front and on top of the mountain and a negative perturbation on the lee side. However, due to the very strong winds caused by Dagmar, the atmosphere was probably near-neutrally stratified, and much of the flow traversed over the mountain. Thus, blocking of the flow and pushing of the mountain are not likely the processes that caused the pressure anomaly. However, the conservation of potential vorticity with compression and stretching of air colums, together with the adiabatically cooling and warming of the air, are the most reasonable explanations. According to Bernoulli's equation (see Chapter 4), when following a parcel's trajectory, there is a balance between the parcel's kinetic energy, the pressure and the potential energy. When the flow approached the mountain at constant height, the pressure increased forcing the kinetic energy to decrease. A decrease in the kinetic energy resulted in weaker wind speed which impaired the balance between the pressure gradient force and the Coriolis force. This caused some of the flow, in this case, to distort northwards until

the balance again was restored. The same thing can be seen in the pressure field at 2300UTC. This kind of pressure pattern are often associated with a Rossby-number varying around unity ($R_0 \sim 1$, see Section 2.2), and are therefore said to be intermediate, quasi-geostrophic flows[2], characterized by asymmetric flow around an obstacle (Smith, 1979, 1980).

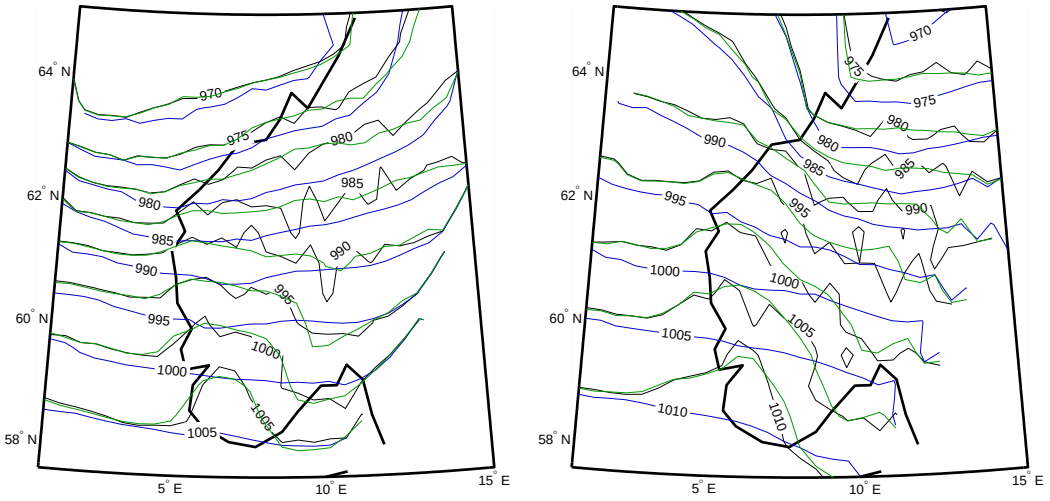

Figure 6.2: Pressure fields from the three WRF runs. The black line corresponds to the control run, the green line is the smoothed topography run and the blue line is the flat topography run. Left panel shows the pressure field at 1900UTC the 25th of December 2011, while the right panel shows the pressure at 2300UTC the same day.

6.2 The WRF Wind Speed Patterns

To get an overview of the result from the different WRF model runs, the wind speed patterns over Southern Norway were plotted, for the two times when the maximum wind speed occured in the observations (at 1900UTC and 2300UTC the 25th, see Figure 4.3). The results are shown in Figure 6.3.

A comparison of the control run and the smooth run shows that the complex topography created higher wind speeds in Langfjella, but lower wind speeds many places in the lee of the mountain range. The maximum wind speed in the control run was between 35-40 $\mathrm{m\,s^{-1}}$, both at 1900UTC and 2300UTC, while the maximum wind speed in the smooth topography run was between 30-35 $\mathrm{m\,s^{-1}}$ at 1900UTC, and 35-40 $\mathrm{m\,s^{-1}}$ at 2300UTC. The offshore wind patterns were almost identical for these two runs, especially at 1900UTC. The wind shadow south of Kråkenes lighthouse was more pronounced in the control run than in the smooth topography run. This suggests that more of the flow was affected by the mountain in the control run due to the higher mountain tops. The largest difference between the control and the smooth topography run was the disturbances in the wind field in the lee of Langfjella (the streaks of alternating high and low wind speed), visible in the control run. See also the upper panels in Figure 6.4. These disturbances were probably caused by

[2]In quasi-geostrophic flow, the acceleration following an air parcel is equal to the difference between the Coriolis force and the pressure gradient force. The wind is replaced by its geostropic value, and are therefore non-divergent, which implies that the vertical displacement are solely determined by the ageostrophic part of the wind (Holton and Hakim, 2012).

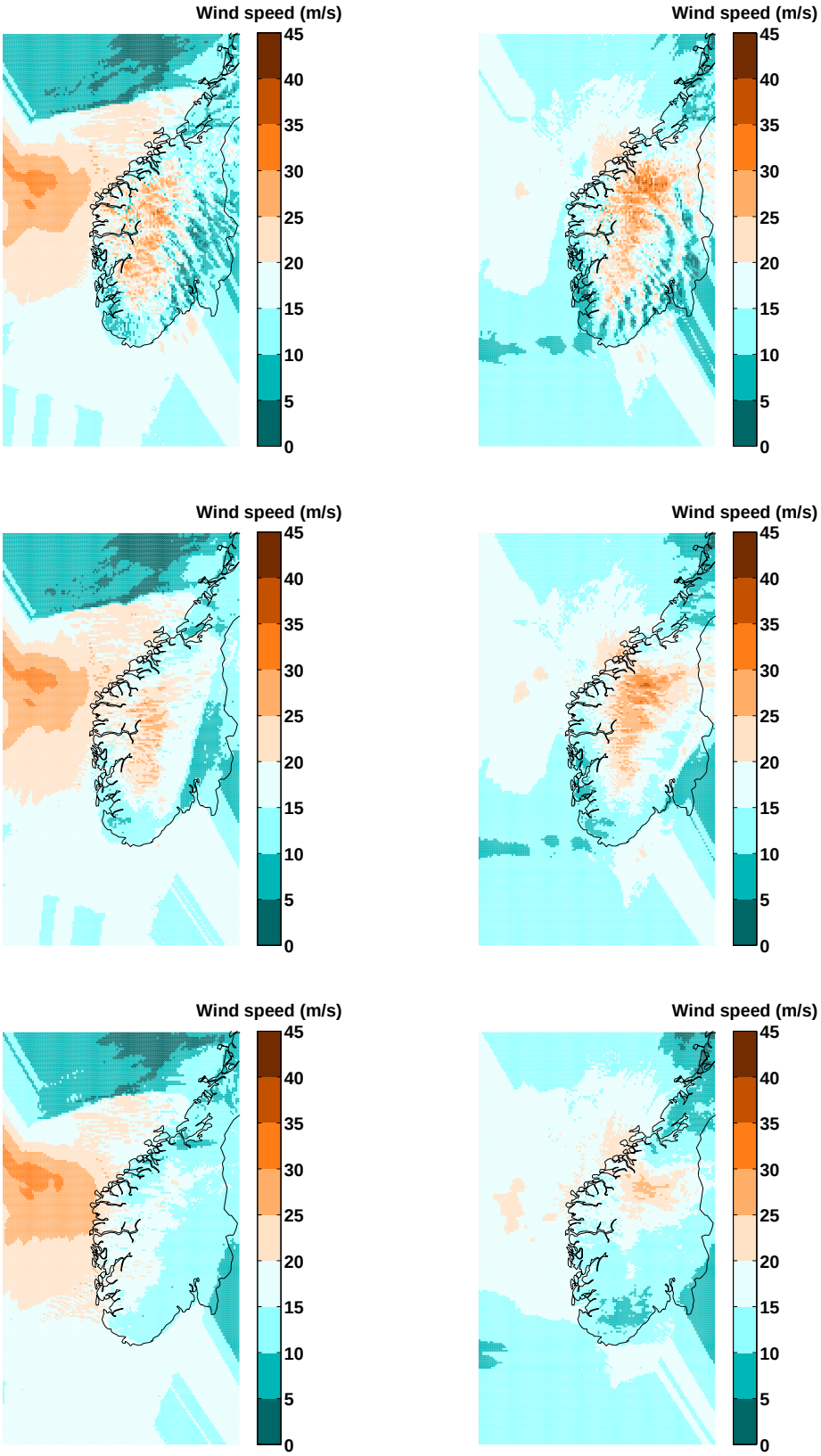

Figure 6.3: Simulated wind speed pattern for all the WRF runs. The figures in the left colum show the instantaneous 10-m wind speed from 1900UTC the 25th of December 2011, while the right column corresponds to 2300UTC the same day. The two figures in the upper row show the wind speed pattern from the WRF control run. The two figures in the middle row show the result from the smoothed topography run, while the two lower figures correspond to the wind speed pattern from the flat topography run.

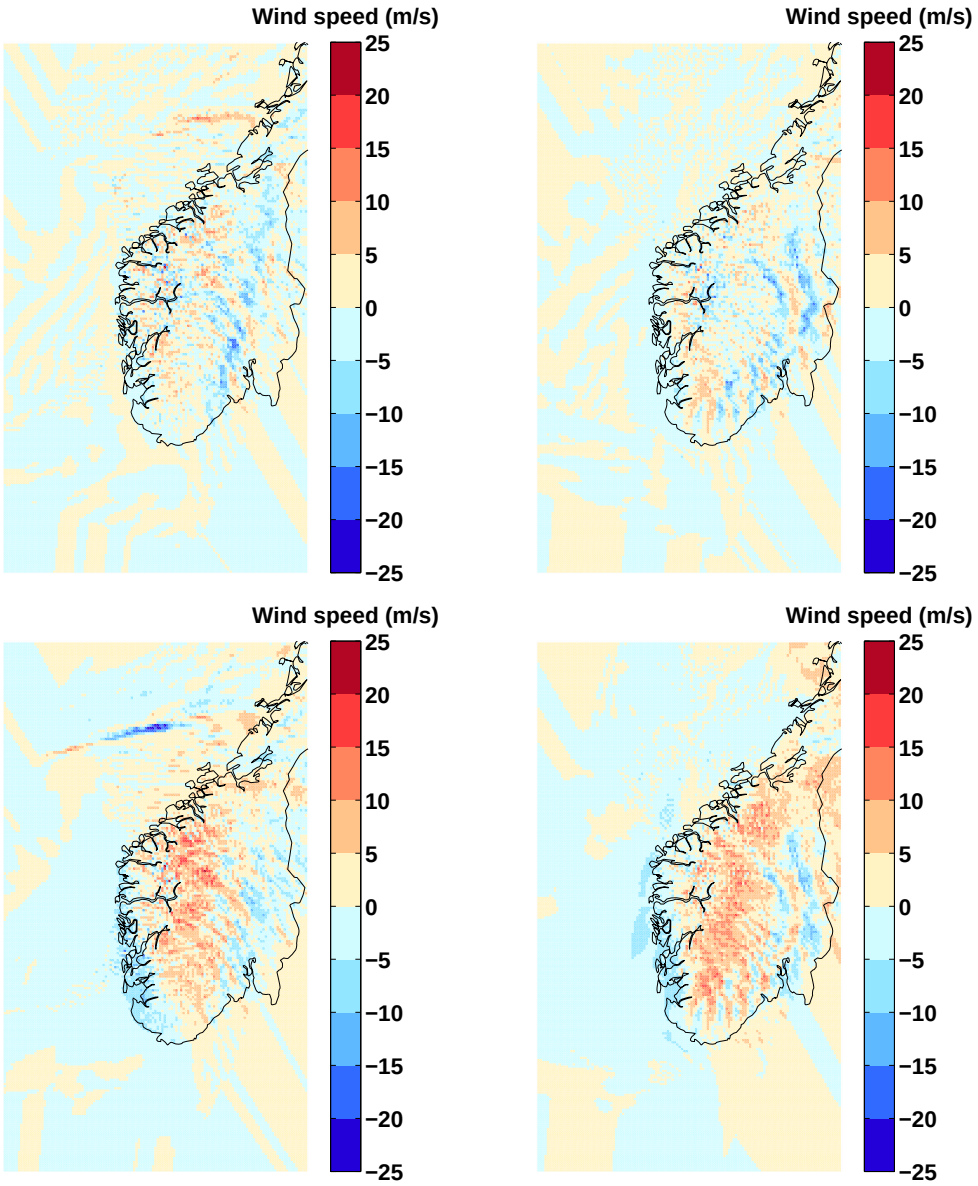

Figure 6.4: Difference in the wind speed pattern between the three WRF model runs. The two upper panels show the difference between the control run and the smooth topography run. The two lower panels show the difference between the control run and the flat topography run. The red colors indicate when the wind speed from the control run was larger, and the blue indicates when the wind from the smoothed/flat topography was larger. The figures in the left colum show the difference in the wind speed patterns from 1900UTC the 25th of December 2011, while the right column corresponds to the difference at 2300UTC, the same day.

all the long and narrow valleys, present in the control run. According to Whiteman and Doran (1993), the wind speed in a valley may depend on the component of the ambient geostrophic wind which is in alignment with the along-valley axis. At 2300UTC the 25th, the large scale wind direction was more or less perpendicular to the along-valley axis, for both Rendalen and Gudbrandsdalen. This may be the reason for the wind shadow in these valleys at that time. At 1900UTC the large scale wind direction had a larger component in the along-valley axis, and hence the wind speed inside the valleys was higher.

When comparing the control run and the flat topography run (upper and lower panels in Figure 6.3), the offshore wind patterns were more different than the offshore patterns between the control and smooth topography run. The strong winds to the south of the low (the orange bulb offshore in Figure 6.3, left column), reached further inland in the flat topography run than in the control run. The underestimation of the wind speed from the WRF model (compared to the observations) was very pronounced for these westernmost stations (see Chapter 5). The reason was probably due to the wind shadow that occurred along the western coast in the runs with mountains. If the high pressure region (that slows down the wind here) on the windward side would have been less pronounced, then the area of very strong winds, located offshore, would have reached the westernmost stations, like it did in the flat topography run.

Offshore the northwestern coast, the wind speed was weaker in the flat topography run compared to the control run (1900UTC the 25th). Since no mountain was present in the flat run, no high pressure perturbation occured on the windward side, and the left-side jet was absent. Comparing the wind speeds in the mountain region, the wind was weaker in the flat topography run compared to the control run. This was probably by virtue of the difference in height above sea level. For some places east of the mountain range the wind speed was higher in the flat topography run compared to the control run (especially at 2300UTC). This was probably due to the effects of the complex topography in the control, creating local wind shadows.The maximum wind speed in the flat run was 20-25 $\mathrm{m\,s^{-1}}$ at 1900UTC, and between 25-30 $\mathrm{m\,s^{-1}}$ at 2300UTC, compared to the maximum wind speed of 35-40 $\mathrm{m\,s^{-1}}$ in the control run. The higher wind speed inland (where the mountain would have been) in the flat topography run was caused by the difference in the aerodynamic roughness length[3]. This area still had the same friction as a mountain, and not forest or low land terrain, and hence the wind speed was significantly higher in this area.

The wind shadow on the southwestern coast, present in the control run and in the smooth topography run, was not present in the flat topography run. Depending on the wind direction, there were variations in the northward extent of this wind shadow. When the offshore wind direction was southwesterly (1900UTC the 25th), the wind shadow stopped at Kråkenes lighthouse (the westernmost point of Norway). When the offshore wind direction had turned more towards northwest (2300UTC the 25th), the shadow extended further north. At this time, the wind shadow was also more pronounced south of Kråkenes lighthouse. The wind shadow only occurred in the runs with topography; in the flat run the flow was not slowed down by the mountain induced high pressure region. Hence, the flow did not get disturbed by the imbalance between the pressure gradient force and the Coriolis force. This resulted in an absence of the left-side jet and wind shadows. This in agreement with the findings in Barstad and Grønås (2005).

[3]The aerodynamic rougheness length (Z_0) is a measure on the height above ground where the wind speed is zero. The higher the surface friction is (i.e. forest and bushes) the larger the aerodynamic roughness length will be. (Stull, 1988)

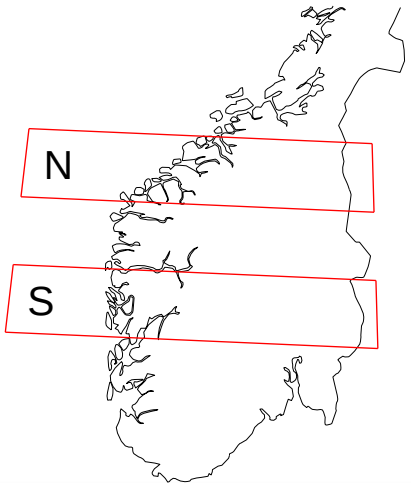

Figure 6.5: Map indicating the two transects, southern (S) and northern (N). The northern section spans from 62°-63°N, while the southern section spans from 60°-61°N. Both sections span over longitudes 2°-13°.

6.3 Southern and Northern Transects

Figures 6.3 and 6.4 contains detailed information about the wind patterns from the three WRF model runs. Model data from two regions of interest were therefore extracted to be able to investigate and capture the main wind pattern across Southern Norway. Based on the previous figures, the choice of the two sections was made where the difference between the runs was largest, namely north and south of the westernmost stations. The two sections can be seen in Figure 6.5. Section N (northern) spanned from 62°-63°N and 2°-13°E. Section S (southern) covered an area from 60°-61°N and over the same longitude interval as section N. Comparisons between the control run and the smooth topography run, and between the control run and the flat topography run were carried out. Only the comparison between the control run and the flat topography run for the southern region will be discussed in detail. Rest of figures can be seen in Appendix B

Figures 6.6 and 6.7 show cross sections of data in region S, for control run and the flat topography run, at 1900UTC and 2300UTC the 25th, respectively. The mountain height, wind speed, wind direction, and potential temperature (the four lowest panels) were averaged in bins of 0.1° longitude and their respective 1° latitude. The temperature profiles (the four upper panels) were averaged a bit different; the upper left panel was averaged over its respective 1° latitude and the 2° wide bins centered at 3°E, 6°E, 9°E and 12°E, respectively. The temperature profiles were made to see how the atmospheric stability changed from offshore (centered at 3°E), costal area (centered at 6°E), mountain area (centered at 9°E) and in land (centered at 12°E).

Southern Region at 1900UTC the 25th

In Figure 6.6 the results from section S for 1900UTC the 25th are shown. For both control run and the flat topography run the highest wind speed was found offshore, around $23\,\mathrm{m\,s^{-1}}$. The wind speed abated towards the coast for both runs, but the decrease in wind speed was proportional to the southerly component of the wind direction in the same area; the flat run had the smallest decrease in wind speed and

the smallest southerly component in the wind directon, compared to the control run. This is in agreement with the distortion of the isolines in Figure 6.2. The difference in the wind direction can be explained by the imbalance between the pressure gradient force and the Coriolis force caused by the presence of the mountain (see Section 2.3.1 for further explanation). The wind speed in the flat run continued to decrease inland, while the wind speed for the control run increased, and reached maximum wind speed ($25\,\mathrm{m\,s^{-1}}$) at the top of the mountain, followed by a decrease in the wind speed on the lee side. The wind speed in the control run fluctuated more than the wind speed in the flat topography run. This was probably due to the complex topography, since the fluctuations were only present over land. The wind speed in the control run did also increase and decrease on the exact some places as the topography height increased and decreased (see the bottom panel in Figure 6.6).

The potential temperature line for the run without topography was more or less the same throughout the whole longitude interval, and reached the maximum value of 283°K around 8° longitude. The potential temperature line for the run with topography increased as the air started to climb the mountain and reached the maximum value of 288°K where the mountain range was highest. Around 11°E the potential temperature curve for the control run suddenly dropped 3°K back to its upstream value of 284°K.

The offshore atmospheric stability (centered at 3°E) was almost neutral compared to the dry adiabatic lapse rate[4] (see the upper left panel of Figure 6.6). In the next panel (centered at 6°E) the stability had increased for both runs, but the flat topography run had in addition a weak and shallow inversion layer close to the ground. In the third panel (centered at 9°E), the stability had further increased, and the inversion in the flat topography run was stronger and reached further up in the atmosphere. The shallow inversion layer, in the flat topography run, was probably caused by warm air advection from the sea on top of the cold snow covered ground. The inversion layer was probably so shallow because of the strong winds mixed the air column almost all the way down to the ground. This inversion layer may also have influenced the 10-m wind speed in that run, which prohibited the strongest wind speeds to reach all the way down. In the right most panel the stability had increased further. The atmosphere in the flat topography run was a bit more stable than the control run, but the inversion layer was gone.

Southern Region at 2300UTC the 25th

Figure 6.7 depicts the results from 2300UTC for the southern region (S). The offshore wind speed for both runs was lower than at 1900UTC, but the wind speed from the flat topography run was higher than in the control run. As the air approached the coast of Norway, the wind speed from both the runs decreased, but the wind speed from the run with topography decreased the most. Here, it is more evident that the wind from the control run had to go around the mountain; it started out as pure westerly wind, as the air reached land the wind turned to a more southwesterly direction, as the air reached the mountain top the wind direction turned back to westerly, and then to northwesterly further inland. From this it is evident that the flow created a shallow anticyclone on the windward side, and cyclonic motion on the lee side. This can also be seen in the results from the linear wave model in Section 5.2. The wind from the flat run got a small northerly component at the coast, then shifted to a more southwesterly direction inland. The influence of the two valleys, Gudbrandsdalen and Rendalen from the control run, is very pronounced

[4]The dry adiabatic lapse rate was here set to be -9.8 °K /1000m

in Figure 6.7. At this time, the large scale wind was almost perpendicular to the along-valley axes, and according to Whiteman and Doran (1993) the along-valley wind will then be minimal.

The stability of the atmosphere increased inland (see the four upper panels in Figure 6.6). As seen in Figure 6.6, the flat topography run got an inversion layer over land. The inversion at 2300UTC was stronger than at 1900UTC because the temperature near the ground had decreased; the air in a warm sector will heat the cold ground from above, and as soon as the cold front passes, the ground will start to loose heat to the colder air above. At 1900UTC Dagmar's cold front had just passed (maybe not for the easternmost stations), and the radiative cooling of the ground had just started, so the ground was still heated from the air in the warm sector. At 2300UTC the ground had been exposed to the cold air behind the cold front for a longer time, and hence the loss of heat was larger and the temperature near the ground was colder. That is probably why the ground temperature was higher at 1900UTC than at 2300UTC. A situation with a warmer ground below a colder atmosphere is unstable. The reason why the temperature profile in the flat run was still stable near the ground was the advection of the much warmer air from the Atlantic Ocean.

Many of the observed features for the southern region are also seen for the northern region (see Figures B.1 and B.2 in Appendix B). One of the major differences was that the offshore wind speed at 1900UTC was much higher for the northern region than for the southern region; the cross-section for the northern region included the very high wind speed south of the low pressure center (see left column of Figure 6.3), which might have been a sting jet (Schultz and Sienkiewicz, 2013).

The results from the comparison of the control run and the smooth topography run can be seen in Appendix B, Figures B.3 to B.6. The results for the two runs were very similar, and will therefore not be discussed.

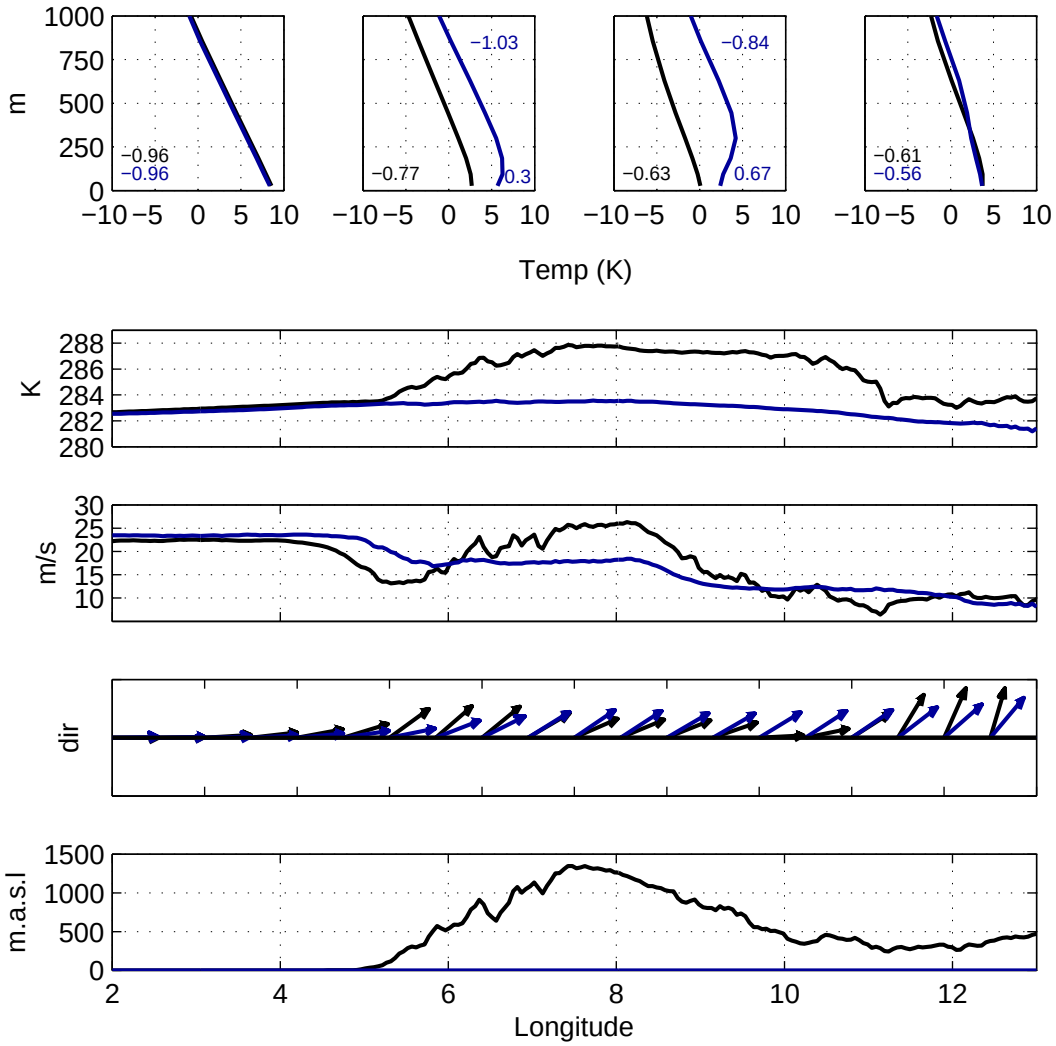

Figure 6.6: Cross sections of the data in southern (S) region, for the control run and the flat topography run for 1900UTC on the 25th of December 2011. The black line shows to the results from the control run, while the blue line shows results from the flat run. The mountain height, wind speed, wind direction, and potential temperature (the four lowest panels) were averaged in bins of 0.1° longitude and their respective 1° latitude. The temperature profiles (the four upper panels) were averaged a bit different; the panels were averaged over its respective 1° latitude and the 2° wide bins centered at 3°E, 6°E, 9°E and 12°E, respectively. The lowest panel shows the topography height in meters above sea level (m.a.s.l). The next panel shows the instantaneous 10-m wind direction followed by the corresponding wind speed. Next is the potential temperature (in roughly 450 m above the topography) in degree Kelvin, and the four upper panels show the temperature gradient of the atmosphere, given in number of degree Kelvin per hundred meters.

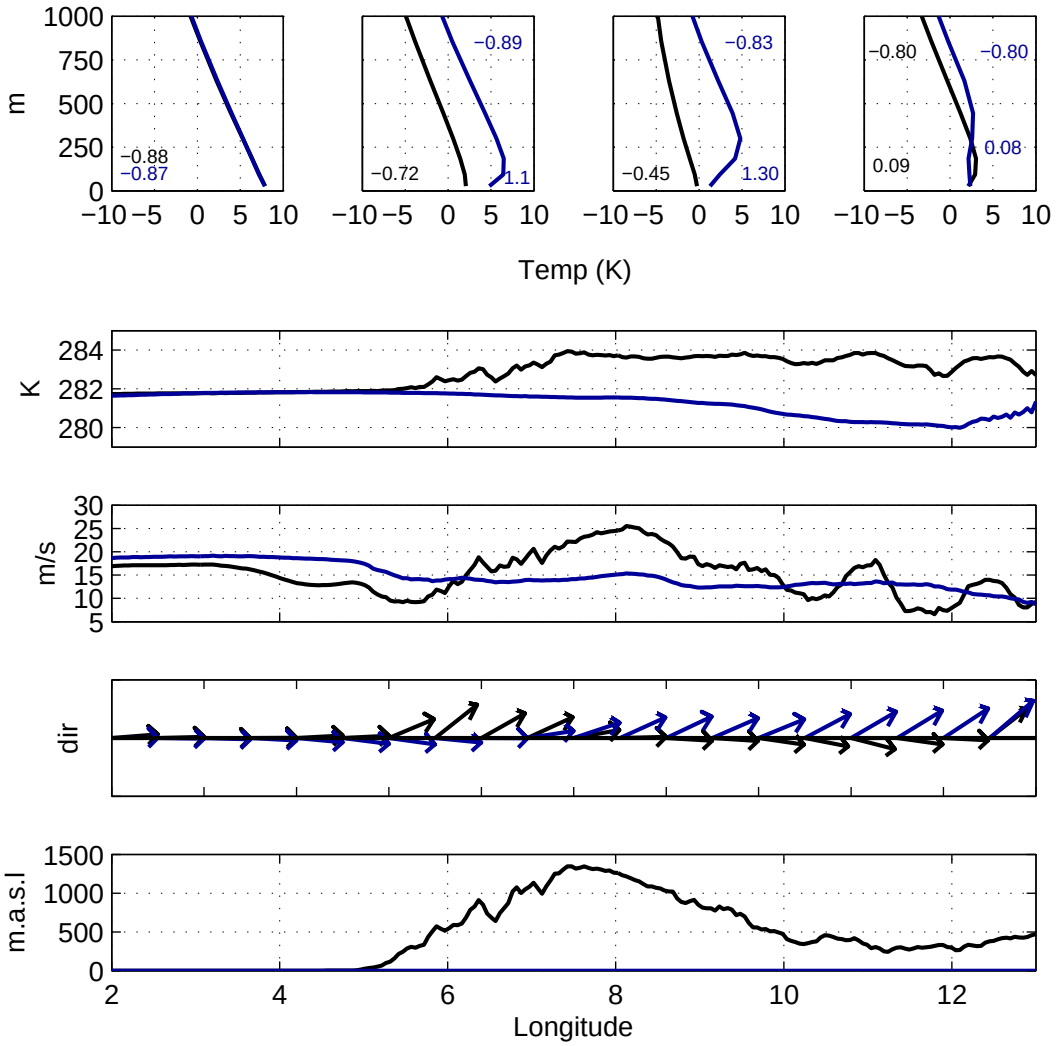

Figure 6.7: The same as Figure 6.6, but for 2300UTC on the 25th of December 2011.

6.4 The Selected Stations

The timeseries of the simulated 10-m wind, for the six selected stations were also investigated: a) Veiholmen, b) Kråkenes lighthouse c) Utsira lighthouse, d) Lista lighthouse, e) Juvvasshø and f) Oslo-Blindern (see Figure 4.5 for the location of the six stations).

For Veiholmen lighthouse (Figures 6.8 and 6.9, a), no clear pattern in the difference between the runs was found. The flat topography run had lower wind speed when the two other runs reached their maximum wind speed (around 1900UTC the 25th). In the control run and smooth topography run, the wind direction turned clockwise from 180° to 240° and the wind speed increased rapidly. However, this was not the case for the flat topography run. Barstad and Grønås (2005) concluded in their paper that the jet along the northwestern coast of Southern Norway was most pronounced when the wind came from southwest. That may be what happened when the wind was turning from 180° to 240°, and the wind speed responded by an abrupt increase from $8\,\mathrm{m\,s^{-1}}$ to almost $25\,\mathrm{m\,s^{-1}}$.

For Kråkenes lighthouse (Figures 6.8 and 6.9, b), the wind speed and direction from the smooth topography run more or less follows the curves from the control run throughout the whole period of interest. When the wind direction from the flat run was more westerly than the two other runs (around 1800UTC the 25th until 0600UTC the 26th) the wind speed from the flat run also exceeded the two other runs. When the wind direction had a larger westerly component, the positive pressure perturbation on the windward side of the mountain barrier was more pronounced, slowing down the wind speed, hence the wind speed in the flat topography run exceeded the wind speed from the two other runs. This was the case for all the coastal sites, except for Veiholmen lighthouse (Figures 6.8 and 6.9, b, c and d).

For the mountain station Juvvasshø (Figures 6.8 and 6.9, e), the wind speed for the flat run was lower than the wind speed for the two other runs during the whole period of interest. This may indicate that the wind speed increased with height. The three curves for the wind direction follow each other more or less all the time, except in the morning the 26th. At that time, the wind speed from the flat run turned anticlockwise to a more southerly direction, making the wind in the flat run reach its minimum value, probably due to the loss of kinetic energy through dissipation caused by the longer distance traveled over land.

The results for Oslo-Blindern are represented in the lower right panel in Figures 6.8 and 6.9. The difference between the three runs was larger for this station; all the curves for the wind direction increase and decrease, on average, at the same time, but the curve from the control run has larger fluctuations than the two other curves. It looks like the wind speed from the control run was lower than the wind speed from the two other runs throughout almost the entire time period. This can also be seen in Figure 6.9 f).

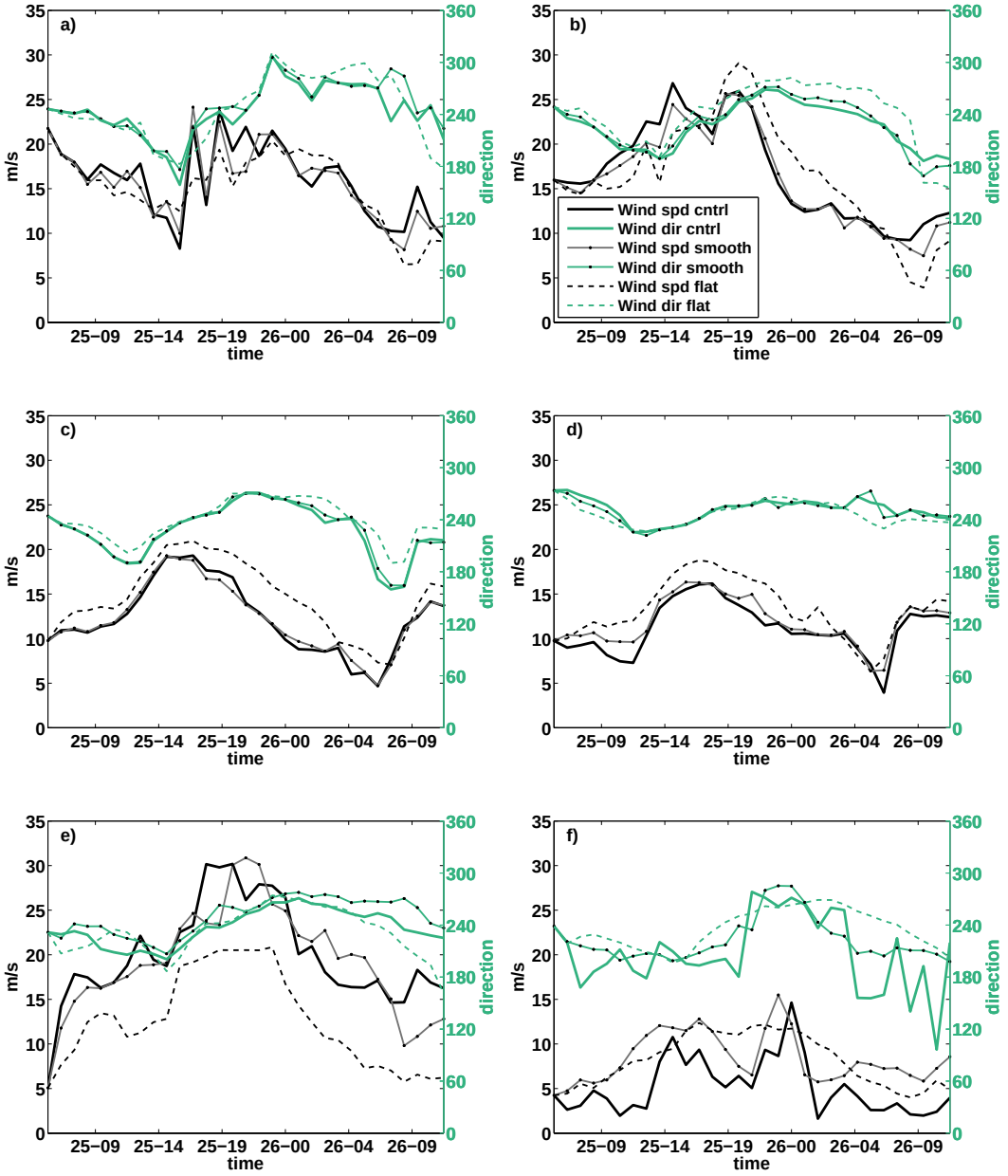

Figure 6.8: Timeseries of the 10-m wind speed (black curves) and the corresponding wind direction (green curves) from the WRF model, from 25th of December 2011 at 0600UTC until 1200UTC the 26th. The solid thick lines correspond to the WRF control run, the solid lines with dots correspond to the run with smoothed topography, while the dashed lines correspond to the run with flat topography, for six selected stations: a) Veiholmen, b) Kråkenes lighthouse, c) Utsira lighthouse, d) Lista lighthouse, e) Juvvasshø and f) Oslo- Blindern.

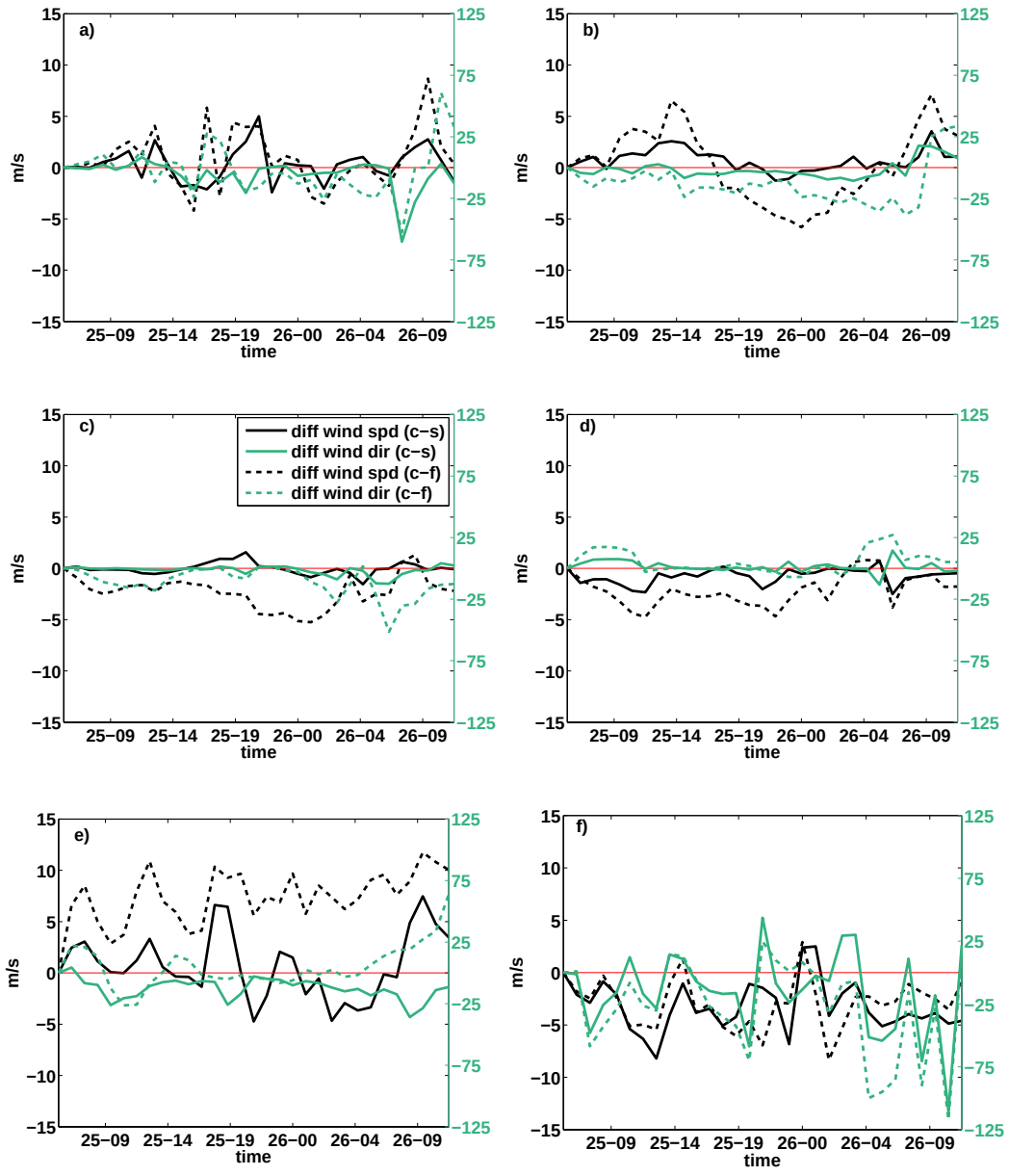

Figure 6.9: The same as Figure 6.8, but for the timeseries of the difference in the WRF model wind speed between the three runs.

6.5 Gravity Waves

A good indication of the motion in the atmosphere can be obtained by studying the potential temperature field, shown in Figures 6.10 and 6.11.

The difference in the wind patterns between the three WRF runs in the lee side of the mountain range was remarkble, especially between the control run and the smooth topography run (see Figures 6.3 and 6.4). A phenomenon that can cause such disturbances in the lee of a mountain is gravity wave motion in the atmosphere, caused by the interaction between the flow with and the topography (see Section 2.1). If the atmosphere is neutrally stratified, the air column is just pushed up by the topography, and no wave motion will appear. By looking at both the panels in Figure 6.10, and taking into account that the atmosphere was near-neutrally stratified (see upper panels of Figures 6.6 and 6.7), the air columns appear to be pushed up by the topography. The very strong winds of Dagmar mixed the entire air column, so the restoring force (the buoyance), to maintain a wave motion, was absent. Therefore, the interaction between the flow and the topography did not result in gravity wave motion. Some of the disturbances in the temperature field, in Figure 6.10, were probably an artifact from the extraction of the WRF data. At the given latitude, the point nearest 60.5°N latitude was extracted, possibly taking data from different potential temperature fields. No gravity wave motion was found in the potential temperature field for the smooth topography run, see Figure 6.11.

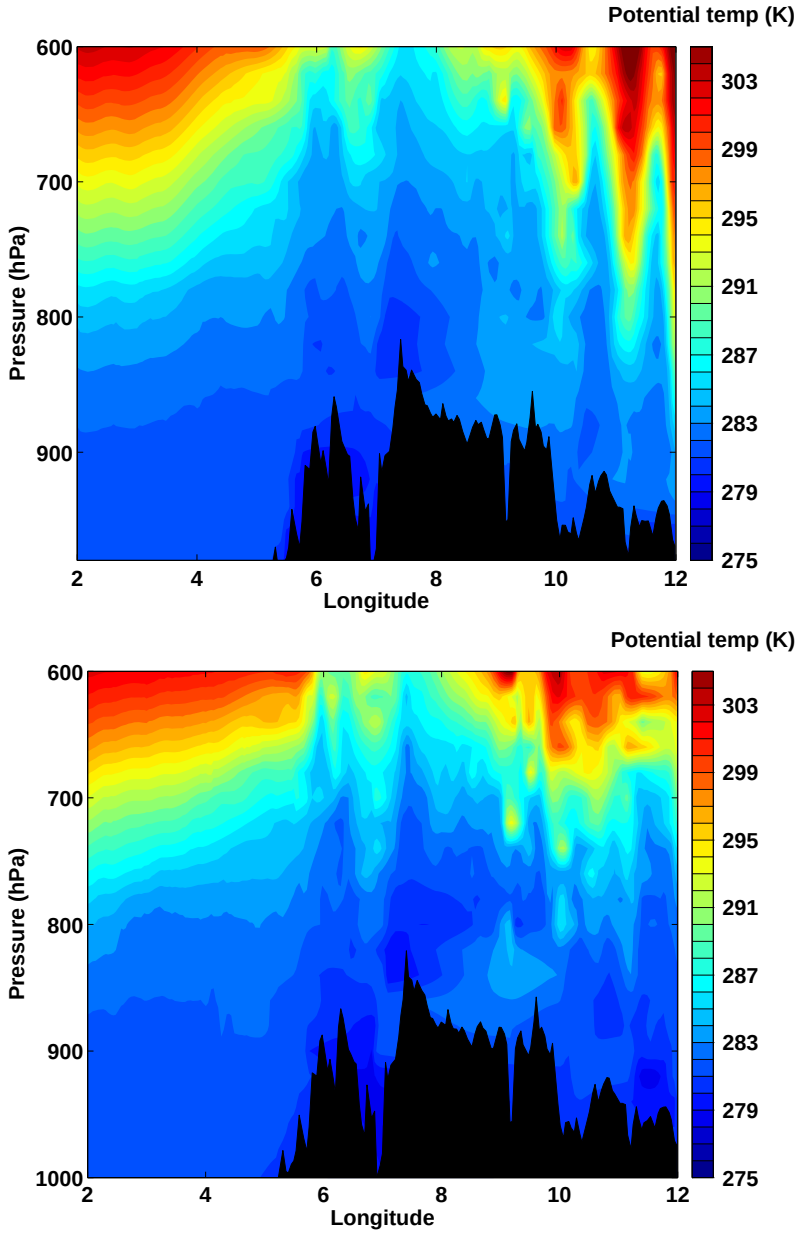

Figure 6.10: The potential temperature fields from the WRF control run, for 1900UTC (upper panel) and 2300UTC (lower panel) the 25th of December 2011. The cross section was taken at 60.5°N and from 2-12°E. The black field shows the topography height.

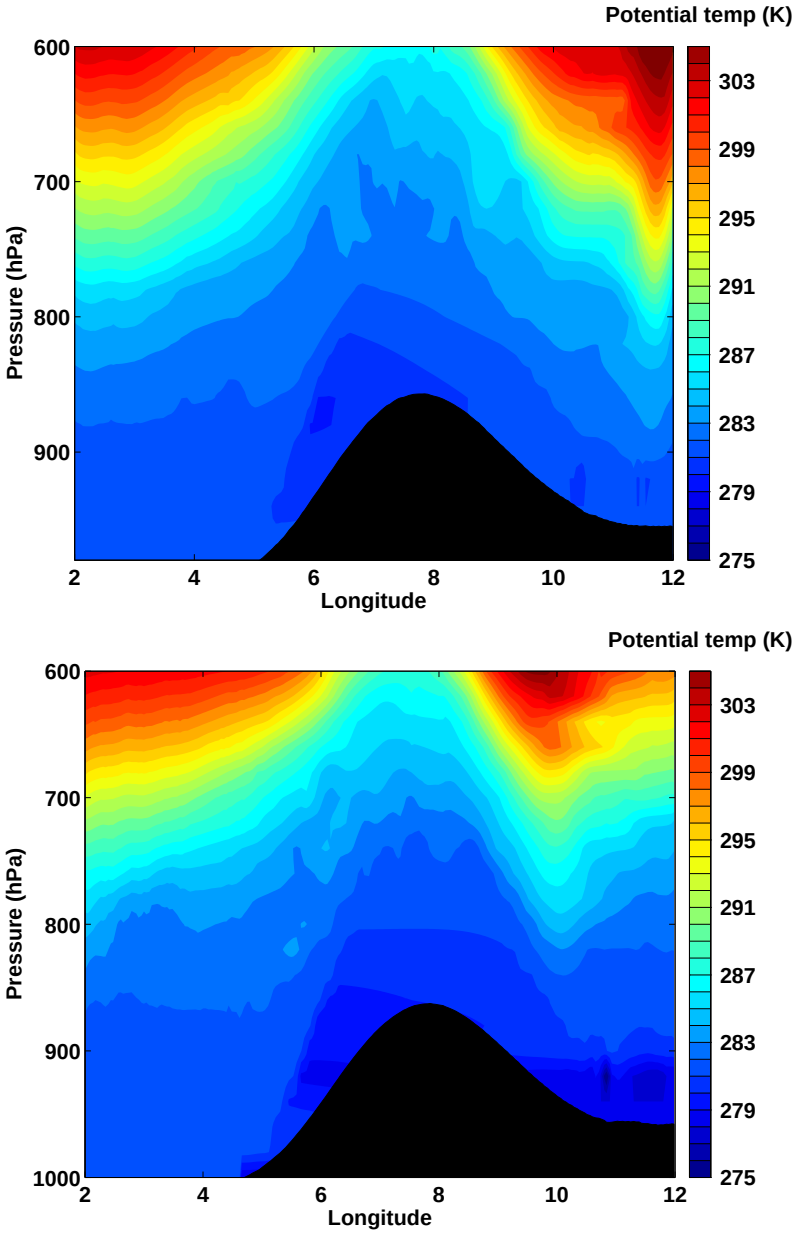

Figure 6.11: The same as in Figure 6.10, but for the smooth topography run.

6.6 Summary

- In addition to simulating Dagmar with the best resolved topography ("control run"), two other model runs were carried out. The second run was a scenario where the complexity of the original topopgraphy in Southern Norway was smoothed out ("smooth topography run"), and the third run was a scenario where the topography was completely removed ("flat topography run"). The reason for this was to see the effect of Norway's complex topography, and how the topography changed the strong winds caused by Dagmar.

- The difference in the pressure fields between the three runs over Southern Norway (Figure 6.2) was caused by the interaction between the flow and the topography. The pressure patterns for the runs with topography were characterized by a shallow anticyclone over the mountain and a local depression on the lee side. This pressure patterns in the topography runs were caused by adiabatically cooling of air and conservation of potential vorticity resulting in an impaired geostrophic balance.

- The main difference between the wind speed pattern (see Figures 6.3 and 6.4) from the control run and the smooth run was the disturbances in the wind speed pattern on the lee side of the mountain. It may look like the valleys Gudbrandsdalen and Rendalen (see upper panel of Figure 6.1) resulted in some kind of wind shadow at 2300UTC the 25th, when the wind direction in that area was westerly. The wind direction was then more or less perpendicular to the valley axis, and accoring to Whiteman and Doran (1993) thet can result in very low wind speed along the valley.

- From the comparison between the control run and the flat run, there was especially one clear difference, besides the much higher wind speed up in the mountain in the control run. The wind shadow on the western coast in the control run (see Figures 6.3 and 6.4) was not present in the flat topography run. Depending on the wind direction, there were variations in how far north this wind shadow extended. When the offshore wind direction came from southwest (1900UTC the 25th) the wind shadow stopped at Kråkenes lighthouse. When the offshore wind direction had turned into a more northwesterly direction (2300UTC the 25th), the shadow extended further north. At this time the wind shadow also got more pronounced south of Kråkenes lighthouse. This in agreement with the findings in Barstad and Grønås (2005).

- All the stations situated along the western and southwestern coast (Kråkenes lighthouse, Utsira lighthouse and Lista lighthouse) experienced higher wind speeds during the flat run compared to the topography runs. During the topography runs these stations were located in the area of the upstream wind shadow.

- There was no sign of gravity waves in the lee of Langfjella. The atmospheric stability was almost neutral making the restoring force minimal. The topography pushed the air columns up without creating any lee-waves (see Figures 6.10 and 6.11).

Chapter 7

Concluding Remarks

The aim of this thesis was to find out how the complex topography in Southern Norway affected the strong winds caused by the storm Dagmar, and not go into details about the corresponding synoptic situation. An observational study was carried out, together with high resolution simulations performed by the numerical model WRF to investigated the interaction between the flow and different topographies (see Section 3.1.9 for more information about the WRF runs). A linear wave model (Barstad and Grønås, 2005) was used to address the differences between the results form the WRF model and the observations.

The observational study showed that the highest observed 10-m mean wind speed (10 min average) was measured on the northwestern coast of Southern Norway, at Kråkenes lighthouse, $43.8\,\mathrm{m\,s^{-1}}$. Several stations along the northwestern coast measured a 10-m mean wind speed (10 min average) stronger than hurricane force ($>32.7\,\mathrm{m\,s^{-1}}$). The wind was also very strong in the mountain regions: Juvvasshø station measured a maximum wind gust of $64.7\,\mathrm{m\,s^{-1}}$. See Chapter 4 for figures and discussion of the observational study.

Schultz and Sienkiewicz (2013) stated that descending of air, associated with frontolysis, reaching a near-neutral boundary layer provides a physical mechanism for a phenomena called "sting jets", also called "the poisonous tail of the back bent occlusion" by Grønås (1995) (see Figure 4.1 for the back bent occluded front). The sting jet forms south of the low pressure center, and the wind direction is therefore often westerly. The off shore atmospheric stability at the time when Dagmar struck Norway was near-neutral and the conditions were favourable for creating such a jet. The high-momentum air situated higher up in the atmosphere was then able to penetrate through the atmosphere, all the way down to the surface, and create very high surface winds. This sting jet may be the reason why all of the selected stations (Veiholmen lighthouse, Kråkenes lighthouse, Utsira lighthouse, Lista lighthouse, Juvvasshø and Oslo-Blindern) experienced a rapid increase of the wind speed when the wind direction veered from a southwesterly to a westerly direction.

The WRF model was used to recreate the situation when Dagmar struck Norway (the WRF control run). These results were compared to the observations to get a validation of the WRF model. The simulated pressure pattern was very similar to the pressure pattern from the analysis, at both 1800UTC he 25th and 0000UTC the 26th. See Figure 5.1 and Figure 4.1 for the pressure patterns from the WRF model and the analysis, respectively. The WRF model underestimated the pressure in the core of Dagmar and Cato at both 1800UTC the 25th and 0000UTC the 26th, compared to the analysis of the Norwegian Meteorological Insitute. This underestimation could have affected the strength of the large scale wind speed, and hence the strength of

the sting jet.

For the six costal stations, from Torungen lighthouse in southeast to Kristiansund in northwest (see Figure 5.4 for the location of the stations), the WRF model underestimated the average wind speed by $1.39\,\mathrm{m\,s^{-1}}$, while the median showed no underestimation. For six selected stations in the mountain area (see Figure 5.4) the WRF model overestimated the average wind speed (by $3.16\,\mathrm{m\,s^{-1}}$ (mean) and $2.40\,\mathrm{m\,s^{-1}}$ (median)). The overestimation of the average wind speed was largest for the six selected inland stations. Here, the WRF model overestimated the average wind speed by $3.43\,\mathrm{m\,s^{-1}}$ for both mean and median. While, the WRF model did a good job simulating the wind speed along the coast, the model severly underestimated where the most extreme wind events were observed.

The underestimation of the wind speed by the WRF model was most pronounced for the western most stations (e.g. at Kråkenes lighthouse and Svinøy lighthouse). The reason was probably due to a too strong wind shadow that occured along the western coast; the presence of Langfjella retarded the flow on the windward side, creating a too strong high pressure anomaly. The region of very strong winds simulated offshore the northwestern coast (visible by the orange bulb in Figure 6.3) could have reached the westernmost stations if the high pressure anomaly on the wind ward side was less pronounced. It should be noted that a WRF simulation of Dagmar performed by Harstveit (2012) also resulted in underestimation of the wind speed for the western most stations.

The linear wave model was used in the attempt to understand the wind pattern generated by WRF, and to address the differences between the WRF model output and the observations, and also to find out how much of the observed signal that could be explained by simple linear theory. The most evident similarity between the result from the linear wave model with near observed wind and stability, the WRF model and the observations was the upstream wind shadow. The acceleration down the lee side of the mountain, present in the linear wave model, was absent both in the WRF model output and in the observations (see Figure 5.8). The reason for this may be the high surface friction due to forest, bushes, threes, houses etc., which was not included in the linear wave model. Both the wind speed patterns from the WRF model and the observations showed evidence of a left side jet, i.e. acceleration of the wind along the northwestern coast of Southern Norway, this was not the case for the linear model. See Section 5.2 for figures and discussion of the comparison. To investigate how changes in wind speed, wind direction, mountain height, and the atmospheric stability may have influenced the WRF model results, four sensitivity runs were carried out by the linear wave model. See Section 5.2.2 for the results and figures from the sensitivity runs. The results from the linear wave model showed that small changes in the key variables can have significant effect on the resulting wind and pressure patterns. From westerly to southwesterly upstream wind direction the left side jet varied from almost non-excisting to very pronounced, respectively. In addition, a higher atmospheric stability and a higher mountain forced more of the flow to go around the mountain and converge in the lee. If the value of several key parameters used in the WRF model differed from the observed values this may result in two very different wind patterns.

In addition to simulate Dagmar with the best resolved topography (the WRF control run), two other WRF model runs were carried out. The second run was a scenario where the complexity of the original topopgraphy in Southern Norway was smoothed out (the smooth topography run), and the third run was a scenario where the topography was completely removed (flat topography run). The reason for this was to see the effect of Norway's complex topography, and how different

topographies would have changed the strong winds caused by Dagmar. See Chapter 6 for the results, figures and discussion of the three scenarios. The difference in the pressure fields between the three WRF runs over Southern Norway (see Figure 6.2) was caused by the interaction between the flow and the topography. For the two runs with topography the pressure patterns were characterized by a shallow anticyclone on the windward side and over the mountain, in addition to a local depression on the lee side. The positive and negative pressure perturbations were caused by adiabatic cooling of the air as the flow went up the muntain, and warming of the air as the flow descent down the lee side of the mountain, together with conservation of potential vorticity. According to Bernoulli's equation this will result in a retarded flow wherever the pressure perturbation is positive, hence on the wind ward side and downstream of the mountain, and a accelerated flow wherever the pressure perturbation was negative (down the lee side). The most pronounced difference between the wind pattern from the WRF control run and the flat topography run was the wind shadow on the western coast of Southern Norway, which was visible only in the control run. The northern extent of this wind shadow varied with the direction of the wind speed. When the off shore wind direction was westerly the wind shadow stopped at Kråkenes lighthouse. When the wind direction came from northwest, the wind shadow extended further north, in addition the wind shadow south of Kråkenes got more pronounced. This is in agreement with the findings in Barstad and Grønås (2005). Out of the six selected stations (Veiholmen lighthouse, Kråkenes lighthouse, Utsira lighthouse, Lista lighthouse, Juvvasshø, and Oslo-Blindern), the ones situated along the western and southwestern coast experienced higher wind speed during the flat topography run compared to the control run and smooth topography run. The reason for this is due to the positive pressure perturbation, present only in the runs with a mountain, which slowed down the flow.

Future Work

There are other things that could have been investiated regarding the storm Dagmar: Since an investigation of the synoptic situation was excluded in this thesis, a more detailed analysis of the large scale pressure pattern, when Dagmar occured, would have been interesting. The synoptic situation when Dagmar and the New Year's storm from 1992 made landfall bear remarkable resemblance. A further investigation of why the two storms became so strong, and to find out if a certain large scale synoptic situation trigger these very strong and demaging low pressure systems, would have been valuable information for the forcasters.

From the theory of gap flows (see Section 2.4.1 for more information), the wind speed can reach anomalously high values in regions like fjords and valleys. It looks like some of the fjords in the WRF control run had a slightly different wind speed pattern inside the fjord compared to the smooth and flat topography run (where the fjords and valleys were excluded). It would be interesting to perform a high resolution simulation of what happend in one of these large fjords in Southern Norway, e.g. Sognefjorden (see Figure 6.1 for the location of the fjord).

In the attempt du make the results from the linear wave model more comparable to the results from the WRF model, it would have been interesting to include a boundary layer in the linear model.

Appendix A

Station Information

Station information			
Station name	**lat**	**lon**	**moh**
SARPSBORG	59.29	11.11	57
KJELLER	59.97	11.04	109
HAKADAL JERNBANESTASJON	60.12	10.83	170
GARDERMOEN	60.21	11.08	202
KONGSVINGER	60.19	12.01	148
FLISA	60.61	12.01	185
RENA - HAUGEDALEN	61.16	11.44	240
RENA FLYPLASS	61.19	11.37	255
EVENSTAD	61.43	11.08	257
HJERKINN	62.22	9.542	1012
TYNSET - HANSMOEN	62.27	10.73	482
HAMAR - STAVSBERG	60.82	11.07	221
KISE (HEDMARK)	60.77	10.81	128
LILLEHAMMER - SÆTHERENGEN	61.09	10.48	240
KVITFJELL	61.46	10.13	1030
VENABU	61.65	10.11	930
SKÅBU	61.53	9.402	928
JUVVASSHØ	61.68	8.373	1894
BRÅTÅ - SLETTOM	61.90	7.895	664
GROTLI	62.02	7.664	872
DOMBÅS - NORDIGÅRD	62.07	9.115	638
FOKSTUGU	62.11	9.286	973
STRØMTANGEN FYR	59.15	10.83	10
RYGGE	59.38	10.78	40
GULLHOLMEN	59.44	10.58	14
OSLO - HOVIN	59.92	10.8	100
ALNA	59.93	10.84	90
OSLO - BLINDERN	59.94	10.72	94

TRYVANNSHØGDA	59.98	10.67	514
ASKER	59.86	10.43	163
HØNEFOSS-HØYBY	60.17	10.25	140
VEST-TORPA	60.94	10.04	542
ÅSBJØRSBRÅTEN	60.92	9.289	639
FAGERNES LUFTHAVN	61.01	9.293	822
FAGERNES	60.99	9.237	365
BEITOSTØLEN	61.25	8.923	965
GULSVIK	60.38	9.605	142
NESBYEN - TODOKK	60.57	9.134	166
HEMSEDAL	60.85	8.593	604
GEILO - OLDEBRØTEN	60.53	8.195	772
DRAMMEN - BERSKOG	59.75	10.12	8
KONNERUD	59.71	10.15	193
KONGSBERG BRANNSTASJON	59.62	9.638	170
VEGGLI	60.04	9.147	275
DAGALI LUFTHAVN	60.42	8.501	798
FILEFJELL - KYRKJESTØLANE	61.18	8.113	956
SOGNEFJELLHYTTA	61.56	7.998	1413
FINSEVATN	60.59	7.53	1210
SANDE - GALLEBERG	59.62	10.21	60
MELSOM	59.23	10.35	26
FÆRDER FYR	59.03	10.52	6
SANDHAUG	60.18	7.481	1250
SVENNER FYR	58.97	10.15	15
SKIEN - GEITERYGGEN	59.18	9.567	136
NOTODDEN FLYPLASS	59.57	9.21	20
MÆSSTRAND	59.84	8.179	977
GVARV - NES	59.38	9.213	93
HØYDALSMO	59.50	8.199	560
VÅGSLI	59.77	7.365	821
JOMFRULAND	58.86	9.575	5
LYNGØR FYR	58.63	9.15	4
TORUNGEN FYR	58.40	8.789	12
NELAUG	58.66	8.631	142
TVEITSUND	59.03	8.519	252
LANDVIK	58.34	8.523	6
KJEVIK	58.2	8.077	12
OKSØY FYR	58.07	8.053	9
BYGLANDSFJORD - NESET	58.69	7.803	207
VALLE	59.20	7.527	308
BLÅSJØ	59.33	6.882	1105

HOVDEN - LUNDANE	59.58	7.39	841
KONSMO - HØYLAND	58.27	7.381	263
LINDESNES FYR	57.98	7.048	13
LISTA FYR	58.11	6.567	14
SIRDAL - SINNES	58.92	6.91	560
EIK - HOVE	58.51	6.505	65
EIGERØYA	58.44	5.872	49
OBRESTAD FYR	58.66	5.555	24
SØRHEIM	58.76	5.651	87
SOLA	58.88	5.637	7
KVITSØY - NORDBØ	59.07	5.412	21
LYSEBOTN	59.06	6.647	5
LIARVATN	59.05	6.121	300
FISTER - SIGMUNDSTAD	59.16	6.037	30
MIDTLÆGER	59.84	6.982	1079
NEDRE VATS	59.48	5.751	64
HAUGESUND LUFTHAVN	59.35	5.198	24
UTSIRA FYR	59.31	4.872	55
RØVÆR	59.44	5.078	25
STORD LUFTHAVN	59.79	5.341	49
SLÅTTERØY FYR	59.91	5.068	25
FET I EIDFJORD	60.41	7.280	735
KVAMSØY	60.36	6.275	49
KVAMSKOGEN - JONSHØGDI	60.39	5.964	455
FLESLAND	60.29	5.226	48
BERGEN - FLORIDA	60.38	5.333	12
EVANGER	60.65	6.111	17
VOSSEVANGEN	60.62	6.426	54
FEDJE	60.78	4.72	19
MIDTSTOVA	60.66	7.276	1162
VANGSNES	61.17	6.645	49
SOGNDAL LUFTHAVN	61.16	7.141	497
FJØRLAND - BREMUSEET	61.42	6.764	3
FØRDE LH - BRINGELAND	61.39	5.76	321
FØRDE - TEFRE	61.46	5.933	64
FLORØ LUFTHAVN	61.58	5.028	9
YTTERØYANE FYR	61.57	4.682	26
SANDANE	61.79	6.184	51
SANDANE LUFTHAVN	61.83	6.104	60
STRYN - KROKEN	61.92	6.559	208
KRÅKENES	62.03	4.986	75
FISKÅBYGD	62.10	5.582	41

ØRSTA-VOLDA LUFTHAVN	62.18	6.081	74
SVINØY FYR	62.33	5.268	38
ÅKERNESET	62.19	6.993	900
TAFJORD	62.23	7.422	11
VIGRA	62.56	6.115	22
REKDAL	62.65	6.755	43
MANNEN	62.46	7.770	1294
MÅRSTEIN	62.45	7.848	67
MOLDE LUFTHAVN	62.74	7.262	3
ONA	62.86	6.538	13
SUNNDALSØRA	62.67	8.559	10
KRISTIANSUND LUFTHAVN	63.11	7.816	62
VEIHOLMEN	63.52	7.947	5
RØROS LUFTHAVN	62.58	11.35	625
OPPDAL - SÆTER	62.60	9.667	604
SULA	63.85	8.467	5
ORKDAL - THAMSHAMN	63.32	9.850	4
SOKNEDAL	62.95	10.18	299
KOTSØY	62.98	10.56	127
SELBU	63.22	11.01	160
TRONDHEIM - VOLL	63.41	10.45	127
VÆRNES	63.46	10.94	12
MERÅKER - VARDETUN	63.41	11.73	169
VERDAL - REPPE	63.78	11.67	81
SNÅSA - KJEVLIA	64.16	12.47	195
STEINKJER - SØNDRE EGGE	64.02	11.45	6
ØRLAND	63.70	9.601	10
HALTEN FYR	64.17	9.406	16
BUHOLMRÅSA FYR	64.40	10.46	18
NAMSOS LUFTHAVN	64.47	11.57	2
NORDLI - HOLAND	64.45	13.72	433
GARTLAND	64.53	12.38	95
NAMSSKOGAN	64.74	12.85	140
RØRVIK LUFTHAVN	64.83	11.14	4
NORDØYAN FYR	64.80	10.55	33
SKLINNA FYR	65.20	11.00	23
BRØNNØYSUND LUFTHAVN	65.46	12.22	9
VEGA - VALLSJØ	65.70	11.86	4
TJØTTA	65.83	12.43	21
SANDNESSJØEN LH - STOKKA	65.96	12.47	17
MOSJØEN LUFTHAVN	65.78	13.22	72
LAKSFORS	65.62	13.29	50

MAJAVATN	65.17	13.37	319
SELJELIA	66.13	13.59	126
VARNTRESK	65.83	14.19	406
SKAMDAL	66.23	13.90	5
MO I RANA LUFTHAVN	66.36	14.30	70
STORFORSHEI	66.40	14.53	110
HJARTÅSEN	66.50	14.95	251
SOLVÆR	66.37	12.61	10
MYKEN	66.76	12.49	17
REIPÅ	66.90	13.65	9
SALTDAL	66.85	15.31	81
BODØ	67.27	14.36	11
HELLIGVÆR	67.40	13.90	24
DRAG - AJLUOKTA	68.05	16.08	19
STRAUMSNES	68.43	17.66	200
NARVIK LUFTHAVN	68.44	17.39	31
EVENES LUFTHAVN	68.49	16.68	26
ROTVÆR	68.37	15.94	8
SKROVA FYR	68.15	14.65	11
SVOLVÆR LUFTHAVN	68.25	14.67	9
LEKNES LUFTHAVN	68.16	13.62	26
VÆRØY HELIPORT	67.65	12.72	4
RØST LUFTHAVN	67.53	12.10	4
SORTLAND	68.70	15.42	3
STOKMARKNES LH - SKAGEN	68.58	15.03	3
BØ I VESTERÆLEN	68.61	14.43	8
ANDØYA	69.31	16.13	10
ANDØYA - TROLLTINDEN	69.24	16.00	436
HARSTAD STADION	68.8	16.54	45
HEKKINGEN FYR	69.60	17.84	14
BARDUFOSS	69.06	18.54	76
DIVIDALEN	68.78	19.70	204
TROMSØ	69.65	18.94	100
TROMSØ - LANGNES	69.68	18.91	8
TORSVÅG FYR	70.25	19.50	21
SKIBOTN	69.39	20.27	5
SØRKJOSEN LUFTHAVN	69.79	20.96	6
NORDSTRAUM - KVÆNANGEN	69.83	21.88	6

Table A.1: Table containing information about the stations used in the Observational study (Chapter 4)

Appendix B

Figures from the Cross Sections

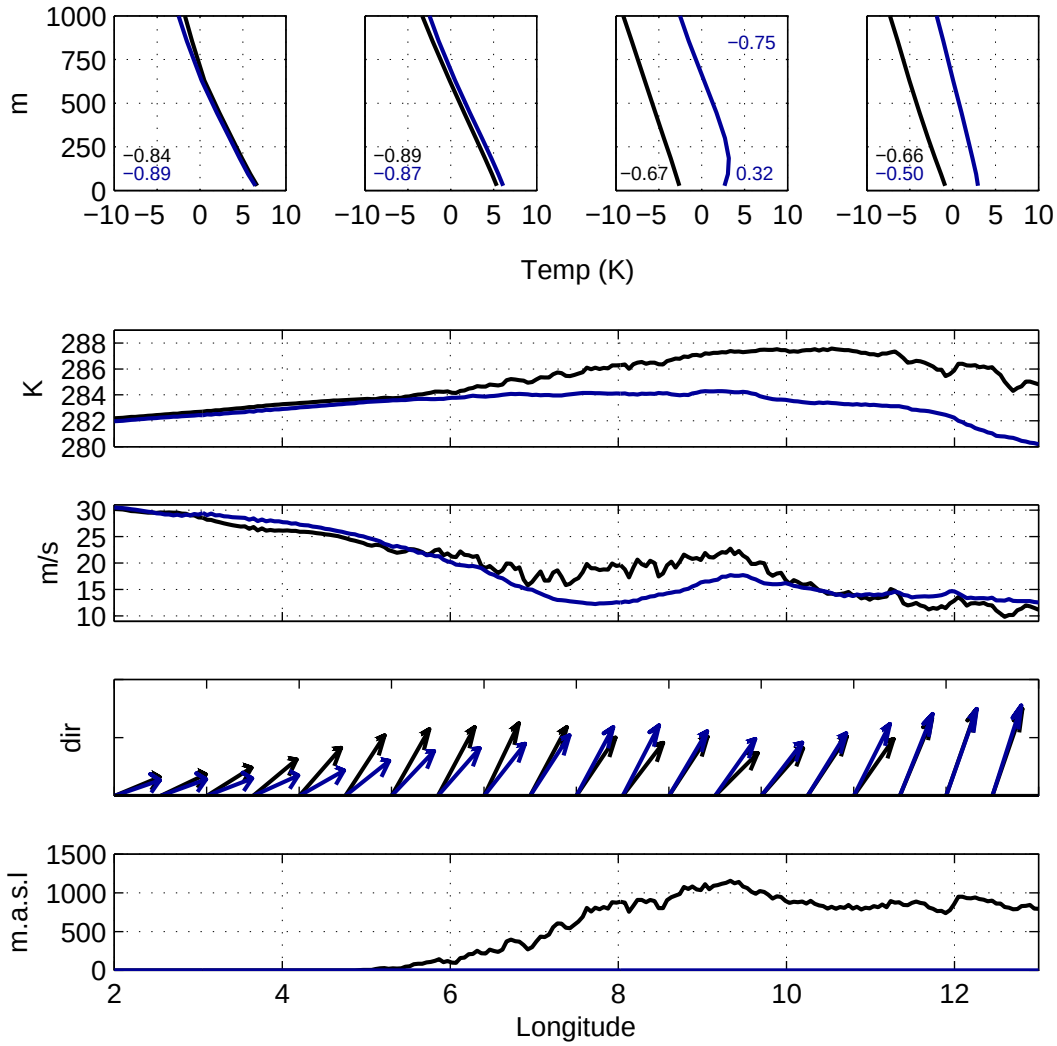

Figure B.1: Cross sections of the data in northern (N) region, for the control run and the flat topography run for 1900UTC on the 25th of December 2011. The black line shows to the results from the control run, while the blue line shows results from the flat run. The mountain height, wind speed, wind direction, and potential temperature (the four lowest panels) were averaged in bins of 0.1° longitude and their respective 1° latitude. The temperature profiles (the four upper panels) were averaged a bit different; the panels were averaged over its respective 1° latitude and the 2° wide bins centered at 3°E, 6°E, 9°E and 12°E, respectively. The lowest panel shows the topography height in meters above sea level (m.a.s.l). The next panel shows the instantaneous 10-m wind direction followed by the corresponding wind speed. Next is the potential temperature (in roughly 450 m above the topography) in degree Kelvin, and the four upper panels show the temperature gradient of the atmosphere, given in number of degree Kelvin per hundred meters.

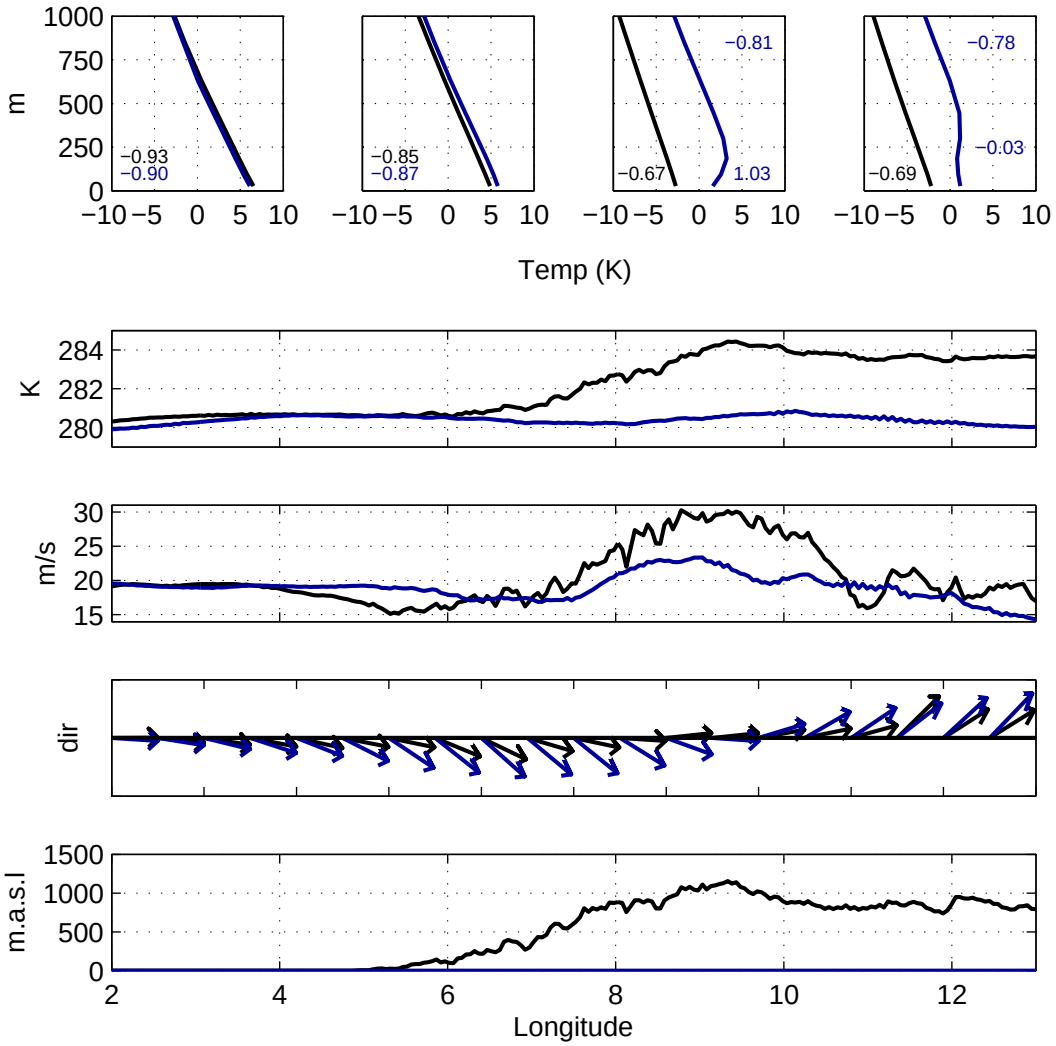

Figure B.2: The same as Figure B.1, but for 2300UTC on the 25th og December 2011.

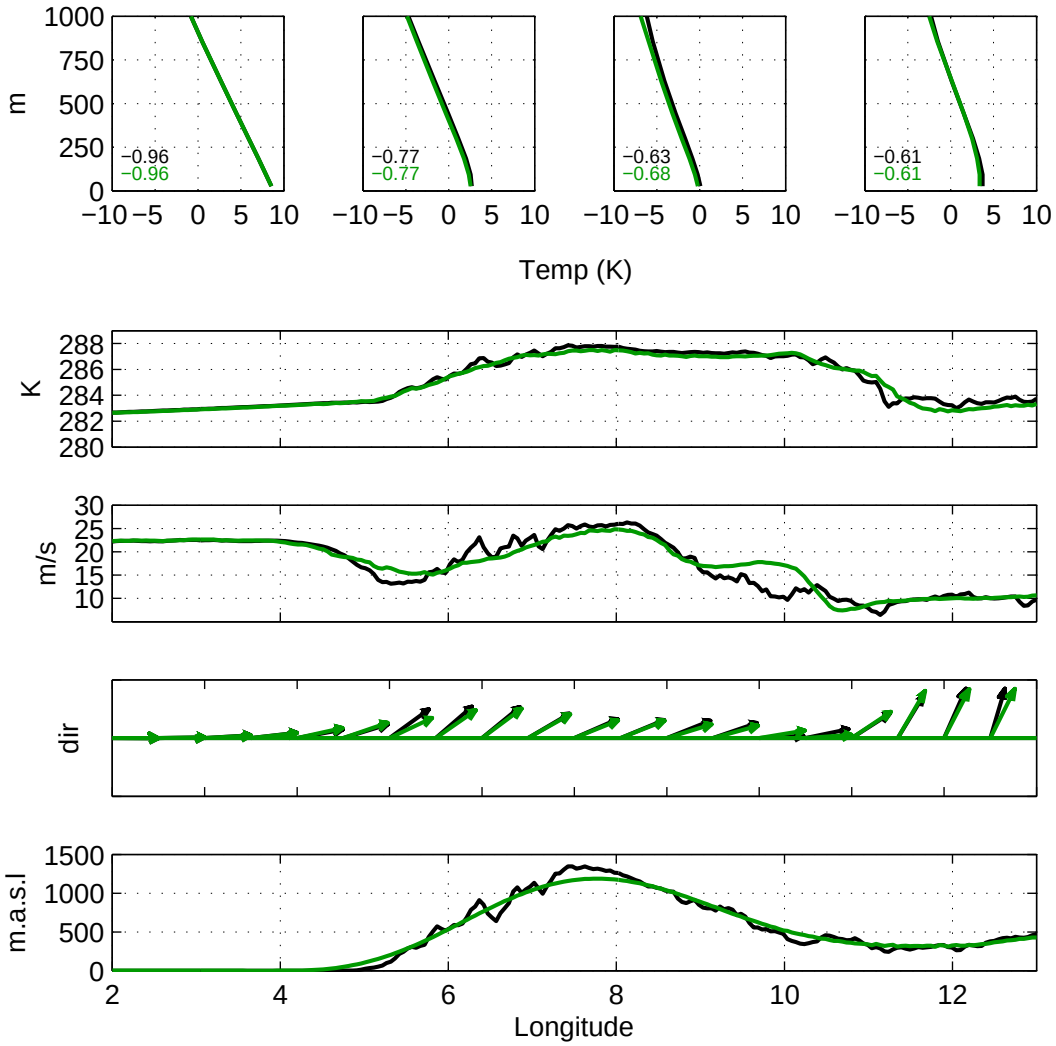

Figure B.3: The same as Figure B.1, but for the southern region, and for the control run (black curves) and the smooth topography run (green curves), at 1900UTC on the 25th of December 2011.

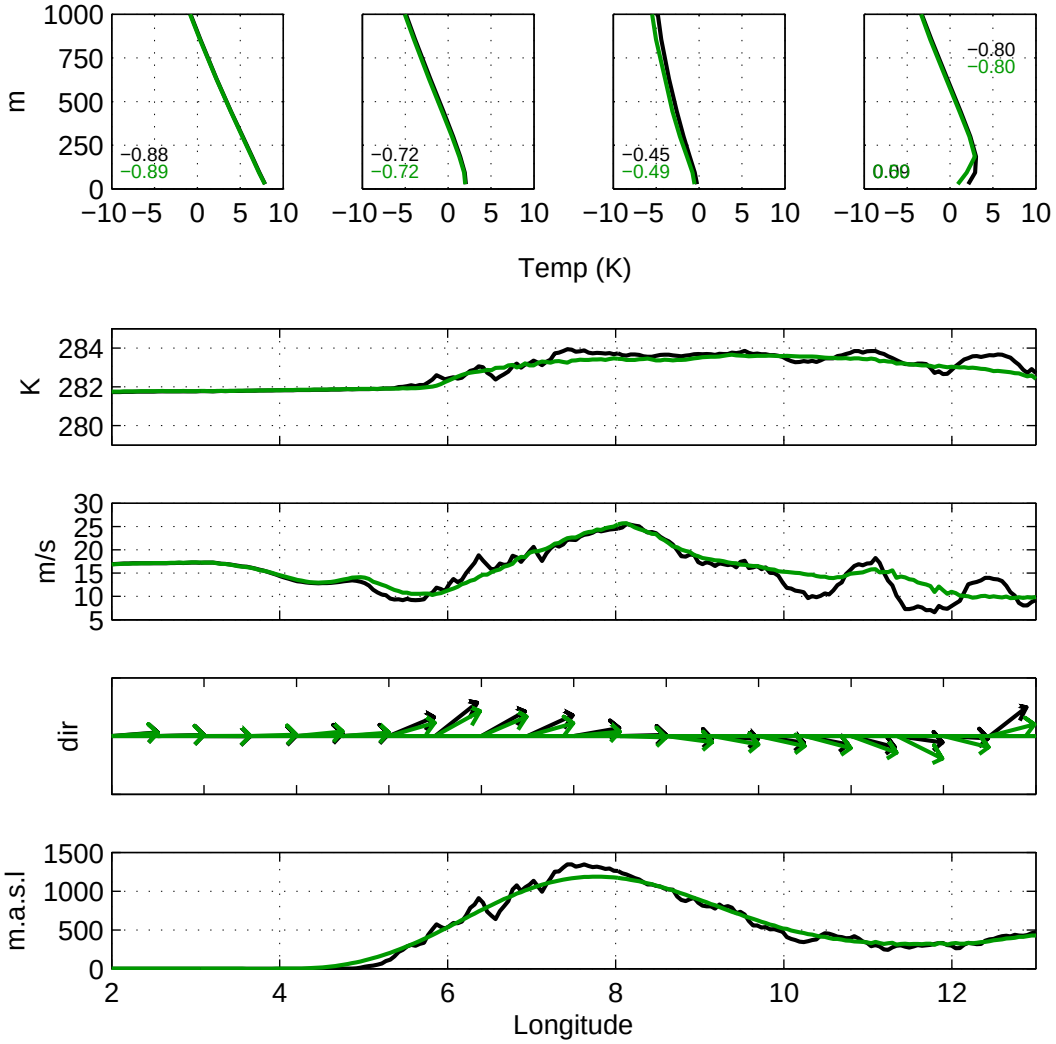

Figure B.4: The same as Figure B.1, but for the southern region, and for the control run (black curves) and the smooth topography run (green curves), at 2300UTC on the 25th of December 2011.

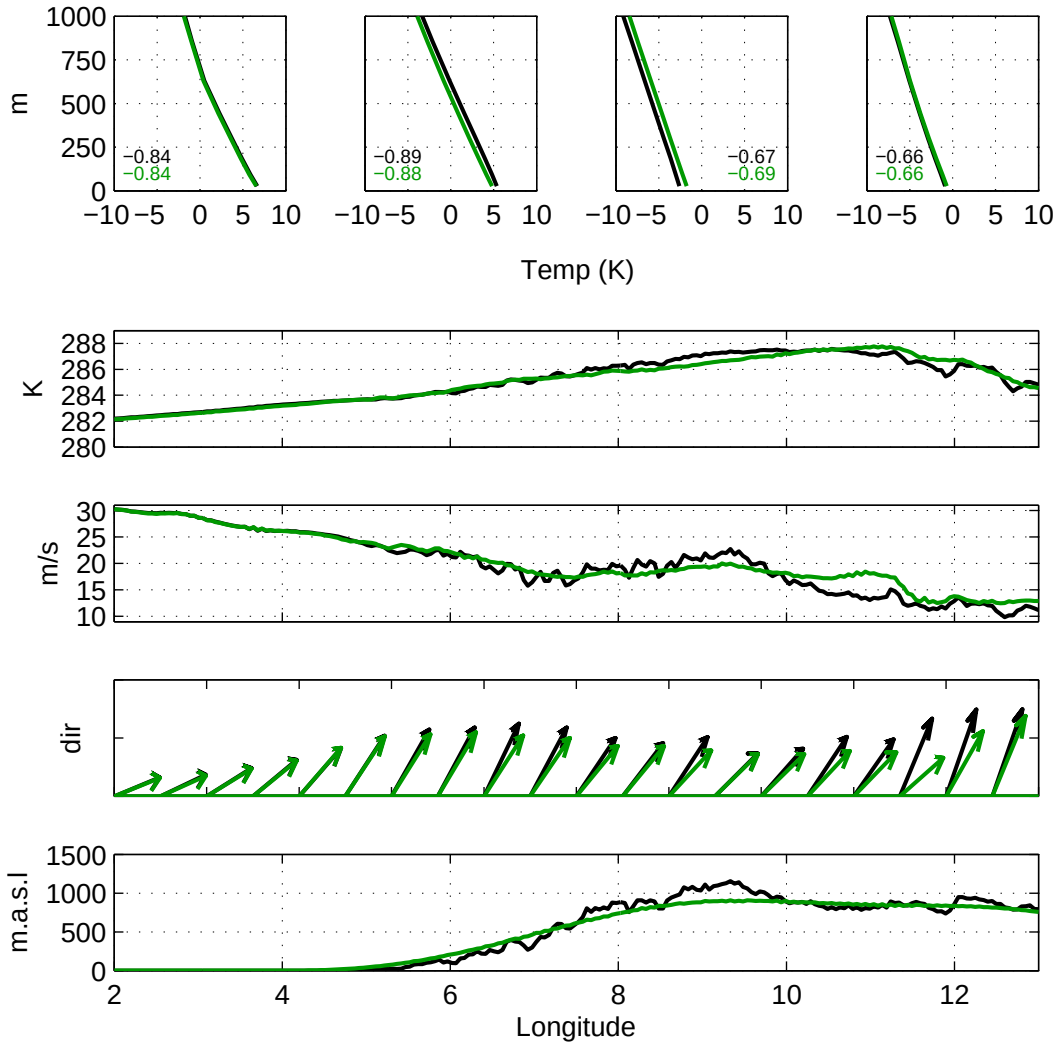

Figure B.5: The same as Figure B.1, but for the control run (black curves) and the smooth topography run (green curves), at 2300UTC on the 25th of December 2011.

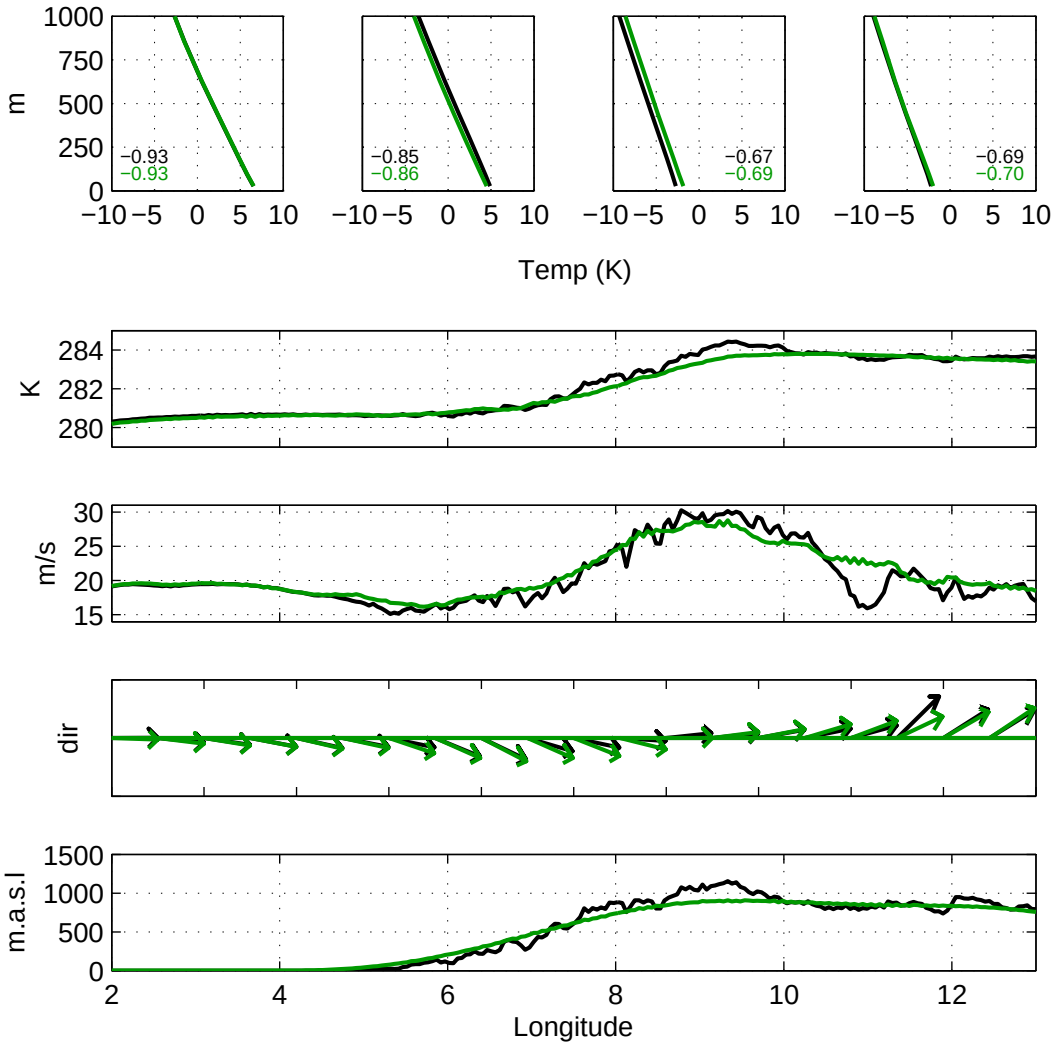

Figure B.6: The same as Figure B.1, but for the control run (black curves) and the smooth topography run (green curves), at 1900UTC on the 25th of December 2011.

Bibliography

Barstad, I. and Grønås, S. (2005), 'Southwesterly flows over southern Norway - mesoscale sensitivity to large-scale wind direction and speed.', *Tellus Series A-dynamic Meteorology and Oceanography* **57**(2), 136–152.

Barstad, I. and Grønås, S. (2006), 'Dynamical structures for southwesterly airflow over southern Norway: the role of dissipation', *Tellus Series A-Dynamic Meteorology and Oceanography* **58**(1), 2–18.

Beljaars, A. (1995), 'The parametrization of surface fluxes in large-scale models under free convection', *Quarterly Journal of the Royal Meteorological Society* **121**(522), 255–270.

Berg, P., Döscher, R. and Koenigk, T. (2013), 'Impacts of using spectral nudging on regional climate model RCA4 simulations of the Arctic.', *Geoscientific Model Development Discussions* **6**(1).

Bjerknes, J. and Solberg, H. (1922), *Life cycle of cyclones and the polar front theory of atmospheric circulation*, Grondahl.

Chen, F. and Dudhia, J. (2001), 'Coupling an advanced land surface-hydrology model with the Penn State-NCAR MM5 modeling system. Part I: Model implementation and sensitivity.', *Monthly Weather Review* **129**(4), 569–585.

Dudhia, J. (1989), 'Numerical study of convection observed during the winter monsoon experiment using a mesoscale two-dimensional model', *Journal of the Atmospheric Sciences* **46**(20), 3077–3107.

Durran, D. R. (1990), 'Mountain waves and downslope winds', *Atmospheric processes over complex terrain. Meteorological Monographs* **23**(45).

Dyer, A. and Hicks, B. (1970), 'Flux-gradient relationships in the constant flux layer', *Quarterly Journal of the Royal Meteorological Society* **96**(410), 715–721.

FinansNorge (2013), 'Finans Norge'. Page retrieved 10.04.2013.
URL: *http://www.fno.no/Hoved/Statistikk/skadeforsikring/Naturskadestatistikk-NASK/*

Gabersek, S. and Durran, D. R. (2004), 'Gap flows through idealized topography. Part I: Forcing by large-scale winds in the nonrotating limit.', *Journal of the Atmospheric Sciences* **61**(23), 2846–2862.

Goody, R., West, R., Chen, L. and Crisp, D. (1989), 'The correlated-k method for radiation calculations in nonhomogeneous atmospheres.', *Journal of Quantitative Spectroscopy and Radiative Transfer* **42**(6), 539–550.

Grønås, S. (1995), 'The seclusion intensification of the New Year's day storm 1992.', *Tellus A* **47**(5), 733–746.

Harstveit, K. (2012), Vinden som blåste - hvor sterk var Dagmar?, Report 41-42, Norges vassdrags- og energidirektorat og Kjeller vindteknikk.

Hartmann, D. L. (1994), *Global Physical Climatology*, Vol. 56, Academic press.

Holton, J. R. and Hakim, G. J. (2012), *An introduction to dynamic meteorology*, Academic Press.

Hov, Ø., Cubasch, U., Fischer, E., Höppe, P., Iversen, T., Gunnar, K., Kundzewicz, Z. W., Rezacova, D., Rios, D., Santos, F. D., Schädler, B., Veisz, O., Zerefos, C., Benestad, R., Murlis, J., M., D., Leckebusch, G. C. and Ulbrich, U. (2013), Extreme weather events in Europe: Preparing for climate change adaptation., Technical report, The Norwegian Academy of Science and Letters. ISBN 978-82-7144-100-5.

Kain, J. S. (1993), 'Convective parameterization for mesoscale models: The Kain-Fritsch scheme.', *The representation of cumulus convection in numerical models, Meteor. Monogr* **46**, 165–170.

Kain, J. S. (2004), 'The Kain-Fritsch convective parameterization: An update.', *Journal of Applied Meteorology* **43**(1), 170–181.

Laprise, R. (1992), 'The Euler equations of motion with hydrostatic-pressure as an independent variable.', *Monthly Weather Review* **120**(1), 197–208.

Laprise, R., Kornic, D., Rapaić, M., Šeparović, L., Leduc, M., Nikiema, O., Luca, A., Diaconescu, E., Alexandru, A. and Lucas-Picher, P. (2012), Considerations of domain size and large-scale driving for nested regional climate models: Impact on internal variability and ability at developing small-scale details., *in* 'Climate Change', Springer, pp. 181–199.

Long, R. R. (1954), 'Some aspects of the flow of stratified fluids: II. Experiments with a two-fluid system', *Tellus* **6**(2), 97–115.

Markowski, P. and Richardson, Y. (2011), *Mesoscale meteorology in midlatitudes*, Vol. 2, Wiley.

Mellor, G. L. and Yamada, T. (1982), 'Development of a turbulence closure model for geophysical fluid problems', *Reviews of Geophysics* **20**(4), 851–875.

MET (2012), 'Observations'. Data retreived 15.12.2012.
URL: *www.eklima.no*

Mlawer, E. J., Taubman, S. J., Brown, P. D., Iacono, M. J. and Clough, S. A. (1997), 'Radiative transfer for inhomogeneous atmospheres: RRTM, a validated correlated-k model for the longwave.', *Journal of Geophysical Research* **102**(D14), 16663–16,682.

Nigro, M. A., Cassano, J. J., Lazzara, M. A. and Keller, L. M. (2012), 'Case study of a barrier wind corner jet off the coast of the Prince Olav mountains, Antarctica', *Monthly Weather Review* **140**(7), 2044–2063.

NSAA (2014), 'After Dagmar.'.
URL: *http://upload.wikimedia.org/wikipedia/commons/e/ec/After_Dagmar.jpg*

Pan, F. F. and Smith, R. B. (1999), 'Gap winds and wakes: SAR observations and numerical simulations', *Journal of the Atmospheric Sciences* **56**(7), 905–923.

Paulson, C. A. (1970), 'The mathematical representation of wind speed and temperature profiles in the unstable atmospheric surface layer', *Journal of Applied Meteorology* **9**(6), 857–861.

Radu, R., Déqué, M. and Somot, S. (2008), 'Spectral nudging in a spectral regional climate model', *Tellus A* **60**(5), 898–910.

Schultz, D. M. and Sienkiewicz, J. M. (2013), 'Using frontogenesis to identify sting jets in extratropical cyclones', *Weather and Forecasting* **28**(3).

Scorer, R. (1949), 'Theory of waves in the lee of mountains', *Quarterly Journal of the Royal Meteorological Society* **75**(323), 41–56.

Skamarock, W., Klemp, J., Dudhia, J., Gill, D., Barker, D., Duda, M., Huang, X., Wang, W. and Powers, J. (2008), 'A description of the advanced research WRF version 3. NCAR Technical Note, NCAR/TN-475+STR'.

Smith, R. (1990), 'Why can't stably stratified air rise over high ground?', *Atmospheric Processes over Complex Terrain, B. Blumen, Ed. American Meteorological Society* pp. 105–107.

Smith, R. B. (1979), 'The influence of mountains on the atmosphere', *Advances in Geophysics.* **21**, 87–230.

Smith, R. B. (1980), 'Linear theory of stratified hydrostatic flow past an isolated mountain', *Tellus* **32**(4), 348–364.

Smith, R. B. (1989), 'Hydrostatic air-flow over mountains', *Advances in Geophysics* **31**, 1–41.

Stull, R. B. (1988), *An introduction to boundary layer meteorology*, Vol. 13, Springer.

Teigland, J. (2002), 'Sosioøkonomiske effekter av ekstremt vær i Norge: en studie av effekter i tid og rom av nyttårsorkanen 1992', *VF-rapport* **7**, 2002.

Thompson, G., Rasmussen, R. M. and Manning, K. (2004), 'Explicit forecasts of winter precipitation using an improved bulk microphysics scheme. Part I: Description and sensitivity analysis.', *Monthly Weather Review* **132**(2).

Wallace, J. M. and Hobbs, P. V. (2006), *Atmospheric science: An introductory survey*, Vol. 92, Academic Press.

Warner, T. T. (2011), *Numerical weather and climate prediction*, Vol. 89, Cambridge University Press Cambridge, UK.

Webb, E. (1970), 'Profile relationships: The log-linear range, and extension to strong stability', *Quarterly Journal of the Royal Meteorological Society* **96**(407), 67–90.

Wetterzentrale (2014), 'Satellite pictures'. Page retreived 05.03.2014.
URL: *http://www.wetterzentrale.de/topkarten/fssatms1.html*

Whiteman, C. D. and Doran, J. C. (1993), 'The relationship between overlying synoptic-scale flows and winds within a valley', *Journal of Applied Meteorology* **32**(11), 1669–1682.